

Accepted: Astronomical Journal

Spectroscopy of Outlying H II Regions in Spiral Galaxies: Abundances and Radial Gradients

Liese van Zee¹

National Radio Astronomy Observatory,² PO Box 0, Socorro, NM 87801
lvanee@nrao.edu

John J. Salzer³

Astronomy Department, Wesleyan University, Middletown, CT 06459-0123
slaz@parcha.astro.wesleyan.edu

Martha P. Haynes

Center for Radiophysics and Space Research and
National Astronomy and Ionosphere Center⁴
Cornell University, Ithaca, NY 14853
haynes@astrosun.tn.cornell.edu

Aileen A. O'Donoghue

Physics Department, St. Lawrence University, Canton, NY 13617
aodo@music.stlawu.edu

Thomas J. Balonek

Department of Physics and Astronomy, Colgate University
13 Oak Drive, Hamilton, NY 13346
tbalonek@colgate.edu

¹Jansky Fellow

²The National Radio Astronomy Observatory is a facility of the National Science Foundation, operated under a cooperative agreement by Associated Universities Inc.

³NSF Presidential Faculty Fellow

⁴The National Astronomy and Ionosphere Center is operated by Cornell University under a cooperative agreement with the National Science Foundation.

ABSTRACT

We present the results of low dispersion optical spectroscopy of 186 H II regions spanning a range of radius in 13 spiral galaxies. Abundances for several elements (oxygen, nitrogen, neon, sulfur, and argon) were determined for 185 of the H II regions. As expected, low metallicities were found for the outlying H II regions of these spiral galaxies. Radial abundance gradients were derived for the 11 primary galaxies; similar to results for other spiral galaxies, the derived abundance gradients are typically -0.04 to -0.07 dex kpc^{-1} .

Subject headings: galaxies: abundances — galaxies: ISM — galaxies: spiral

1. Introduction

Radial abundance gradients, in the sense that the inner H II regions have higher abundances than the outer ones, are found in almost all large spiral galaxies. For instance, a gradient of approximately -0.07 dex kpc^{-1} is observed in both the stellar and gaseous components of the Milky Way (Shaver *et al.* 1983; Smartt & Rolleston 1997). The physical basis for the presence of an abundance gradient is still a matter of debate; successful chemical evolution models typically include a combination of (1) a radial dependence on the star formation activity, generally taking the form of a Schmidt law (e.g., Philipps & Edmunds 1991); (2) radial gas flows (e.g., Edmunds 1990; Götz & Köppen 1992); and (3) a radial dependence on stellar yields due to IMF variations (e.g., Güsten & Mezger 1982). The relative importance of these processes can be constrained by investigating the observed gradients for a large sample of galaxies which span a range of morphological type (e.g., Vila-Costas & Edmunds 1992) or environment (e.g., Skillman *et al.* 1996).

Extensive studies of individual galaxies either via spectroscopy (e.g., NGC 5457, Kennicutt & Garnett 1996; NGC 2403, Garnett *et al.* 1997) or spectrophotometric imaging (e.g., NGC 628, NGC 6946, Belley & Roy 1992; NGC 925, NGC 1073, Martin & Roy 1994; NGC 2366, NGC 4395, Roy *et al.* 1996; NGC 1313, Walsh & Roy 1997) indicate that large numbers of H II region abundances are necessary to determine accurate abundance gradients. While spectrophotometric imaging observations have the advantage that large samples are easily obtained, they are not as accurate as spectroscopic studies for individual objects. Recently, several large spectroscopic surveys and literature compilations have appeared (e.g., McCall *et al.* 1985; Vila-Costas & Edmunds 1992; Zaritsky *et al.* 1994). These studies indicate that the oxygen abundance gradients may be a function of Hubble type (e.g., Vila-Costas & Edmunds 1992). Furthermore, the mass surface density appears to play a critical role in supporting an abundance gradient (e.g., Vila-Costas & Edmunds 1992; Garnett *et al.* 1997).

If the abundance gradients are constant across the full radial extent of the galaxy, the outermost H II regions in spiral galaxies should have low abundances, similar to those found in low luminosity dwarf galaxies. Thus, the outlying H II regions of spiral galaxies provide a new environment in which to investigate metallicity effects on elemental yields (particularly of nitrogen) and other aspects of the star formation process.

In this paper, we present the results of new spectroscopic observations of a large number of outlying H II regions in 11 spiral galaxies. In the few instances where the target galaxies did not have previous abundance measurements reported in the literature, spectra of inner H II regions were obtained as well. The observations presented in this paper complement previous spectroscopic observations by extending the radial coverage. In a previous paper (van Zee *et al.* 1998, hereafter Paper I), these H II region abundances were used to investigate the origin of nitrogen in low metallicity environments. Here, we present the complete data set and discuss the derived radial abundance gradients. This paper is organized as follows. In Section 2, the galaxy sample is defined and the imaging and spectroscopic observations are described. The observed H II region line strengths and diagnostics are presented in Section 3. The abundance derivations are described in Section 4; the radial abundance gradients for all 11 spiral galaxies are discussed in Section 5. The conclusions are summarized in Section 6.

2. Observations

2.1. Sample Selection

To facilitate identification of outlying H II regions and to minimize internal extinction, a sample of 11 nearly face-on spiral galaxies were selected for imaging and spectroscopic observations. In addition, two galaxies from the NGC 2805 group (NGC 2820 and IC 2458) were also observed; NGC 2820 is a nearly edge-on spiral and IC 2458 is a dwarf galaxy. Table 6 lists the physical properties of the sample galaxies. The morphological type, inclination, position angle, and isophotal radius (at the 25 mag arcsec⁻² surface brightness isophote) for each system have been taken from the RC3 (de Vaucouleurs *et al.* 1991). The inclination was derived by assuming an intrinsic axial ratio, q , of 0.2. With the exception of NGC 1068 and NGC 2903, all of the primary targets are classified as late-type (Sc or Sd) spirals. Furthermore, all the galaxies in the sample have low inclination angles and subtend a large angular size.

The distances listed in Table 6 were derived either from Cepheid variables (NGC 2403, Freedman & Madore 1988; NGC 925, Silbermann *et al.* 1996; NGC 5457, Kelson *et al.* 1996), or were estimated from the recessional velocity based on a Virgocentric infall model and an assumed H_0 of 75 km s⁻¹ Mpc⁻¹ (NGC 628, NGC 1068, NGC 2903, NGC 3184: Zaritsky *et al.* 1994; NGC 4395: Wevers *et al.* 1986; NGC 1232, NGC 1637, NGC 2805, NGC 2820, IC 2458: this paper). Absolute magnitudes were computed from the apparent magnitudes listed in the RC3, corrected for internal and Galactic extinction, and the adopted distances. All of the primary targets have

B–band apparent magnitudes brighter than 11.2, corresponding to absolute magnitudes ranging between -17.7 and -21.3 .

Of the 11 primary targets, three (NGC 1232, NGC 1637, and NGC 2805) had no previous abundance measurements reported in the literature. The other 8 were known to have moderate to steep abundance gradients (e.g., Zaritsky *et al.* 1994), but lacked abundance measurements of the outermost H II regions. The total number of new H II region abundances for each galaxy are tabulated in Table 6. Multiple H II regions were observed in all galaxies except for NGC 1068, where the outlying H II regions were discovered to be too faint for the planned abundance measurements.

2.2. Optical Imaging

In preparation for the spectroscopic observations, wide field images of the selected galaxies were obtained with the Burrell Schmidt telescope at KPNO⁵ in 1995 April and October and 1996 January. The S2KA CCD had a read noise of $3 e^-$ and a pixel scale of $2.028'' \text{ pix}^{-1}$. A gain of $2.5 \text{ DN}/e^-$ was selected for the 1995 April observing run; a gain of $3.7 \text{ DN}/e^-$ was selected for all subsequent observing runs. While the typical seeing was less than $2''$, the spatial resolution of these images is dominated by the large pixel size. R–band and H α narrow band images were obtained for all program galaxies. During the 1995 April run, three to four 450 second observations of each program galaxy were obtained with the R–band filter; during the subsequent observing runs, one 600 second exposure was obtained for each galaxy. During all the observing runs, the H α imaging consisted of several sets of ON–OFF–ON observations with individual exposure times of 600 seconds each. A total of three to five H α sets were obtained for each program galaxy (corresponding to total on–line integration times of 3600 to 6000 seconds). The H α filter (KP 1468) had a central wavelength of 6571 \AA and a width of 84 \AA ; the OFF images were obtained through a matched off–line filter (KP 808) centered at 6411 \AA , with a width of 88 \AA .

Data reduction was performed within the IRAF⁶ package and followed standard practice. After bias subtraction and flat fielding, images with multiple exposures were aligned and the sky background was subtracted. The images were then scaled to the level of the “most photometric” (either the frame with the lowest airmass or the one taken under the best weather conditions) and combined with a median filter. At the same time, the off–line H α images were scaled to the level of the on–line images, based on the observed counts for at least six to ten stars in each frame.

Because the majority of these images were taken under non–photometric conditions, they were used primarily as finding charts for the outlying (faint) H II regions. The relevant R–band

⁵Observations made with the Burrell Schmidt of the Warner and Swasey Observatory, Case Western Reserve University.

⁶IRAF is distributed by the National Optical Astronomy Observatories.

and continuum subtracted $H\alpha$ images are presented in Figure 1. The images are oriented with north to the top and east to the left. The $2'$ slits on the $H\alpha$ images indicate the spatial scale of each pair of images.

Optical scale lengths (R_d), tabulated in Table 6, were derived from the R-band images. The IRAF task ELLIPSE was used to fit ellipses of constant surface brightness. We note that several of the galaxies in the present sample are asymmetric, making such fits difficult to interpret. In particular, satisfactory fits were obtained only for NGC 628, NGC 925, NGC 1232, NGC 2403, and NGC 2903. The scale length tabulated in Table 6 for NGC 1068 was derived from a fit to only the outer isophotes, those with $r > 50''$. By far the worst fit was obtained for the severely asymmetric spiral NGC 1637; the scale length presented here should only be taken as a rough estimate. The derived scaled lengths for the remaining galaxies, NGC 2805, NGC 3184, NGC 4395, and NGC 5457, are reasonable, although we caution that the ellipse fitting was not ideal due to their modest asymmetries.

2.3. Optical Spectroscopy

Low resolution optical spectra of the selected H II regions were obtained with the Double Spectrograph on the 5m Palomar⁷ telescope during observing runs in 1996 May and November and 1997 January. The long slit ($2'$) was set at a $2''$ aperture during all observing runs; the seeing was generally better than $2''$. During all observing runs, a 5500 \AA dichroic was used to split the light to the two sides (blue and red), providing complete spectral coverage from $3500\text{--}7600 \text{ \AA}$. The blue spectra were acquired with the 300 lines/mm diffraction grating (blazed at 3990 \AA). The red spectra were acquired with the 316 lines/mm diffraction grating (blazed at 7500 \AA). A thinned 800×800 TI CCD with a read noise of $8 e^-$, a gain of 1.5, and 9.2 \AA effective resolution (2.19 \AA/pix) was used on the blue side; a thinned 1024×1024 TEK CCD with a read noise of 7.5, gain of 2.0, and an effective resolution of 7.8 \AA (2.46 \AA/pix) was used on the red side. The spatial scale of the long slit was 0.8 arcsec/pix on the blue and 0.49 arcsec/pix on the red. The CCD on the blue side had moderate focussing problems across the full wavelength range. During all observing runs, the focus was optimized for $H\delta$ and $[\text{O III}] \lambda 4363$.

The observations were conducted via blind offsets from nearby stars. Stellar and H II region coordinates were derived from the Schmidt narrow band $H\alpha$ images. Astrometric plate solutions were calculated using the coordinates of the bright stars in the HST Guide Star Catalog, yielding positions accurate to within $1''$. The telescope pointing was verified each run by using the same offsetting technique to move between several stars in a field. Offsets between stars and H II regions were typically less than $20'$. Previous observations (e.g., van Zee *et al.* 1997) indicated that the

⁷Observations at the Palomar Observatory were made as part of a continuing cooperative agreement between Cornell University and the California Institute of Technology.

5m telescope could point and track accurately; nonetheless, the newly commissioned offset guider was used to improve the tracking during long exposures.

To reduce light losses due to atmospheric refraction, the slit position angle was set close to the parallactic angle during the observations. The slit positions are illustrated on the H α images in Figure 1 and tabulated in Table 6. The slit numbers listed in Table 6 are ordered in increasing Right Ascension for each galaxy and each slit is labelled by the offset (arcseconds east–west and north–south) from the galaxy center (tabulated in Table 6). The offsets do not necessarily correspond to the location of an H II region since the telescope was often pointed between two (or more) H II regions in order to maximize the number of H II regions observed. The astrometric pointing centers are also given in Table 6 along with the position angle (PA) of the slit. Finally, the observing run and the total integration times are listed. Most observations consisted of two or three 1200 second exposures; in a few instances, primarily due to time constraints, the integration time was only 300 seconds.

Flux calibration was obtained by observations of at least 5 standards per night (Stone 1977; Oke & Gunn 1983; Massey *et al.* 1988), interspersed with the H II region observations. Wavelength calibration was obtained by observations of arc lamps taken before and after each H II region observation. A Hollow Cathode (Fe and Ar) lamp was used to calibrate the blue spectra; a combination of He, Ne, and Ar lamps were used to calibrate the red spectra.

The spectra were reduced and analyzed with the IRAF package. The spectral reduction included bias subtraction, scattered light corrections, and flat fielding with both twilight and dome flats. The 2–dimensional images were rectified based on the arc lamp observations and the trace of stars at different positions along the slit. The sky background was removed from the 2-dimensional images by fitting a low order polynomial along each row of the spectra. One dimensional spectra of each H II region were then extracted from the rectified images. Throughout this paper, the H II region nomenclature is based on east–west and north–south offsets from the galaxy center. These offsets were derived either from the pointing center (if only one H II region was in the slit), or were computed for each H II region from the pointing center, the slit position angle, and the spatial scale of the image. These offsets, therefore, are generally only accurate to 1–2".

The 1D spectra were corrected for atmospheric extinction and flux calibrated. Since the night–to–night variation in the calculated sensitivity function was small, the sensitivity function for each run was created using the standard stars from all nights. As a final step, the individual 20 minute exposures were combined. In general, there was excellent agreement in the continuum level of the final blue and red spectra for each H II region, indicating that the flux calibration and extraction regions were well matched.

A few representative spectra are shown in Figure 2. The three H II regions in Figure 2 are ordered in increasing distance from the center of NGC 1232. Figure 2(a) illustrates a typical spectrum from the inner galaxy; absorption features are present and the low ionization lines, such as [O II] and [N II], are strong while the high ionization lines, such as [O III], are extremely weak

or absent. Figure 2(b) illustrates a typical spectrum from the outer galaxy; the emission lines dominate the spectrum, with both the low and high ionization lines at moderate strength. Finally, Figure 2(c) illustrates the low abundance nature of the outermost H II regions. Here, the [O III] lines are very strong while [N II] and [S II] are weak, indicating that this is a high temperature (low abundance) H II region. Furthermore, [O III] λ 4363 is clearly detected in this spectrum, permitting an accurate temperature estimate (see Section 4.3).

3. Line Ratios and Diagnostic Diagrams

3.1. Extinction

The reddening along the line of sight to each H II region was computed from the observed strengths of the Balmer emission lines. The intrinsic line ratios of $H\alpha/H\beta$ and $H\gamma/H\beta$ were interpolated from the values of Hummer & Storey (1987) for case B recombination, assuming that $N_e = 100 \text{ cm}^{-3}$ and $T_e = 10000 \text{ K}$. For the few H II regions where the [O III] λ 4363 line was detected, the electron temperature as derived from the [O III] lines (see Section 4.3) was used instead of the nominal 10000 K. The reddening function, $f(\lambda)$, normalized at $H\beta$ from the galactic reddening law of Seaton (1979) as parameterized by Howarth (1983), was used, assuming a value of $R = A_V/E_{B-V} = 3.1$. When necessary to bring the two Balmer line ratios into agreement, an underlying Balmer absorption with an equivalent width of 2 \AA was assumed. The reddening coefficients, $c_{H\beta}$, derived for each H II region are listed in Table 6 and are shown as a function of radius in Figure 3. While there is a fair amount of scatter in the reddening plots, the general trend is for the outer H II regions to have lower extinction than the inner ones. Similar extinction gradients have been seen in photometric studies of the dust content in spiral galaxies (e.g., Peletier *et al.* 1995).

3.2. Line Intensities

The reddening corrected line intensities relative to $H\beta$ are given in Table 6. In this and subsequent tables, each H II region is identified by its east–west and north–south offsets from the galaxy center (in arcsec, north and east are positive) and by its slit number (Table 6). Furthermore, the H II regions for each galaxy are ordered by increasing radial distance. The error associated with each relative line intensity was determined by taking into account the Poisson noise in the line, the error associated with the sensitivity function, the contributions of the Poisson noise in the continuum, read noise, sky noise, and flat fielding or flux calibration errors, the error in setting the continuum level (assumed to be 10% of the continuum level), and the error in the reddening coefficient. For a few of the high abundance H II regions, the [O III] lines were so weak that [O III] λ 4959 was not detected. In those instances, the tabulated [O III] line intensities were derived by assuming that the [O III] λ 5007 line intensity was 2.88 times the intensity of [O III]

$\lambda 4959$.

3.3. Diagnostic Diagrams

Since the majority of the H II regions in this sample are from the outer regions of spiral galaxies, they should form well defined H II region sequences in diagnostic diagrams (e.g., Osterbrock 1989). A few galactic nuclei (NGC 925+002–002, NGC 1637–001–000, and NGC 4395–003–003) were also observed, however, so it is worthwhile to examine such plots to determine if these are stellar photoionized emission regions or AGN. Several of the line ratios commonly used as H II region diagnostics are tabulated in Table 6 and are graphically shown in Figures 4 and 5. In these and subsequent Figures, the H II regions in each galaxy are coded by common symbols. The well defined H II region sequence formed by the $[\text{N II}]/\text{H}\alpha$ and $[\text{O III}]/\text{H}\beta$ line ratios is illustrated in Figure 4. A theoretical curve from the H II region model of Baldwin *et al.* (1981) is superposed on the data in Figure 4(a), illustrating that the majority are indeed H II regions. Panel (b) shows the same diagnostic, but with the sum of $[\text{O II}]/\text{H}\beta$ and $[\text{O III}]/\text{H}\beta$ (R_{23}) on one axis instead of $[\text{O III}]/\text{H}\beta$ (after McCall *et al.* 1985). In both of these plots, NGC 4395–003–003 (marked by an arrow) deviates from the overall H II region sequence. This supports the suggestion by Ho *et al.* (1995) that the nucleus of NGC 4395 harbors a dwarf Seyfert. Similarly, while the diagnostic diagrams from $[\text{S II}]/\text{H}\alpha$ are less definitive, the nucleus of NGC 4395 again falls outside of the H II region sequence in Figure 5. Due to the unknown ionization source for NGC4395–003–003, it has been excluded from the following abundance analysis.

4. Abundance Determinations

Several assumptions are required to convert observed line ratios into nebular abundances. In sections 4.1 – 4.3, we describe the methodology used to obtain the electron density and electron temperature for each H II region. In section 4.4, we describe the ionization correction factors which were used to convert the derived ionic abundances to nebular abundances. Finally, in sections 4.5 and 4.6 we discuss the derived oxygen abundances and the relative enrichments of nitrogen, neon, sulfur, and argon.

4.1. Electron Density

The density sensitive line ratio $[\text{S II}] \lambda 6717/6731$ is tabulated for each H II region in Table 6 and graphically illustrated in Figure 6. The maximum value of this line ratio in the low density limit is marked on Figure 6. The majority of the H II regions are within the low density limit ($I(\lambda 6717)/I(\lambda 6731) > 1.35$). In the following abundance analysis, an electron density of 100 cm^{-3} was assumed for the majority of the H II regions; in the few instances where the $[\text{S II}]$ line ratios

were below the low density limit, a version of the FIVEL program of De Robertis *et al.* (1987) was used to calculate the electron density from the observed [S II] line ratios.

4.2. Semi-Empirical Oxygen Abundances

The optical oxygen lines ([O II] $\lambda 3727$ and [O III] $\lambda\lambda 4959, 5007$) are sensitive to both the oxygen abundance and electron temperature. At low metallicities, the dominant coolant is the collisionally excited Lyman series, and thus the total oxygen line intensity ($R_{23} \equiv ([\text{O II}] + [\text{O III}]) / \text{H}\beta$) increases as the abundance increases. As the metallicity increases, however, the infrared fine structure lines, such as the 52μ and 88μ oxygen lines and the C^+ 158μ transition, begin to dominate the cooling. At an oxygen abundance of approximately 1/3 solar, the intensity of the optical oxygen lines reaches a maximum and then declines as the oxygen abundance increases. The behavior of the optical oxygen line intensities as a function of oxygen abundance has been examined via semi-empirical methods (e.g., Searle 1971; Pagel *et al.* 1979; Alloin *et al.* 1979; Edmunds & Pagel 1984; Dopita & Evans 1986; Skillman 1989) and derived from H II region ionization models (e.g., McGaugh 1991; Olofsson 1997). The theoretical models of McGaugh (1991) are shown in Figure 7. The surface is double valued due to the ambiguity between high and low abundances. Furthermore, the geometry of the H II region (represented by the average ionization parameter, \bar{U} , the ratio of ionizing photon density to particle density) introduces a further spread in the estimated abundance for a given R_{23} . In addition, aging of the H II regions can also introduce further scatter as both the ionization parameter and the shape of the ionizing spectrum evolve (e.g., Stasińska & Leitherer 1996; Olofsson 1997); we do not include such effects in the present analysis.

The observed line strengths for the H II regions are plotted in Figure 7. The lowest values of R_{23} occur for the innermost H II regions observed, and therefore presumably populate the high abundance side of the R_{23} surface (see below). At these high oxygen abundances, the ionization parameter (\bar{U}) is approximately 0.001 for all of the H II regions. In contrast, the H II regions with low oxygen abundances span a wide range of \bar{U} , indicating that it is important to include such ionization effects when using the strong line method to estimate oxygen abundances.

The process of determining empirical oxygen abundances from the strong line ratios requires several steps. First, abundances for both the high and low abundance side of the surface were determined. Further information is required, however, to resolve the ambiguity between these two values. The degeneracy can be broken by looking at the line strengths of other species. For instance, the [N II]/[O II] line ratio forms a single parameter sequence from high to low abundance (Figure 8). In general, H II regions with $\log ([\text{N II}]/[\text{O II}]) < -1.0$ are believed to have low oxygen abundances, while those with $\log ([\text{N II}]/[\text{O II}])$ greater than -1.0 are on the high abundance side. For those H II regions where the [N II]/[O II] diagnostic was conclusive (those with $\log ([\text{N II}]/[\text{O II}]) > -0.8$ or $\log ([\text{N II}]/[\text{O II}]) < -1.05$), the abundance from the appropriate side of the surface was assigned.

A large fraction of the H II regions in this sample fall in the ambiguous region of the R_{23} relation (the turnover region) where the $[\text{N II}]/[\text{O II}]$ diagnostic is inconclusive. Thus, it was necessary to identify an alternative means of determining the oxygen abundance for these H II regions. Like the $[\text{N II}]/[\text{O II}]$ diagnostic, the $[\text{N II}]/\text{H}\alpha$ ratio increases with increasing oxygen abundance (Figure 9). The relation between the $[\text{N II}]/\text{H}\alpha$ line ratio and the oxygen abundance was determined by a weighted least squares fit to the low abundance H II regions from van Zee *et al.* (1997) and the high abundance H II regions ($8.8 < 12 + \log(\text{O}/\text{H}) < 9.1$) in the present sample:

$$12 + \log(\text{O}/\text{H}) = 1.02 \log([\text{NII}]/\text{H}\alpha) + 9.36. \quad (1)$$

Note that the $[\text{N II}]/\text{H}\alpha$ line ratio is only valid as a metallicity estimator for $12 + \log(\text{O}/\text{H}) < 9.1$ and in the absence of shock excitation. Furthermore, with typical errors of 0.2 dex or more, it is not a particularly accurate abundance estimator. However, it does provide an additional method to break the ambiguity of the R_{23} abundances.

For those H II regions where the oxygen abundance could not be resolved based on the $[\text{N II}]/[\text{O II}]$ line ratio, the $[\text{N II}]/\text{H}\alpha$ relation was used to calculate an empirical oxygen abundance. This empirical oxygen abundance was then compared with the two (high and low abundance) estimates from the R_{23} relation. Whichever R_{23} abundance was closest to the empirical abundance was then assigned, unless both the R_{23} abundances were significantly different from the empirical abundance. In the instances where neither the upper nor the lower branch R_{23} abundances were within 0.2 dex of the empirical abundance, the empirical abundance was assigned. This primarily occurred when the empirical abundance estimate was between 8.2 and 8.5, corresponding to the turnover region of the R_{23} relation, a region where typical errors are several tenths of a dex.

4.3. Electron Temperature

The preferred method of obtaining an estimate of the electron temperature of the ionized gas is to derive it from the corrected line strengths of the $[\text{O III}]$ lines. For the 16 H II regions where $[\text{O III}] \lambda 4363$ was detected (9% of the sample), the $[\text{O III}]$ ratio $\lambda\lambda 4959, 5007/\lambda 4363$ is tabulated in Table 6. A version of the FIVEL program of De Robertis *et al.* (1987) was used to compute T_e from this reddening-corrected line ratio. Not unexpectedly, the H II regions with detectable $[\text{O III}] \lambda 4363$ correspond to those with high T_e ; the electron temperatures were typically in the range of 9000 to 14000 K, with errors of 300 to 600 K.

In most cases, however, $[\text{O III}] \lambda 4363$ was not detected, or was contaminated by the nearby Hg $\lambda 4358$ night sky line. In these instances, the electron temperature was estimated from ionization models. Because oxygen is one of the dominant coolants, the electron temperature depends strongly on the oxygen abundance. Thus, if the oxygen abundance is known, the electron temperature can be estimated. The anticorrelation between oxygen abundance and electron temperature (Pagel *et al.* 1979; Shaver *et al.* 1983) was used in a self-consistent manner to

estimate T_e . The errors in the derived temperatures are quite large. For the H II regions where the electron temperature was derived from the assumed oxygen abundance, the error in the electron temperature was set to yield the appropriate error (as determined by the calibration process) in the computed oxygen abundance. For the abundances estimated from R_{23} (71% of the sample), this corresponds to 0.1 dex, or ~ 500 K for a T_e of 5000 to 7000 K. For the oxygen abundances estimated from the $[\text{N II}]/\text{H}\alpha$ relation (20% of the sample), errors of 0.2 dex in the oxygen abundance were adopted, corresponding to temperature uncertainties of ~ 2000 K for a T_e of 10000 K. As a check of self-consistency, the same method was used to estimate the electron temperatures for those H II regions where $[\text{O III}] \lambda 4363$ was detected; in general, the two methods yielded similar results, with absolute differences less than the estimated errors for the empirical method. The electron temperatures adopted for the subsequent abundance analysis are tabulated in Table 6.

Numerical models of H II regions have shown that, particularly at low abundances, there are significant differences between the temperatures in the high- and low-ionization zones (Stasińska 1980). This difference must be taken into account to derive accurate abundances. We therefore adopt the approach taken by Pagel *et al.* (1992), who use the H II region models of Stasińska (1990) to derive an approximation for the electron temperature of the O^+ zone:

$$T_e(\text{O}^+) = 2[T_e^{-1}(\text{O}^{++}) + 0.8]^{-1}, \quad (2)$$

where T_e is the electron temperature in units of 10^4 K.

4.4. Ionization Correction Factors

For all atoms other than oxygen, the derivation of atomic abundances requires the use of ionization correction factors (ICFs) to account for the fraction of each atomic species which is in an unobserved ionization state. To estimate the nitrogen abundance, we have assumed that $\text{N}/\text{O} = \text{N}^+/\text{O}^+$ (Peimbert & Costero 1969). To estimate the neon abundance, we have assumed that $\text{Ne}/\text{O} = \text{Ne}^{++}/\text{O}^{++}$ (Peimbert & Costero 1969). To determine the sulfur and argon abundances, we are forced to adopt an ICF from published H II region models to correct for the unobserved S^{+3} and Ar^{+3} states. We have adopted analytical forms of the ICFs as given by Thuan *et al.* (1995). In H II regions where $\text{S}^{++} \lambda 6312$ was not detected, an ICF was assumed based on the average value of the ICF in all other H II regions. The use of an “average” ICF assumes that the ionization characteristics of the H II regions with non-detections of the $\text{S}^{++} \lambda 6312$ line are similar to those where $\lambda 6312$ was detected. This is not necessarily the case, but it appears to work reasonably well. We have assumed an error of 50% in this “average” ICF of 5.8 ± 2.9 .

4.5. Oxygen Abundances

The oxygen abundances tabulated in Table 6 were derived from the observed line strengths (Table 6) and the relevant emissivity coefficients (based on the electron temperature (Table 6) and electron density) as calculated by a version of the FIVEL program of De Robertis *et al.* (1987). The errors in the derived abundances are dominated by the errors inherent in the electron temperature estimates.

As expected, the outermost H II regions in the spiral galaxies have low oxygen abundances. The new observations confirm the low abundance nature of H681 (+010+885) in NGC 5457 (Garnett & Kennicutt 1994), which has the lowest oxygen abundance ($12 + \log (\text{O}/\text{H}) = 7.92 \pm 0.03$) of all the spiral galaxy H II regions in this sample (the H II regions in the dwarf galaxy IC 2458 also have similarly low oxygen abundances). The highest oxygen abundances are found in the asymmetric spiral NGC 1637, with typical abundances of 1.5 to 2 times the solar value.

The majority of the oxygen abundances were ultimately derived from the strong line method (either from the McGaugh (1991) R_{23} calibration or the modified version of this R_{23} relation as described in Section 4.2). Other calibrations of the R_{23} relation yield slightly different results. In particular, the R_{23} calibration of Zaritsky *et al.* (1994) (ZKH) will yield very similar abundances for H II regions with $12 + \log (\text{O}/\text{H}) > 8.5$ (Table 6). Note, however, that since the ZKH analytical form does not explicitly take into account the turnover in the R_{23} relation, it can result in artificially high abundances for the outlying H II regions. A comparison of the derived abundances from the modified McGaugh calibration (this paper) with those derived from the Zaritsky *et al.* (1994) analytical formula is shown in Figure 10. Also shown in Figure 10 and tabulated in Table 6 are the R_{23} abundance estimates from the calibration of Edmunds & Pagel (1984). It is clear from this plot that the EP84 calibration will yield steeper abundance gradients than either the ZKH or the modified McGaugh calibrations used here.

4.6. Nitrogen, Neon, Sulfur, and Argon Abundances

The abundances of nitrogen, neon, sulfur, and argon were computed from the observed line strengths (Table 6), the emissivity coefficients, and the ionization correction factors described in Section 4.4. Their abundances relative to oxygen are tabulated in Table 6. The original purpose of the observations described here was to investigate the N/O ratio in the outlying, low abundance, H II regions of spiral galaxies. Detailed analysis of the derived N/O ratios is presented in a separate paper (van Zee *et al.* 1998, Paper I). Briefly, as seen in other high metallicity H II regions, the N/O ratio increases linearly with the oxygen abundance at high abundance. However, the N/O ratio plateaus for H II regions with metallicities less than 1/3 solar, indicating that there is a primary origin for nitrogen in low metallicity environments.

The relative abundances of the α elements (Ne, S, and Ar) are expected to be constant with

increasing oxygen abundance. Their abundances relative to oxygen are shown in Figure 11. Also shown in Figure 11 are the solar values (Anders & Grevesse 1989). As expected for primary elements, the relative abundance ratios are essentially constant: the mean $\log(\text{Ne}/\text{O})$ is -0.65 ± 0.18 ; the mean $\log(\text{S}/\text{O})$ is -1.55 ± 0.15 ; and the mean $\log(\text{Ar}/\text{O})$ is -2.28 ± 0.11 . These mean ratios are similar to those derived for low metallicity H II regions in dwarf galaxies (e.g., Thuan *et al.* 1995; van Zee *et al.* 1997).

5. Radial Abundance Gradients

The oxygen abundances presented in this paper increase the total number of H II regions observed in these spiral galaxies. Furthermore, a large fraction of the H II regions in this sample are located at radii greater than half of the isophotal radius. These outlying H II regions provide a significant lever–arm for the computation of radial abundance gradients (see also Ferguson *et al.* 1998). The spiral galaxy abundance gradients are illustrated in Figure 12. All deprojected radii have been computed from the H II region offsets and the assumed inclination and position angles (Table 6); the deprojected radii are tabulated (in arcsec) in Table 6. In Figure 12, the deprojected radii have been normalized by the isophotal radius (R_{25}), as listed in the RC3 (de Vaucouleurs *et al.* 1991) and tabulated in Table 6. The filled symbols in Figure 12 represent H II regions from the present study. The open circles represent data from the literature: NGC 628 (McCall *et al.* 1985), NGC 925 (Zaritsky *et al.* 1994), NGC 1068 (Evans & Dopita 1987; Oey & Kennicutt 1993), NGC 2403 (McCall *et al.* 1985; Fierro *et al.* 1986; Garnett *et al.* 1997), NGC 2903 (McCall *et al.* 1985; Zaritsky *et al.* 1994), NGC 3184 (Zaritsky *et al.* 1994), NGC 4395 (McCall *et al.* 1985), and NGC 5457 (Kennicutt & Garnett 1996). To place the literature abundances on a common scale with the abundances derived in this paper, the analytical form of the R_{23} calibration presented by Zaritsky *et al.* (1994) was used to compute the oxygen abundances. As illustrated in Table 6 and Figure 10, this analytical form of the R_{23} calibration yields similar abundance estimates for high abundance H II regions. The only exceptions to this recalibration of the literature data were the few instances where abundances were derived from an electron temperature which was directly measured, either through the [O III] or [O II] line ratios (e.g., NGC 5457, Garnett & Kennicutt 1994; NGC 2403, Garnett *et al.* 1997).

The oxygen abundance gradients obtained from weighted least–squares fits to both the literature and new data points are tabulated in Table 6. For those galaxies with previous abundance gradients reported in the literature, the newly derived abundance gradients are generally in agreement with older results (see, e.g., the compilations by Zaritsky *et al.* 1994; Garnett *et al.* 1997). The few exceptions are NGC 925, NGC 1068, and NGC 4395. For NGC 1068, the one additional H II region in the present study is at such a large radius compared to the previous observations that it determines the gradient. Further observations of the other outlying H II regions in NGC 1068 will be necessary to confirm the derived gradient. For NGC 925 and NGC 4395, the new observations also result in steeper abundance gradients than previously reported

in the literature. The majority of the H II regions in both of these galaxies are at, or near, the R_{23} turnover, so the derived abundances have large errors. The previous spectroscopic studies of NGC 925 (Zaritsky *et al.* 1994) and NGC 4395 (McCall *et al.* 1986) were limited by the small number of H II regions observed; in these studies, the abundance gradients were swamped by the intrinsic errors of the abundance measurements. Spectrophotometric imaging observations of a large number of H II regions in NGC 925 (Martin & Roy 1994) suggested that a steeper abundance gradient existed; the newly derived abundance gradient from the spectroscopic observations is in good agreement with the spectrophotometric imaging results. Spectrophotometric imaging observations of NGC 4395 indicated that the abundance gradient was flat (or nonexistent) in this low luminosity galaxy (Roy *et al.* 1996); the new spectroscopic results suggest that a shallow gradient exists, but the errors in the derived slope are quite large.

A large scatter in the oxygen abundance for a given radius can indicate azimuthal variations of the abundance gradient. An apparent branching of the abundance gradient of NGC 5457 at radii between $R/R_{25} \sim 0.2\text{--}0.5$ was noticed by Kennicutt & Garnett (1996). The two branches are spatially separate, with the higher abundance H II regions lying on the northwest half of the galaxy and the lower abundance H II regions lying on the southeast side (near NGC 5461). As discussed by Kennicutt & Garnett (1996), these abundance variations could arise from the inherent asymmetry of the galaxy, from tidal interactions with its companions NGC 5474 and/or NGC 5477, or from accretion of high-velocity gas. Other galaxies, such as NGC 925 and NGC 2403, also show large variations in the abundance at a given radius. The H II regions in both of these galaxies lie near the turnover region of the R_{23} relation, however. Thus, the large scatter in oxygen abundance is probably due to the intrinsic errors in the abundance measurements. New observations with solid detections of the temperature sensitive lines will be necessary to address the validity of these abundance variations.

Observations of the Milky Way suggest that the abundance gradient may flatten in the outer disk (e.g., Vílchez & Esteban 1996). The outermost points of NGC 5457 suggest that the abundance gradient may flatten in this galaxy as well. However, previous claims of flattening in the inner regions of NGC 5457 (e.g. Zaritsky 1992; Scowen *et al.* 1992; Vila-Costas & Edmunds 1992) have not been substantiated (Henry & Howard 1995; Kennicutt & Garnett 1996). To determine if flattening of the abundance gradient is a common phenomena of the outer disk, observations of H II regions at even larger radii will be necessary. Such observations are challenging due to the faintness of the outermost H II regions, but not impossible (e.g., Ferguson *et al.* 1998).

6. Conclusions

We have presented the results of high signal-to-noise spectroscopy of 186 H II regions spanning a range of radius in 13 spiral galaxies. Abundances for several elements (oxygen, nitrogen, neon, sulfur, and argon) were derived for all except the nucleus of NGC 4395. Below, we summarize the main conclusions.

(1) The H II region diagnostic diagrams indicate that the nucleus of NGC 4395 harbors a dwarf Seyfert. The remaining 185 H II regions form a well defined H II region sequence in the Osterbrock diagnostic diagrams. Furthermore, the majority of the H II regions are low density, with an assumed N_e of 100 cm^{-3} .

(2) A modified version of the R_{23} calibration of McGaugh (1991) was used to derive the majority of the oxygen abundances. In this method, the $[\text{N II}]/\text{H}\alpha$ line ratios are used to break the degeneracy between the upper and lower branches; furthermore, this line ratio is used to estimate the oxygen abundance for H II regions which fall in the R_{23} turnover region ($8.2 < 12 + \log (\text{O}/\text{H}) < 8.5$).

(3) The enrichment of the α elements (neon, sulfur, and argon) relative to oxygen is constant for all H II regions in this sample. The mean α -to-oxygen ratios are consistent with those derived for low metallicity H II regions (e.g., Thuan *et al.* 1995; van Zee *et al.* 1997). The mean abundance ratios are: -0.65 ± 0.18 , -1.55 ± 0.15 , and -2.28 ± 0.11 for $\log (\text{Ne}/\text{O})$, $\log (\text{S}/\text{O})$, and $\log (\text{Ar}/\text{O})$, respectively.

(4) The outlying H II regions presented here extend the radial range of H II region abundances measured in spiral galaxies. For those galaxies with previous abundance measurements, the newly derived radial gradients are generally consistent with those previously reported. For the three galaxies which had no abundance measurements reported in the literature (NGC 1232, NGC 1637, and NGC 2805), each now has abundances measured in at least 15 H II regions.

(5) As expected, the outermost H II regions in the spiral galaxies have abundances similar to those of low luminosity dwarf galaxies. These outlying H II regions provide a new environment in which to investigate metallicity effects on stellar yields and the star formation process (see, e.g., van Zee *et al.* 1998).

We thank Elizabeth Barrett for processing several of the $\text{H}\alpha$ images and Stacy McGaugh for providing us with the ionization models. We thank the anonymous referee for comments which improved the presentation of this paper. We thank Scott Lacey, Stacey Davis, Jennifer Heldmann, Lai Man Lee, Alison Schirmer, and Matt Pickard for their assistance in the observations at the Burrell Schmidt. They and TJB acknowledge travel support from the W.K. Keck Foundation for their support of astronomy through the Keck Northeast Astronomy Consortium. AOD acknowledges travel support by the Judge Francis Bergen Career Development Award in Astrophysics, from the Dudley Observatory, Schenectady, New York. We acknowledge the financial support by NSF grants AST95-53020 to JJS and AST90-23450 and AST95-28860 to MPH. This research has made use of the NASA/IPAC Extragalactic Database (NED) which is operated by the Jet Propulsion Laboratory, California Institute of Technology, under contract with the National Aeronautics and Space Administration.

REFERENCES

- Alloin, D., Collin–Soufrin, S., Joly, M., & Vigroux, L. 1979, *A&A*, 78, 200
- Anders, E., & Grevesse, N. 1989, *Geochim. Cosmochim. Acta*, 53, 197
- Baldwin, J. A., Phillips, M. M., & Terlevich, R. 1981, *PASP*, 93, 5
- Belley, J., & Roy, J.–R. 1992, *ApJS*, 78, 61
- De Robertis, M. M., Dufour, R. J., & Hunt, R. W. 1987, *JRASC*, 81, 195
- de Vaucouleurs, G., de Vaucouleurs, A., Corwin, H. G., Buta, R., Paturel, G., & Fouqué, P. 1991, *Third Reference Catalogue of Bright Galaxies* (Springer, New York) (RC3)
- Dopita, M. A., & Evans, I. N. 1986, *ApJ*, 307, 431
- Edmunds, M. G. 1990, *MNRAS*, 246, 678
- Edmunds, M. G., & Pagel, B. E. J. 1984, *MNRAS*, 211, 507 (EP84)
- Evans, I. N., & Dopita, M. A., 1987, *ApJ*, 319, 662
- Ferguson, A. M. N., Gallagher, J. S., & Wyse, R. F. G. 1998, *AJ*, in press
- Fierro, J., Torres–Peimbert, S., & Peimbert, M. 1986, *PASP*, 98, 1032
- Freedman, W. L., & Madore, B. F. 1988, *ApJ*, 332, L63
- Garnett, D. R., & Kennicutt, R. C. 1994, 426, 123
- Garnett, D. R., Shields, G. A., Skillman, E. D., Sagan, S. P., & Dufour, R. J. 1997, *ApJ*, 489, 63
- Götz, M., & Köppen, J. 1992, *A&A*, 262, 455
- Güsten, R., & Mezger, P. G. 1982, *Vistas, Astro.*, 26, 159
- Henry, R. B. C., & Howard, J. W. 1995, *ApJ*, 438, 170
- Ho, L. C., Filippenko, A. V., & Sargent, W. L. W. 1995, *ApJS*, 98, 477
- Kelson, D. D., Illingworth, G. D., Freedman, W. F., Graham, J. A., Hill, R., Madore, B. F., Saha, A., Stetson, P. B., Kennicutt, R. C., Mould, J. R., Hughes, S. M., Ferrarese, L., Phelps, R., Turner, A., Cook, K. H., Ford, H., Hoessel, J. G., & Huchra, J. 1996, *ApJ*, 463, 26
- Kennicutt, R. C., & Garnett, D. R. 1996, *ApJ*, 456, 504
- Kobulnicky, H. A., & Skillman, E. D. 1996, 471, 211
- Kobulnicky, H. A., & Skillman, E. D. 1997, 489, 636
- Martin, P., & Roy, J.–R. 1994, *ApJ*, 424, 599
- McCall, M. L., Rybski, P. M., & Shields, G. A. 1985, *ApJS*, 57, 1 (MRS)
- McGaugh, S. S. 1991, *ApJ*, 380, 140
- Oey, M. S., & Kennicutt, R. C. 1993, *ApJ*, 411, 137
- Olofsson, K. 1997, *A&A*, 321, 29

- Osterbrock, D. E. 1989, *Astrophysics of Gaseous Nebulae and Active Galactic Nuclei* (University Science Books, Mill Valley)
- Pagel, B. E. J., Edmunds, M. G., Blackwell, D. E., Chun, M. S., & Smith, G. 1979, *MNRAS*, 189, 95
- Pagel, B. E. J., Simonson, E. A., Terlevich, R. J., & Edmunds, M. G. 1992, *MNRAS*, 255, 325
- Peimbert, M., & Costero, R. 1969, *Bol. Obs. Tonantzintla y Tacubaya*, 5, 3
- Peletier, R. F., Valentijn, E. A., Moorwood, A. F. M., Freudling, W., Knapen, J. H., & Beckman, J. E. 1995, *A&A*, 300, L1
- Phillipps, S., & Edmunds, M. G. 1991, *MNRAS*, 251, 84
- Roy, J.–R., Belley, J., Dutil, Y., & Martin, P. 1996, *ApJ*, 460, 284
- Scowen, P. A., Dufour, R. J., & Hester, J. J. 1992, *AJ*, 104, 92
- Searle, L. 1971, *ApJ*, 168, 327
- Shaver, P. A., McGee, R. X., Newton, L. M., Danks, A. C., Pottasch, S. R. 1983, *MNRAS*, 204, 53
- Silbermann, N. A., Harding, P., Madore, B. F., Kennicutt, R. C., Saha, A., Stetson, P. B., Freedman, W. L., Mould, J. R., Graham, J. A., Hill, R. J., Turner, A., Bresolin, R., Ferrarese, L., Ford, H., Hoessel, J. G., Han, M., Huchra, J., Hughes, S. M. G., Illingworth, G. D., Phelps, R., & Sakai, S. 1996, *ApJ*, 470, 1
- Skillman, E. D. 1989, *ApJ*, 347, 883
- Skillman, E. D., & Kennicutt, R. C. 1993, *ApJ*, 411, 655
- Skillman, E. D., Kennicutt, R. C., & Shields, G. A., & Zaritsky, D. 1996, *ApJ*, 462, 147
- Smartt, S. J. & Rolleston, W. R. J. 1997, *ApJ*, 481, L47
- Stasińska, G. 1980, *A&A*, 84, 320
- Stasińska, G. 1990, *A&AS*, 83, 501
- Stasińska, G., & Leitherer, C. 1996, *ApJS*, 107, 661
- Thuan, T. X., Izotov, Y. I., & Lipovetsky, V. A. 1995, *ApJ*, 445, 108
- van Zee, L., Haynes, M. P., & Salzer, J. J. 1997, *AJ*, 114, 2479
- van Zee, L., Salzer, J. J., & Haynes, M. P. 1998, *ApJ*, 497, L1 (Paper I)
- Vila–Costas, M. B., & Edmunds, M. G. 1992, *MNRAS*, 259, 121
- Vílchez, J. M. & Esteban, C. 1996, *MNRAS*, 280, 720
- Walsh, J. R., & Roy, J.–R. 1997, *MNRAS*, 288, 715
- Wevers, B. M. H. R., van der Kruit, P. C., & Allen, R. J. 1986, *A&AS*, 66, 505
- Zaritsky, D. 1992, *ApJ*, 390, L73

Zaritsky, D., Kennicutt, R. C., & Huchra, J. P. 1994, *ApJ*, 420, 87 (ZKH)

This preprint was prepared with the AAS L^AT_EX macros v4.0.

Table 1. Galaxy Properties

Galaxy	RA (2000)	Dec (2000)	Morph. ^a Type	Distance ^b [Mpc]	M_B^c	i^a	p.a. ^a	R_{25}^a [arcsec]	R_d [arcsec]	No. HII Regions
NGC 0628	01:36:41.6	15:47:03	.SAS5..	9.7	−20.1	25	25	314.	71.8	19
NGC 0925	02:27:16.8	33:34:46	.SXS7..	9.29	−19.8	58	102	314.	86.2	44
NGC 1068	02:42:40.6	−00:00:46	RSAT3..	14.4	−21.3	32	70	212.	111.4	1
NGC 1232	03:09:45.3	−20:34:41	.SXT5..	21.5	−21.2	30	90	222.	60.2	16
NGC 1637	04:41:28.0	−02:51:27	.SXT5..	8.6	−18.5	36	15	120.	20.6	15
NGC 2403	07:36:51.0	65:36:04	.SXS6..	3.25	−19.1	60	126	656.	117.3	17
NGC 2805	09:20:20.3	64:06:11	.SXT7..	23.5	−20.7	42	125	189.	74.8	17
IC 2458	09:21:30.0	64:14:20	.I.O.P*	23.5	−16.9	3
NGC 2820	09:21:45.4	64:15:25	.SBS5P/	23.5	−20.1	4
NGC 2903	09:32:10.0	21:30:18	.SXT4..	6.3	−19.9	64	17	378.	85.9	9
NGC 3184	10:18:16.8	41:25:28	.SXT6..	8.7	−19.3	21	135	222.	55.8	17
NGC 4395	12:25:48.9	33:32:52	.SAS9..	4.5	−17.7	18	147	395.	149.9	11
NGC 5457	14:03:12.5	54:20:55	.SXT6..	7.4	−21.2	18	37	865.	152.9	13

^aMorphological type, inclination, position angle, and isophotal radius from de Vaucouleurs *et al.* 1991 (RC3).

^bDistance references: NGC 628, NGC 1068, NGC 2903, NGC 3184– Zaritsky *et al.* 1994; NGC 925– Silbermann *et al.* 1996; NGC 1232, NGC 1637, NGC 2805, IC 2458, NGC 2820– Virgocentric infall model; NGC 2403– Freedman & Madore 1988; NGC 4395– Wevers *et al.* 1986; NGC 5457– Kelson *et al.* 1996.

^cAbsolute magnitude calculated from the apparent magnitude listed in the RC3 and the adopted distance to the system.

TABLE 2. Spectroscopy Observing Log

Slit No.	Name	RA (2000)	Dec (2000)	PA [deg]	Run	T _{int} [sec]
NGC 0628						
1	-232 +112	01 36 25.54	15 48 55.29	8	Jan97	3×1200
2	-086 +186	01 36 35.62	15 50 08.83	38	Jan97	2×1200
3	+063 -157	01 36 45.94	15 44 25.71	47	Jan97	2×1200
4	+178 -052	01 36 53.93	15 46 10.97	182	Jan97	3×1200
5	+256 -041	01 36 59.33	15 46 21.57	90	Nov96	2×1200
6	+292 -020	01 37 01.84	15 46 43.35	59	Jan97	2×1200
NGC 0925						
1	-285 +023	02 26 54.00	33 35 08.88	118	Nov96	2×1200
2	-274 +010	02 26 54.90	33 34 55.68	70	Nov96	2×1200
3	-192 -018	02 27 01.47	33 34 27.86	127	Nov96	1×1200
4	-159 +162	02 27 04.05	33 37 28.27	34	Nov96	2×1200
5	-145 -006	02 27 05.23	33 34 40.15	76	Jan97	2×1200
6	-109 +062	02 27 08.06	33 35 48.25	78	Jan97	2×1200
7	-097 +087	02 27 09.03	33 36 13.09	90	Nov96	2×1200
8	-022 +227	02 27 15.07	33 38 33.38	90	Nov96	2×1200
9	-012 -066	02 27 15.86	33 33 39.67	103	Nov96	2×1200
10	-005 +000	02 27 16.38	33 34 45.91	103	Jan97	2×1200
11	+052 +130	02 27 20.96	33 36 56.17	112	Nov96	2×1200
12	+111 -024	02 27 25.66	33 34 22.52	73	Nov96	2×1200
13	+182 +019	02 27 31.34	33 35 04.95	80	Nov96	2×1200
14	+207 -114	02 27 33.36	33 32 52.10	90	Nov96	2×1200
15	+217 -006	02 27 34.17	33 34 40.22	90	Nov96	2×1200
NGC 1068						
1	+111 -088	02 42 48.02	-00 02 13.59	120	Nov96	3×1200
NGC 1232						
1	-103 -021	03 09 37.98	-20 35 01.88	0	Nov96	2×1200
2	+004 -101	03 09 45.56	-20 36 22.19	0	Nov96	2×1200
3	+021 +091	03 09 46.78	-20 33 10.15	0	Nov96	2×1200
4	+059 +058	03 09 49.51	-20 33 43.30	357	Nov96	2×1200
5	+075 -012	03 09 50.61	-20 34 52.56	0	Nov96	2×1200
6	+099 -101	03 09 52.34	-20 36 21.85	34	Nov96	2×1200
7	+135 +114	03 09 54.88	-20 32 46.88	31	Nov96	2×1200
8	+147 -030	03 09 55.74	-20 35 11.33	0	Nov96	2×1200
NGC 1637						
1	-055 -011	04 41 24.32	-02 51 37.51	0	Nov96	1×1200
2	-017 -031	04 41 26.89	-02 51 58.19	354	Nov96	2×1200
3	-001 +026	04 41 27.96	-02 51 01.17	0	Nov96	2×1200
4	+009 -026	04 41 28.61	-02 51 53.19	16	Nov96	2×1200
5	+026 +055	04 41 29.71	-02 50 32.16	0	Nov96	2×1200
6	+047 -031	04 41 31.13	-02 51 58.19	0	Nov96	2×1200
7	+047 +046	04 41 31.16	-02 50 40.53	353	Nov96	2×1200
8	+058 -054	04 41 31.90	-02 52 20.61	0	Nov96	2×1200
NGC 2403						
1	-425 -002	07 35 42.49	65 36 01.77	344	Jan97	2×1200
2	-377 +104	07 35 50.16	65 37 47.59	7	Jan97	2×1200
3	-104 -256	07 36 34.32	65 31 48.18	358	Jan97	2×1200
4	+178 -203	07 37 19.72	65 32 40.89	17	Jan97	2×1200
5	+358 -192	07 37 48.72	65 32 51.73	33	Jan97	2×1200
6	+376 -106	07 37 51.60	65 34 18.36	8	Jan97	2×1200

TABLE 2. (continued)

Slit No.	Name	RA (2000)	Dec (2000)	PA [deg]	Run	T _{int} [sec]
NGC 2805						
1	-151 +102	09 19 57.19	64 07 53.42	75	Nov96	2×1200
2	-051 -009	09 20 12.57	64 06 01.93	45	Nov96	2×1200
3	-043 -061	09 20 13.76	64 05 10.12	54	Nov96	2×1200
4	-005 -080	09 20 19.53	64 04 51.41	75	Nov96	2×1200
5	+037 -115	09 20 25.94	64 04 15.98	79	Nov96	2×1200
6	+058 -022	09 20 29.21	64 05 49.03	38	Nov96	2×1200
7	+116 -098	09 20 37.99	64 04 33.41	71	Nov96	2×1200
IC 2458						
1	-033 -007	09 21 24.88	64 14 13.03	88	Nov96	1×300
NGC 2820						
1	-000 -000	09 21 45.40	64 15 25.00	63	Nov96	1×300
NGC 2903						
1	-067 -061	09 32 05.17	21 29 17.10	349	Jan97	3×1200
2	+171 +229	09 32 22.26	21 34 07.08	0	Jan97	2×1200
NGC 3184						
1	-119 -121	10 18 06.25	41 23 26.69	313	Jan97	2×1200
2	-058 -007	10 18 11.67	41 25 21.20	275	Jan97	2×1200
3	+005 +135	10 18 17.22	41 27 43.21	275	Jan97	2×1200
4	+079 +035	10 18 23.81	41 26 02.98	351	Jan97	2×1200
5	+092 -093	10 18 24.96	41 23 55.25	295	Jan97	3×1200
NGC 4395						
1	-272 +186	12 25 27.11	33 35 58.77	90	May96	2×1200
2	-226 +237	12 25 30.80	33 36 49.14	90	May96	2×1200
3	-167 -093	12 25 35.56	33 31 19.13	90	May96	2×1200
4	-075 -117	12 25 42.94	33 30 55.50	90	May96	2×1200
5	-023 +379	12 25 47.09	33 39 11.78	90	May96	2×1200
6	-003 -003	12 25 48.62	33 32 49.10	90	May96	1×300
7	+002 -127	12 25 49.08	33 30 45.65	90	May96	2×1200
8	+061 -029	12 25 53.78	33 32 23.66	90	May96	1×1200
9	+088 -119	12 25 55.96	33 30 53.24	90	May96	3×300
10	+118 +206	12 25 58.32	33 36 18.03	90	May96	2×1200
11	+195 -159	12 26 04.49	33 30 13.06	90	May96	2×1200
12	+200 +141	12 26 04.90	33 35 13.92	90	May96	2×1200
NGC 5457						
1	-499 +300	14 02 15.28	54 25 54.88	90	May96	2×1200
2	-459 -053	14 02 19.97	54 20 02.45	90	May96	1×1200
3	-398 -436	14 02 27.13	54 13 39.33	100	May96	2×1200
4	-347 +276	14 02 32.68	54 25 31.78	90	May96	2×1200
5	-291 +489	14 02 39.06	54 29 03.87	96	May96	2×1200
6	-276 -417	14 02 41.05	54 13 58.71	90	May96	2×1200
7	-106 +028	14 03 00.39	54 21 23.79	90	May96	2×600
8	-037 -532	14 03 08.29	54 12 03.57	90	May96	2×1200
9	-002 -001	14 03 12.30	54 20 54.26	90	May96	1×300
9	+005 +887	14 03 13.11	54 35 41.97	113	May96	2×1200
10	+271 -393	14 03 43.34	54 14 22.57	90	May96	2×1200

TABLE 3. HII Region Line Strengths

Offsets		Slit No.	[OII]	[NeIII]	[OIII]	[OI]	[SIII]	H α	[NI]	[SII]	[ArIII]	$c_{H\beta}$	EW
E-W	N-S		3727+3729	3869	4959+5007	6300	6312	6563	6548+6583	6717+6731	7136		(H β)
NGC 0628													
+081	-140	3	2.19±0.08	0.059±0.005	1.486±0.034	0.010±0.001	...	2.86±0.13	0.676±0.024	0.426±0.014	0.066±0.004	0.29±0.05	75
+062	-158	3	2.32±0.16	...	0.353±0.036 ^a	2.86±0.20	0.960±0.057	0.695±0.040	...	0.48±0.07	63
+047	-172	3	2.62±0.12	...	1.035±0.031	0.029±0.005	...	2.65±0.13	0.807±0.033	0.631±0.025	0.055±0.006	0.45±0.05	41
+044	-175	3	2.48±0.10	...	2.070±0.050	0.029±0.003	...	2.87±0.13	0.722±0.027	0.464±0.017	0.089±0.005	0.51±0.05	149
+180	-008	4	2.26±0.09	...	0.709±0.022	0.015±0.004	...	2.86±0.13	0.879±0.034	0.698±0.026	0.054±0.005	0.48±0.05	39
+178	-052	4	1.89±0.07	0.049±0.004	1.141±0.025	0.021±0.001	...	2.86±0.13	0.739±0.027	0.482±0.017	0.058±0.003	0.36±0.05	109
-086	+186	2	2.96±0.11	0.070±0.003	2.068±0.045	0.018±0.001	0.010±0.001	2.81±0.12	0.686±0.024	0.360±0.012	0.078±0.004	0.39±0.05	152
-075	+200	2	4.05±0.21	...	1.476±0.052	2.86±0.16	0.846±0.040	0.611±0.028	0.069±0.008	0.27±0.06	53
+203	-041	5	2.35±0.12	...	1.925±0.064	3.74±0.20	1.001±0.044	0.736±0.030	0.101±0.007	0.40±0.05	182
-073	+203	2	3.12±0.14	...	1.591±0.042	2.86±0.14	0.788±0.032	0.610±0.023	0.071±0.005	0.33±0.05	89
-069	+208	2	2.88±0.11	0.122±0.006	2.715±0.060	0.036±0.002	0.007±0.001	2.72±0.12	0.666±0.023	0.500±0.016	0.084±0.004	0.41±0.05	206
+254	-043	6	3.74±0.15	...	2.221±0.051	2.76±0.13	0.821±0.030	0.875±0.031	0.065±0.004	0.28±0.05	77
+256	-041	5	4.76±0.26	...	2.488±0.085	2.82±0.16	0.795±0.037	0.958±0.041	0.086±0.008	0.05±0.06	59
-232	+112	1	4.23±0.25	...	0.866±0.053	2.86±0.19	0.569±0.037	0.682±0.039	...	0.24±0.07	38
+262	-041	5	4.12±0.26	...	2.254±0.094	2.83±0.19	0.822±0.045	0.946±0.048	0.096±0.010	0.38±0.07	81
+264	-037	6	3.43±0.16	...	2.936±0.080	2.86±0.15	0.581±0.027	0.760±0.032	0.083±0.008	0.16±0.05	49
+265	-041	5	3.39±0.20	...	4.014±0.150	2.83±0.18	0.532±0.029	0.626±0.032	0.082±0.010	0.08±0.06	69
-227	+148	1	3.38±0.16	...	2.936±0.082	2.78±0.15	0.426±0.020	0.425±0.018	0.061±0.006	0.26±0.05	191
+292	-020	6	2.48±0.10	0.395±0.017	5.365±0.120	0.022±0.002	...	2.56±0.12	0.211±0.008	0.205±0.007	0.068±0.004	0.39±0.05	190
NGC 0925													
+002	-002	10	1.69±0.08	...	1.036±0.031	2.86±0.14	0.726±0.030	0.668±0.027	0.062±0.006	0.00±0.05	7
-005	+000	10	2.37±0.09	...	0.698±0.019	0.043±0.004	0.011±0.003	2.87±0.13	0.899±0.034	0.931±0.032	0.041±0.004	0.18±0.05	13
-008	+000	10	2.88±0.11	...	0.915±0.023	2.89±0.13	0.866±0.032	0.873±0.030	0.051±0.003	0.34±0.05	17
+010	-004	10	2.94±0.12	...	0.826±0.024	0.059±0.005	0.013±0.004	2.89±0.14	0.919±0.035	0.945±0.034	0.047±0.005	0.38±0.05	15
+015	-005	10	1.59±0.06	...	0.995±0.025	2.90±0.13	0.768±0.028	0.806±0.028	0.058±0.004	0.04±0.05	17
+030	-008	10	3.20±0.14	...	0.545±0.021	2.90±0.14	0.959±0.037	0.867±0.032	0.046±0.003	0.53±0.05	22
+036	-010	10	3.40±0.14	...	0.889±0.023	2.86±0.13	0.825±0.031	0.822±0.029	0.062±0.004	0.52±0.05	39
+042	-011	10	2.82±0.12	...	1.275±0.035	2.86±0.14	0.758±0.030	0.751±0.029	0.057±0.004	0.28±0.05	44
+087	-031	12	3.44±0.17	0.283±0.017	2.286±0.072	0.036±0.003	...	2.83±0.15	0.553±0.023	0.698±0.027	0.087±0.006	0.62±0.05	91
-012	-066	9	2.54±0.12	0.365±0.017	5.129±0.154	0.034±0.002	0.011±0.001	2.84±0.14	0.289±0.012	0.339±0.013	0.112±0.006	0.33±0.05	329
-047	-058	9	4.57±0.22	0.220±0.012	1.544±0.048	0.081±0.004	...	2.75±0.14	0.577±0.023	0.896±0.035	0.062±0.004	0.24±0.05	78
+135	-016	12	4.12±0.20	0.416±0.021	2.716±0.083	0.079±0.004	...	2.80±0.14	0.430±0.017	0.779±0.030	0.074±0.005	0.19±0.05	53
-109	+062	6	2.51±0.10	0.242±0.011	2.834±0.063	0.025±0.002	0.010±0.001	2.86±0.13	0.397±0.015	0.459±0.017	0.083±0.005	0.24±0.05	42
+137	+011	13	3.04±0.20	...	3.489±0.142	2.83±0.19	0.324±0.022	0.727±0.039	0.051±0.010	0.31±0.07	67

TABLE 3. (continued)

Offsets		Slit No.	[OII]	[NeIII]	[OIII]	[OI]	[SIII]	H α	[NII]	[SII]	[ArIII]	$c_{H\beta}$	EW (H β)
E-W	N-S		3727+3729	3869	4959+5007	6300	6312	6563	6548+6583	6717+6731	7136		
-137	+056	6	3.47±0.16	...	2.409±0.070	2.92±0.15	0.501±0.023	0.434±0.019	0.071±0.007	0.26±0.06	242
-145	-006	5	2.72±0.10	0.270±0.011	4.091±0.090	0.032±0.002	0.013±0.001	2.65±0.12	0.318±0.012	0.378±0.013	0.088±0.005	0.51±0.05	160
-080	+087	7	4.86±0.24	...	1.947±0.059	0.045±0.002	0.011±0.001	2.80±0.14	0.491±0.020	0.667±0.025	0.067±0.004	0.29±0.05	110
-114	+087	7	4.86±0.25	...	2.656±0.083	0.117±0.007	...	2.86±0.15	0.451±0.020	0.917±0.037	0.068±0.005	0.29±0.06	23
+161	+015	13	3.74±0.19	...	2.256±0.071	2.83±0.15	0.328±0.014	0.573±0.023	0.052±0.004	0.22±0.05	81
+174	+018	13	4.67±0.29	...	1.087±0.055	2.83±0.18	0.319±0.024	0.657±0.036	...	0.17±0.06	19
+182	+019	13	2.46±0.12	0.219±0.012	4.575±0.139	2.83±0.14	0.168±0.007	0.272±0.011	0.073±0.005	0.19±0.05	163
-187	-017	5	3.32±0.13	0.195±0.008	3.423±0.076	0.068±0.003	...	2.86±0.13	0.366±0.013	0.601±0.020	0.069±0.004	0.23±0.05	75
-192	-018	3	3.54±0.18	0.233±0.013	3.875±0.120	0.083±0.004	0.013±0.001	2.80±0.14	0.344±0.015	0.742±0.029	0.069±0.004	0.35±0.05	112
-192	-018	5	3.55±0.14	0.227±0.009	3.760±0.083	0.056±0.003	...	2.68±0.12	0.303±0.011	0.502±0.017	0.070±0.004	0.32±0.05	203
-198	-013	3	3.29±0.16	0.282±0.015	4.573±0.140	0.096±0.005	0.011±0.001	2.79±0.14	0.296±0.013	0.603±0.024	0.076±0.005	0.43±0.05	152
+209	-006	15	4.62±0.27	...	1.721±0.067	2.83±0.17	0.361±0.020	0.533±0.026	0.066±0.008	0.26±0.06	102
-200	-020	5	3.11±0.12	0.292±0.012	3.467±0.077	0.057±0.003	...	2.86±0.13	0.411±0.014	0.586±0.020	0.077±0.004	0.20±0.05	243
+217	-006	15	3.08±0.16	0.570±0.031	4.906±0.155	2.83±0.15	0.234±0.012	0.521±0.022	0.051±0.005	0.20±0.05	48
+156	-114	14	4.37±0.22	...	2.219±0.068	0.089±0.005	0.014±0.002	2.82±0.15	0.431±0.018	0.730±0.028	0.064±0.004	0.35±0.05	108
-220	+004	3	3.97±0.19	0.095±0.005	1.994±0.061	0.045±0.002	0.010±0.001	2.85±0.14	0.392±0.016	0.577±0.022	0.061±0.004	0.44±0.05	124
+221	-006	15	2.41±0.14	...	6.583±0.222	0.086±0.007	...	2.83±0.16	0.257±0.014	0.543±0.025	0.067±0.007	0.08±0.06	117
+052	+130	11	3.39±0.17	0.325±0.020	4.487±0.142	2.83±0.15	0.215±0.010	0.358±0.015	0.089±0.006	0.43±0.05	107
-250	+019	2	2.19±0.11	0.193±0.010	3.913±0.118	0.039±0.002	0.012±0.001	2.82±0.14	0.266±0.011	0.403±0.016	0.081±0.005	0.44±0.05	176
+206	-114	14	3.38±0.18	...	2.976±0.099	2.83±0.16	0.359±0.017	0.653±0.029	0.073±0.007	0.16±0.05	119
+019	+143	11	2.93±0.15	0.586±0.030	5.950±0.184	0.060±0.004	0.012±0.003	2.77±0.14	0.218±0.010	0.388±0.015	0.079±0.005	0.31±0.05	166
-174	+140	4	3.67±0.19	0.285±0.019	3.678±0.118	0.050±0.005	0.013±0.004	2.83±0.15	0.284±0.013	0.598±0.024	0.068±0.006	0.22±0.05	41
-262	+011	1	4.75±0.32	...	2.650±0.118	3.14±0.22	0.324±0.033	0.666±0.041	...	0.44±0.07	48
-272	+016	1	4.60±0.26	...	2.320±0.081	2.86±0.17	0.316±0.019	0.821±0.038	0.043±0.008	0.43±0.06	66
-274	+010	2	3.75±0.18	0.574±0.028	3.854±0.118	0.100±0.005	...	2.84±0.15	0.319±0.013	0.757±0.029	0.061±0.004	0.00±0.05	56
-285	+023	1	4.73±0.24	0.216±0.017	2.145±0.070	0.043±0.006	0.032±0.006	2.86±0.16	0.308±0.016	0.633±0.027	0.048±0.006	0.35±0.05	61
-159	+162	4	4.96±0.30	...	1.334±0.062	3.06±0.20	0.429±0.028	1.138±0.058	...	0.22±0.07	35
-308	+035	1	4.98±0.25	...	1.499±0.049	0.136±0.008	...	3.26±0.17	0.502±0.022	1.024±0.041	0.092±0.007	0.10±0.05	546
-149	+177	4	3.94±0.20	0.125±0.010	1.872±0.060	0.045±0.004	0.008±0.003	2.86±0.15	0.323±0.015	0.611±0.024	0.044±0.004	0.22±0.05	70
-022	+227	8	2.04±0.10	0.238±0.015	5.653±0.177	2.79±0.15	0.148±0.008	0.258±0.011	0.076±0.005	0.14±0.05	146
NGC 1068													
+111	-088	1	1.58±0.11	...	0.632±0.049 ^a	2.86±0.19	1.443±0.079	0.711±0.038	...	0.49±0.06	13
NGC 1232													
+062	+004	4	1.47±0.07	...	0.204±0.011	0.032±0.003	...	2.90±0.15	1.172±0.048	0.692±0.027	...	0.37±0.05	30
+075	-001	5	2.74±0.16	...	0.303±0.032 ^a	2.86±0.18	1.315±0.069	0.826±0.043	...	0.20±0.06	25

TABLE 3. (continued)

Offsets		Slit No.	[OII]	[NeIII]	[OIII]	[OI]	[SIII]	H α	[NII]	[SII]	[ArIII]	$c_{H\beta}$	EW (H β)
E-W	N-S		3727+3729	3869	4959+5007	6300	6312	6563	6548+6583	6717+6731	7136		
+075	-012	5	2.90±0.16	...	0.412±0.024 ^a	0.076±0.007	...	2.86±0.16	1.431±0.065	0.858±0.036	...	0.52±0.06	53
+059	+058	4	1.49±0.07	...	0.300±0.010	0.019±0.001	0.002±0.001	2.88±0.15	1.349±0.054	0.663±0.025	0.019±0.001	0.23±0.05	63
-103	-021	1	2.28±0.11	...	0.652±0.021	0.046±0.003	...	2.84±0.14	1.166±0.047	0.724±0.028	0.033±0.003	0.26±0.05	40
-103	+022	1	3.12±0.16	...	1.066±0.037	0.068±0.008	...	2.86±0.16	1.066±0.047	0.676±0.029	0.035±0.007	0.27±0.05	86
+021	+091	3	2.53±0.12	...	1.349±0.041	0.032±0.002	0.007±0.001	2.86±0.14	1.018±0.041	0.580±0.021	0.057±0.003	0.49±0.05	113
+004	-101	2	3.18±0.15	...	0.979±0.030	0.045±0.002	0.007±0.001	2.88±0.15	1.203±0.048	0.728±0.027	0.048±0.003	0.40±0.05	191
+057	+098	4	4.18±0.22	...	1.590±0.055	0.131±0.009	0.018±0.005	2.94±0.16	1.030±0.042	1.028±0.042	0.062±0.006	0.39±0.05	86
+056	+106	4	3.26±0.25	...	1.987±0.110	2.72±0.22	0.685±0.054	0.687±0.053	...	0.00±0.08	8
+147	-030	8	2.91±0.15	...	1.114±0.036	0.067±0.004	...	2.79±0.15	1.073±0.045	0.758±0.030	0.039±0.003	0.34±0.05	47
+117	+084	7	2.84±0.14	...	2.086±0.064	0.044±0.003	...	2.87±0.15	0.652±0.027	0.605±0.024	0.044±0.003	0.10±0.05	86
+099	-101	6	3.51±0.18	...	1.875±0.060	2.86±0.15	0.821±0.035	0.520±0.021	0.060±0.004	0.29±0.05	97
+093	-110	6	3.93±0.20	...	2.115±0.068	0.068±0.006	...	2.86±0.16	0.822±0.035	0.734±0.031	0.055±0.006	0.11±0.05	46
+147	-065	8	3.40±0.19	...	1.639±0.065	2.88±0.17	0.737±0.037	0.717±0.035	0.041±0.008	0.19±0.06	26
+135	+114	7	1.89±0.09	0.199±0.010	5.247±0.159	0.022±0.001	0.009±0.001	2.77±0.14	0.314±0.013	0.250±0.010	0.069±0.004	0.02±0.05	227
NGC 1637													
-001	-000	3	1.00±0.05	...	0.244±0.014 ^a	0.067±0.004	...	2.92±0.15	2.360±0.097	0.873±0.034	...	0.97±0.05	9
+016	-001	4	2.88±0.40	...	0.198±0.110 ^a	2.86±0.38	1.648±0.174	0.814±0.083	...	1.28±0.13	3
-019	-009	2	2.20±0.35	...	0.877±0.156 ^a	2.86±0.42	1.730±0.208	0.658±0.078	...	1.03±0.14	12
-020	-000	2	0.40±0.04	...	0.081±0.033 ^a	2.86±0.18	1.248±0.065	0.572±0.029	...	0.71±0.06	9
-001	+026	3	1.25±0.07	...	0.395±0.018	2.86±0.16	1.403±0.061	0.709±0.029	...	0.34±0.06	22
+009	-026	4	1.44±0.08	...	0.197±0.023 ^a	0.036±0.005	...	2.86±0.17	1.359±0.062	0.731±0.032	...	0.74±0.06	40
+022	+018	4	1.35±0.07	...	0.105±0.017 ^a	2.86±0.16	1.252±0.055	0.590±0.025	...	0.55±0.05	19
+026	+018	5	1.43±0.11	...	0.207±0.047 ^a	2.86±0.20	1.307±0.077	0.716±0.042	...	0.45±0.07	13
-017	-031	2	0.67±0.05	0.336±0.031	0.104±0.024 ^a	2.86±0.17	1.216±0.059	0.562±0.026	...	0.61±0.06	12
+051	+012	7	0.55±0.04	...	0.133±0.030 ^a	2.71±0.16	1.307±0.064	0.729±0.035	...	0.09±0.06	39
+053	-007	7	0.16±0.03	...	0.056±0.033 ^a	2.84±0.18	1.187±0.060	0.348±0.018	...	0.26±0.06	53
-055	-011	1	2.17±0.18	...	0.504±0.064 ^a	2.86±0.23	1.488±0.097	0.740±0.048	...	0.40±0.08	20
+047	-031	6	1.17±0.06	...	0.137±0.006	2.75±0.14	1.304±0.054	0.534±0.021	0.020±0.002	0.34±0.05	76
+047	+046	7	1.48±0.09	...	0.144±0.024 ^a	2.86±0.17	1.561±0.075	0.626±0.028	...	0.76±0.06	13
-055	-032	1	1.46±0.12	...	0.438±0.058 ^a	2.83±0.22	1.599±0.103	0.910±0.059	...	0.42±0.08	41
+058	-054	8	3.88±0.20	...	0.821±0.028	0.046±0.004	...	2.86±0.15	1.091±0.046	0.788±0.032	0.073±0.006	0.20±0.05	364
NGC 2403													
+186	-177	4	3.54±0.15	0.386±0.020	4.651±0.111	2.86±0.14	0.702±0.027	1.123±0.040	0.097±0.006	0.25±0.05	84
+178	-203	4	2.07±0.08	0.126±0.005	2.919±0.064	2.79±0.12	0.321±0.011	0.246±0.009	0.078±0.004	0.24±0.05	92
+176	-211	4	4.18±0.23	...	0.634±0.044 ^a	3.95±0.24	0.819±0.042	1.134±0.053	0.034±0.009	0.39±0.06	35

TABLE 3. (continued)

Offsets		Slit No.	[OII]	[NeIII]	[OIII]	[OI]	[SIII]	H α	[NII]	[SII]	[ArIII]	$c_{H\beta}$	EW (H β)
E-W	N-S		3727+3729	3869	4959+5007	6300	6312	6563	6548+6583	6717+6731	7136		
+166	-229	4	3.94±0.17	...	2.067±0.053	2.87±0.14	0.513±0.021	0.793±0.029	0.051±0.004	0.39±0.05	122
+356	-195	5	3.87±0.15	0.199±0.010	4.055±0.092	2.86±0.13	0.416±0.015	0.682±0.024	0.085±0.005	0.14±0.05	73
+360	-190	5	3.80±0.16	...	1.276±0.033	0.146±0.007	...	2.86±0.13	0.458±0.017	0.897±0.032	0.041±0.003	0.18±0.05	50
+377	-163	5	3.23±0.13	0.076±0.006	2.900±0.066	2.71±0.12	0.335±0.012	0.408±0.014	0.076±0.004	0.14±0.05	198
+376	-106	6	2.81±0.11	0.263±0.010	4.156±0.091	0.014±0.001	0.011±0.001	2.27±0.10	0.183±0.006	0.206±0.007	0.065±0.003	0.35±0.05	132
-377	+104	2	3.37±0.13	0.146±0.008	2.294±0.052	2.86±0.13	0.376±0.014	0.413±0.014	0.071±0.004	0.16±0.05	92
-105	-218	3	2.43±0.13	...	1.380±0.052	2.47±0.14	0.246±0.017	0.286±0.017	...	0.10±0.06	98
-105	-224	3	3.48±0.16	...	1.011±0.032	2.59±0.13	0.335±0.015	0.415±0.018	...	0.20±0.05	53
-381	+082	2	3.69±0.16	...	2.836±0.072	2.76±0.13	0.336±0.014	0.426±0.016	0.076±0.006	0.17±0.05	208
+383	-056	6	3.33±0.14	...	3.106±0.074	2.30±0.11	0.222±0.009	0.219±0.009	0.055±0.004	0.22±0.05	233
-104	-256	3	4.10±0.18	...	1.447±0.039	2.86±0.14	0.291±0.013	0.350±0.014	0.037±0.004	0.31±0.05	80
-425	-002	1	3.60±0.15	...	2.328±0.055	2.54±0.12	0.254±0.011	0.428±0.016	0.051±0.004	0.10±0.05	52
-423	-010	1	3.14±0.14	...	2.570±0.065	2.44±0.12	0.209±0.010	0.311±0.012	0.040±0.004	0.10±0.05	65
-421	-017	1	4.33±0.18	...	0.612±0.017	2.58±0.12	0.308±0.013	0.443±0.017	0.026±0.003	0.10±0.05	77
NGC 2805													
-051	-009	2	2.09±0.10	0.081±0.004	1.693±0.051	0.027±0.001	0.007±0.001	2.86±0.14	0.614±0.024	0.527±0.020	0.046±0.003	0.18±0.05	59
+055	-026	6	3.90±0.20	0.180±0.017	2.226±0.073	0.041±0.004	...	2.88±0.16	0.637±0.028	0.634±0.027	0.059±0.005	0.44±0.05	57
+058	-022	6	3.63±0.18	0.116±0.009	1.547±0.048	0.060±0.003	...	2.81±0.14	0.713±0.030	0.752±0.029	0.058±0.004	0.34±0.05	116
-021	-045	3	2.93±0.15	...	1.552±0.051	2.88±0.16	0.755±0.034	0.574±0.024	0.066±0.005	0.37±0.05	87
+032	-056	6	4.23±0.24	...	1.995±0.073	2.79±0.16	0.617±0.029	0.682±0.031	0.039±0.006	0.46±0.06	42
-001	-079	4	2.68±0.13	0.145±0.008	2.777±0.083	0.033±0.002	0.011±0.001	2.82±0.14	0.467±0.019	0.483±0.019	0.068±0.004	0.16±0.05	73
-005	-080	4	4.01±0.20	...	2.156±0.065	0.051±0.003	0.009±0.001	2.82±0.14	0.617±0.025	0.752±0.029	0.051±0.003	0.22±0.05	28
-041	-090	4	4.35±0.21	0.260±0.013	2.512±0.076	0.077±0.004	...	2.87±0.15	0.535±0.021	0.816±0.031	0.054±0.003	0.09±0.05	47
+037	-115	5	2.52±0.12	0.300±0.015	4.662±0.140	0.044±0.002	0.013±0.001	2.87±0.15	0.275±0.011	0.463±0.018	0.065±0.004	0.28±0.05	83
+078	-107	5	3.04±0.17	0.183±0.020	3.881±0.132	0.055±0.009	...	2.90±0.16	0.375±0.021	0.729±0.033	0.064±0.009	0.21±0.06	128
-068	-079	3	3.64±0.18	0.391±0.019	4.552±0.138	0.060±0.004	0.014±0.002	2.82±0.14	0.350±0.014	0.526±0.021	0.070±0.005	0.10±0.05	114
+080	-110	6	4.83±0.26	...	3.683±0.123	0.107±0.008	...	2.95±0.17	0.452±0.022	0.859±0.037	0.057±0.007	0.01±0.06	59
+017	-119	5	2.68±0.14	0.134±0.013	3.762±0.120	0.042±0.004	...	2.97±0.16	0.314±0.014	0.451±0.019	0.074±0.005	0.26±0.05	142
+089	-107	6	3.24±0.16	...	5.371±0.165	0.038±0.003	0.013±0.002	2.94±0.15	0.230±0.010	0.392±0.016	0.065±0.004	0.31±0.05	34
+116	-098	6	3.11±0.15	0.390±0.018	4.681±0.140	0.047±0.002	0.014±0.001	2.83±0.14	0.270±0.011	0.447±0.017	0.066±0.004	0.21±0.05	130
-145	+104	1	5.32±0.31	...	2.612±0.098	0.027±0.002	0.013±0.002	2.79±0.17	0.469±0.026	0.772±0.039	...	0.00±0.06	26
-151	+102	1	1.95±0.10	0.465±0.023	7.003±0.212	0.027±0.002	0.013±0.002	2.84±0.15	0.178±0.008	0.248±0.010	0.062±0.004	0.19±0.05	26
IC 2458													
+002	-006	1	2.47±0.12	0.523±0.026	6.455±0.197	0.030±0.002	0.017±0.001	2.79±0.14	0.166±0.007	0.297±0.011	0.075±0.005	0.30±0.05	75
-028	-007	1	2.24±0.18	...	3.469±0.169	2.91±0.23	0.090±0.015	0.408±0.028	...	0.00±0.08	171

TABLE 3. (continued)

Offsets		Slit No.	[OII]	[NeIII]	[OIII]	[OI]	[SIII]	H α	[NII]	[SII]	[ArIII]	$c_{H\beta}$	EW (H β)
E-W	N-S		3727+3729	3869	4959+5007	6300	6312	6563	6548+6583	6717+6731	7136		
-033	-007	1	1.23±0.07	0.278±0.021	6.338±0.208	0.039±0.003	0.014±0.002	2.72±0.15	0.076±0.004	0.165±0.008	0.038±0.003	0.37±0.06	217
NGC 2820													
+001	+001	1	5.32±0.62	...	1.165±0.144 ^a	0.126±0.020	...	2.86±0.35	1.105±0.109	1.077±0.098	...	1.16±0.12	7
+021	+011	1	2.01±0.14	...	2.000±0.087	2.85±0.19	0.679±0.037	0.622±0.032	0.049±0.006	0.68±0.07	40
-018	-009	1	3.32±0.44	...	2.490±0.218	2.86±0.37	0.764±0.085	0.874±0.087	...	1.11±0.12	12
-025	-013	1	3.64±0.32	...	3.475±0.193	0.100±0.014	...	2.93±0.26	0.612±0.048	0.782±0.055	...	0.61±0.09	14
NGC 2903													
-062	-085	1	3.18±0.24	...	1.581±0.090	2.86±0.22	1.361±0.088	0.948±0.060	...	0.67±0.08	3
-065	-073	1	3.86±0.39	...	0.148±0.085 ^a	2.86±0.17	1.290±0.118	1.062±0.091	...	0.64±0.10	2
-067	-061	1	3.36±0.18	...	0.808±0.042	2.86±0.30	1.218±0.061	0.832±0.041	0.032±0.010	0.55±0.06	12
-060	-100	1	3.79±0.20	...	0.327±0.035 ^a	2.86±0.17	1.310±0.063	1.030±0.047	...	0.64±0.06	7
+171	+196	2	3.50±0.14	...	1.885±0.044	2.80±0.13	0.778±0.028	0.514±0.018	0.081±0.005	0.36±0.05	161
+171	+226	2	2.90±0.13	...	2.069±0.056	2.86±0.14	0.712±0.030	0.478±0.019	0.080±0.006	0.22±0.05	78
+171	+232	2	4.24±0.25	...	0.683±0.046	2.86±0.19	0.919±0.053	0.883±0.048	0.067±0.014	0.21±0.06	46
+171	+236	2	3.83±0.20	...	0.614±0.030 ^a	2.86±0.16	0.953±0.051	0.809±0.041	...	0.34±0.06	78
+171	+243	2	3.51±0.17	...	0.644±0.030	2.86±0.16	0.892±0.043	0.635±0.031	0.058±0.012	0.14±0.06	43
NGC 3184													
-058	-007	2	0.39±0.02	...	0.107±0.016	2.86±0.14	0.985±0.041	0.488±0.019	...	0.10±0.05	24
-064	-006	2	0.63±0.05	...	0.191±0.030 ^a	0.074±0.006	...	2.86±0.17	1.371±0.066	0.601±0.027	0.019±0.004	0.69±0.06	30
-080	-005	2	0.69±0.03	...	0.224±0.013	2.86±0.14	1.180±0.047	0.525±0.019	...	0.18±0.05	39
+085	-004	4	0.98±0.06	...	0.221±0.030 ^a	2.86±0.17	1.368±0.064	0.662±0.031	...	0.43±0.06	600
+079	+035	4	0.74±0.04	...	0.129±0.013 ^a	0.042±0.004	...	2.86±0.14	1.131±0.044	0.581±0.022	...	0.23±0.05	38
+059	-079	5	1.21±0.05	...	0.191±0.015	2.87±0.14	1.243±0.048	0.681±0.025	0.019±0.004	0.28±0.05	35
+074	+064	4	1.10±0.07	...	0.390±0.035 ^a	2.86±0.17	1.209±0.056	0.796±0.037	...	0.35±0.06	12
+092	-093	5	1.61±0.07	...	0.196±0.011	2.86±0.13	1.277±0.047	0.835±0.029	0.020±0.002	0.24±0.05	60
+005	+135	3	2.62±0.11	...	1.053±0.024	2.86±0.13	1.154±0.043	0.713±0.025	0.053±0.003	0.24±0.05	66
-002	+136	3	1.63±0.11	...	0.172±0.048 ^a	2.86±0.20	1.083±0.066	0.709±0.043	...	0.05±0.07	100
-017	+137	3	1.69±0.07	...	0.352±0.013	2.86±0.14	1.221±0.048	0.633±0.024	...	0.38±0.05	128
+111	-102	5	3.94±0.48	...	1.090±0.141 ^a	2.86±0.37	1.267±0.139	0.886±0.092	...	0.65±0.12	12
-119	-121	1	2.30±0.12	...	0.304±0.031 ^a	2.86±0.16	1.189±0.057	0.742±0.035	0.026±0.010	0.05±0.06	69
-113	-127	1	1.84±0.09	0.219±0.021	3.747±0.100	2.78±0.14	0.638±0.028	0.272±0.012	0.118±0.008	0.53±0.05	55
-101	-137	1	2.35±0.13	...	1.203±0.049	2.86±0.17	0.993±0.049	0.400±0.021	0.068±0.007	0.27±0.06	112
-110	-130	1	2.69±0.15	...	0.890±0.041	2.82±0.16	1.063±0.051	0.501±0.025	0.049±0.008	0.27±0.06	45
-095	-142	1	2.46±0.11	...	2.117±0.057	2.80±0.14	0.788±0.033	0.754±0.029	0.061±0.007	0.10±0.05	55
NGC 4395													

TABLE 3. (continued)

Offsets		Slit No.	[OII]	[NeIII]	[OIII]	[OI]	[SIII]	H α	[NII]	[SII]	[ArIII]	$c_{H\beta}$	EW (H β)
E-W	N-S		3727+3729	3869	4959+5007	6300	6312	6563	6548+6583	6717+6731	7136		
-003	-003	6	2.03±0.10	0.927±0.044	7.809±0.281	0.452±0.022	0.020±0.001	2.71±0.14	0.648±0.035	0.746±0.029	0.075±0.005	0.62±0.05	80
+061	-029	8	4.08±0.19	...	1.529±0.044	0.031±0.002	...	2.72±0.14	0.381±0.002	0.636±0.024	0.054±0.004	0.30±0.05	67
+099	-029	8	3.20±0.30	...	4.076±0.217	2.86±0.33	0.460±0.222	0.891±0.228	...	0.20±0.11	195
+002	-127	7	2.88±0.13	0.176±0.008	3.798±0.105	0.017±0.001	0.018±0.001	2.71±0.14	0.244±0.009	0.292±0.011	0.090±0.005	0.35±0.05	262
-075	-117	4	4.46±0.21	0.146±0.011	2.381±0.068	2.82±0.15	0.297±0.013	0.678±0.027	0.050±0.003	0.27±0.05	44
+088	-119	9	2.60±0.12	0.336±0.019	4.076±0.118	2.79±0.15	0.237±0.011	0.509±0.020	0.075±0.005	0.21±0.05	116
-167	-093	3	3.67±0.17	0.462±0.023	5.217±0.149	2.72±0.14	0.232±0.011	0.620±0.024	0.091±0.006	0.30±0.05	92
+118	+206	10	3.07±0.14	0.092±0.005	2.551±0.071	0.026±0.001	0.022±0.001	2.77±0.14	0.309±0.013	0.371±0.014	0.076±0.004	0.16±0.05	180
+195	-159	11	4.34±0.21	...	3.217±0.092	0.029±0.003	0.008±0.003	2.35±0.12	0.211±0.010	0.382±0.016	0.069±0.005	0.50±0.05	286
+200	+141	12	3.94±0.18	0.187±0.010	3.037±0.086	2.85±0.15	0.326±0.014	0.529±0.021	0.085±0.005	0.15±0.05	187
-226	+237	2	2.72±0.13	0.246±0.014	4.519±0.130	2.68±0.14	0.195±0.010	0.285±0.012	0.086±0.006	0.22±0.05	148
-272	+186	1	3.06±0.14	0.293±0.015	4.968±0.139	0.028±0.002	0.013±0.002	2.73±0.14	0.196±0.008	0.377±0.014	0.080±0.005	0.19±0.05	125
NGC 5457													
-075	+028	7	0.43±0.03	...	0.168±0.017 ^a	2.86±0.15	1.173±0.051	0.564±0.024	...	0.62±0.05	255
-106	+028	7	0.94±0.09	...	0.461±0.055	2.82±0.21	1.122±0.070	0.576±0.035	...	0.66±0.08	28
-347	+276	4	0.98±0.04	0.523±0.023	7.906±0.219	0.023±0.001	0.016±0.001	2.83±0.14	0.149±0.006	0.176±0.006	0.089±0.005	0.18±0.05	222
-459	-053	2	3.00±0.14	0.280±0.013	3.996±0.112	0.032±0.002	0.012±0.001	2.77±0.14	0.269±0.010	0.347±0.014	0.064±0.004	0.21±0.05	132
+271	-393	11	3.88±0.18	...	1.494±0.044	...	0.010±0.002	2.78±0.14	0.387±0.017	0.387±0.016	0.051±0.004	0.19±0.05	128
-276	-417	6	3.94±0.19	0.094±0.010	1.299±0.040	2.79±0.15	0.253±0.016	0.534±0.021	0.034±0.003	0.25±0.05	105
-037	-532	8	4.01±0.23	...	2.495±0.090	2.78±0.18	0.321±0.020	0.390±0.021	0.037±0.008	0.25±0.06	91
-250	+484	5	2.99±0.14	0.141±0.012	2.544±0.076	2.67±0.14	0.241±0.011	0.441±0.019	0.041±0.005	0.23±0.05	69
-398	-436	3	2.05±0.09	0.338±0.015	5.311±0.147	0.023±0.001	0.015±0.001	2.77±0.14	0.136±0.005	0.206±0.008	0.059±0.003	0.15±0.05	172
-291	+489	5	4.24±0.20	0.122±0.008	1.964±0.056	2.69±0.14	0.332±0.014	0.559±0.022	0.041±0.003	0.23±0.05	67
-499	+300	1	3.57±0.18	0.274±0.022	3.248±0.102	0.015±0.005	...	2.70±0.15	0.314±0.016	0.423±0.019	0.046±0.005	0.21±0.06	87
+010	+885	10	2.13±0.10	0.336±0.016	4.837±0.135	0.035±0.002	0.014±0.001	2.68±0.14	0.135±0.005	0.247±0.009	0.040±0.003	0.12±0.05	101
+005	+887	10	3.10±0.15	0.270±0.016	2.377±0.069	0.023±0.002	...	2.72±0.14	0.179±0.008	0.316±0.013	0.035±0.003	0.32±0.05	61

^aOnly $\lambda 5007$ detected- sum derived assuming $\lambda 5007/\lambda 4959 = 2.88$

TABLE 4. HII Region Ratios

Offsets		r_0	Slit	[OIII]	[SII]	Log	Log	Log	Log	Log
E-W	N-S	[arcsec]	No.	ratio	ratio	([OII]+[OIII])	([OIII]/[OII])	([NII]/H α)	([NII]/[OII])	([SII]/[OII])
NGC 0628										
+081	-140	172.6	3	...	1.57 \pm 0.10	0.566 \pm 0.011	-0.169 \pm 0.020	-0.626 \pm 0.025	-0.511 \pm 0.023	-0.712 \pm 0.022
+062	-158	178.8	3	...	1.56 \pm 0.18	0.426 \pm 0.026	-0.817 \pm 0.053	-0.474 \pm 0.040	-0.382 \pm 0.039	-0.523 \pm 0.039
+047	-172	185.9	3	...	1.59 \pm 0.13	0.562 \pm 0.015	-0.403 \pm 0.024	-0.516 \pm 0.028	-0.511 \pm 0.027	-0.617 \pm 0.026
+044	-175	187.7	3	...	1.54 \pm 0.11	0.658 \pm 0.011	-0.078 \pm 0.021	-0.599 \pm 0.026	-0.535 \pm 0.024	-0.727 \pm 0.024
+180	-008	195.5	4	...	1.92 \pm 0.14	0.473 \pm 0.014	-0.504 \pm 0.023	-0.512 \pm 0.026	-0.410 \pm 0.025	-0.511 \pm 0.024
+178	-052	203.3	4	...	1.85 \pm 0.12	0.481 \pm 0.011	-0.219 \pm 0.019	-0.588 \pm 0.025	-0.408 \pm 0.023	-0.593 \pm 0.023
-086	+186	216.9	2	...	1.45 \pm 0.10	0.701 \pm 0.010	-0.155 \pm 0.019	-0.612 \pm 0.024	-0.634 \pm 0.022	-0.914 \pm 0.022
-075	+200	224.6	2	...	1.58 \pm 0.14	0.742 \pm 0.017	-0.438 \pm 0.027	-0.529 \pm 0.032	-0.680 \pm 0.030	-0.821 \pm 0.030
+203	-041	226.4	5	...	1.52 \pm 0.12	0.631 \pm 0.014	-0.087 \pm 0.027	-0.572 \pm 0.030	-0.371 \pm 0.030	-0.505 \pm 0.029
-073	+203	226.5	2	...	1.52 \pm 0.11	0.673 \pm 0.013	-0.293 \pm 0.022	-0.560 \pm 0.028	-0.598 \pm 0.026	-0.709 \pm 0.025
-069	+208	229.6	2	...	1.36 \pm 0.09	0.748 \pm 0.010	-0.026 \pm 0.019	-0.611 \pm 0.025	-0.636 \pm 0.023	-0.761 \pm 0.022
+254	-043	281.3	6	...	1.59 \pm 0.11	0.775 \pm 0.011	-0.226 \pm 0.020	-0.527 \pm 0.025	-0.658 \pm 0.023	-0.630 \pm 0.023
+256	-041	283.0	5	...	1.43 \pm 0.12	0.860 \pm 0.016	-0.282 \pm 0.028	-0.549 \pm 0.032	-0.777 \pm 0.031	-0.696 \pm 0.030
-232	+112	283.0	1	...	1.70 \pm 0.19	0.707 \pm 0.022	-0.689 \pm 0.037	-0.701 \pm 0.040	-0.871 \pm 0.038	-0.793 \pm 0.036
+262	-041	289.4	5	...	1.38 \pm 0.14	0.804 \pm 0.019	-0.262 \pm 0.033	-0.537 \pm 0.037	-0.700 \pm 0.036	-0.639 \pm 0.035
+264	-037	290.7	6	...	1.60 \pm 0.14	0.804 \pm 0.012	-0.068 \pm 0.024	-0.692 \pm 0.031	-0.772 \pm 0.029	-0.655 \pm 0.028
+265	-041	292.6	5	...	1.51 \pm 0.16	0.869 \pm 0.015	0.074 \pm 0.031	-0.726 \pm 0.036	-0.804 \pm 0.035	-0.733 \pm 0.034
-227	+148	297.2	1	...	1.30 \pm 0.11	0.800 \pm 0.012	-0.061 \pm 0.024	-0.815 \pm 0.031	-0.899 \pm 0.029	-0.900 \pm 0.027
+292	-020	318.0	6	...	1.56 \pm 0.11	0.895 \pm 0.009	0.335 \pm 0.020	-1.083 \pm 0.026	-1.070 \pm 0.024	-1.083 \pm 0.023
NGC 0925										
+002	-002	3.6	10	...	1.53 \pm 0.12	0.436 \pm 0.013	-0.214 \pm 0.023	-0.595 \pm 0.028	-0.368 \pm 0.026	-0.404 \pm 0.026
-005	+000	5.2	10	...	1.54 \pm 0.11	0.487 \pm 0.014	-0.531 \pm 0.021	-0.504 \pm 0.026	-0.421 \pm 0.024	-0.406 \pm 0.023
-008	+000	8.4	10	...	1.47 \pm 0.10	0.579 \pm 0.013	-0.497 \pm 0.020	-0.524 \pm 0.026	-0.521 \pm 0.024	-0.518 \pm 0.022
+010	-004	11.1	10	...	1.50 \pm 0.11	0.576 \pm 0.014	-0.551 \pm 0.022	-0.497 \pm 0.026	-0.505 \pm 0.024	-0.493 \pm 0.024
+015	-005	16.0	10	...	1.44 \pm 0.10	0.412 \pm 0.012	-0.204 \pm 0.021	-0.577 \pm 0.026	-0.316 \pm 0.024	-0.295 \pm 0.023
+030	-008	31.1	10	...	1.43 \pm 0.10	0.573 \pm 0.016	-0.769 \pm 0.025	-0.480 \pm 0.027	-0.523 \pm 0.025	-0.567 \pm 0.024
+036	-010	37.5	10	...	1.41 \pm 0.10	0.633 \pm 0.014	-0.583 \pm 0.021	-0.540 \pm 0.026	-0.616 \pm 0.024	-0.617 \pm 0.023
+042	-011	43.5	10	...	1.38 \pm 0.10	0.612 \pm 0.013	-0.345 \pm 0.022	-0.577 \pm 0.027	-0.570 \pm 0.026	-0.574 \pm 0.025
+087	-031	94.1	12	...	1.56 \pm 0.12	0.758 \pm 0.014	-0.117 \pm 0.026	-0.709 \pm 0.029	-0.794 \pm 0.028	-0.693 \pm 0.028
-012	-066	120.5	9	317 \pm 60	1.39 \pm 0.11	0.885 \pm 0.011	0.304 \pm 0.025	-0.992 \pm 0.028	-0.945 \pm 0.028	-0.876 \pm 0.027
-047	-058	124.2	9	...	1.64 \pm 0.12	0.786 \pm 0.016	-0.471 \pm 0.025	-0.679 \pm 0.028	-0.899 \pm 0.027	-0.708 \pm 0.027
+135	-016	137.2	12	...	1.51 \pm 0.12	0.835 \pm 0.014	-0.181 \pm 0.025	-0.813 \pm 0.028	-0.982 \pm 0.027	-0.724 \pm 0.027
-109	+062	137.6	6	...	1.55 \pm 0.11	0.728 \pm 0.010	0.052 \pm 0.020	-0.858 \pm 0.026	-0.801 \pm 0.024	-0.738 \pm 0.024
+137	+011	149.4	13	...	1.42 \pm 0.15	0.815 \pm 0.016	0.061 \pm 0.033	-0.941 \pm 0.041	-0.972 \pm 0.041	-0.621 \pm 0.037

TABLE 4. (continued)

Offsets		r_0	Slit	[OIII]	[SII]	Log	Log	Log	Log	Log
E-W	N-S	[arcsec]	No.	ratio	ratio	([OII]+[OIII])	([OIII]/[OII])	([NII]/H α)	([NII]/[OII])	([SII]/[OII])
-137	+056	153.1	6	...	1.26 \pm 0.11	0.769 \pm 0.013	-0.158 \pm 0.024	-0.766 \pm 0.030	-0.840 \pm 0.029	-0.903 \pm 0.028
-145	-006	154.8	5	...	1.50 \pm 0.10	0.833 \pm 0.009	0.178 \pm 0.019	-0.920 \pm 0.025	-0.932 \pm 0.023	-0.857 \pm 0.022
-080	+087	156.3	7	...	1.46 \pm 0.11	0.833 \pm 0.015	-0.397 \pm 0.025	-0.755 \pm 0.028	-0.996 \pm 0.027	-0.863 \pm 0.027
-114	+087	170.2	7	...	1.46 \pm 0.12	0.876 \pm 0.015	-0.262 \pm 0.026	-0.802 \pm 0.030	-1.032 \pm 0.029	-0.724 \pm 0.028
+161	+015	177.0	13	...	1.55 \pm 0.12	0.778 \pm 0.014	-0.220 \pm 0.026	-0.936 \pm 0.029	-1.057 \pm 0.028	-0.815 \pm 0.028
+174	+018	192.5	13	...	1.68 \pm 0.18	0.760 \pm 0.022	-0.633 \pm 0.035	-0.948 \pm 0.043	-1.166 \pm 0.042	-0.852 \pm 0.036
+182	+019	201.5	13	...	1.39 \pm 0.11	0.847 \pm 0.011	0.270 \pm 0.025	-1.226 \pm 0.029	-1.165 \pm 0.028	-0.956 \pm 0.028
-187	-017	205.3	5	...	1.38 \pm 0.09	0.829 \pm 0.010	0.013 \pm 0.019	-0.893 \pm 0.025	-0.958 \pm 0.023	-0.743 \pm 0.022
-192	-018	211.1	3	...	1.46 \pm 0.12	0.870 \pm 0.013	0.039 \pm 0.026	-0.910 \pm 0.029	-1.013 \pm 0.029	-0.679 \pm 0.028
-192	-018	211.1	5	...	1.41 \pm 0.10	0.864 \pm 0.009	0.025 \pm 0.019	-0.947 \pm 0.025	-1.068 \pm 0.023	-0.849 \pm 0.022
-198	-013	214.1	3	...	1.36 \pm 0.10	0.896 \pm 0.012	0.143 \pm 0.025	-0.974 \pm 0.029	-1.046 \pm 0.029	-0.737 \pm 0.028
+209	-006	216.5	15	...	1.37 \pm 0.13	0.802 \pm 0.019	-0.429 \pm 0.030	-0.894 \pm 0.036	-1.107 \pm 0.035	-0.938 \pm 0.033
-200	-020	220.8	5	...	1.38 \pm 0.09	0.818 \pm 0.009	0.047 \pm 0.019	-0.842 \pm 0.024	-0.879 \pm 0.022	-0.725 \pm 0.022
+217	-006	224.9	15	...	1.58 \pm 0.13	0.902 \pm 0.012	0.202 \pm 0.026	-1.082 \pm 0.032	-1.119 \pm 0.032	-0.772 \pm 0.029
+156	-114	226.4	14	...	1.40 \pm 0.11	0.819 \pm 0.015	-0.295 \pm 0.025	-0.816 \pm 0.029	-1.006 \pm 0.028	-0.778 \pm 0.027
-220	+004	228.7	3	...	1.42 \pm 0.11	0.775 \pm 0.015	-0.299 \pm 0.025	-0.862 \pm 0.028	-1.005 \pm 0.028	-0.837 \pm 0.027
+221	-006	229.0	15	...	1.54 \pm 0.14	0.954 \pm 0.013	0.437 \pm 0.028	-1.042 \pm 0.034	-0.972 \pm 0.034	-0.647 \pm 0.032
+052	+130	249.1	11	...	1.39 \pm 0.12	0.896 \pm 0.012	0.122 \pm 0.026	-1.119 \pm 0.031	-1.197 \pm 0.030	-0.976 \pm 0.029
-250	+019	255.6	2	...	1.43 \pm 0.11	0.785 \pm 0.011	0.252 \pm 0.025	-1.025 \pm 0.028	-0.915 \pm 0.028	-0.735 \pm 0.027
+206	-114	256.8	14	...	1.37 \pm 0.12	0.803 \pm 0.014	-0.056 \pm 0.028	-0.896 \pm 0.032	-0.974 \pm 0.031	-0.714 \pm 0.030
+019	+143	258.7	11	...	1.37 \pm 0.10	0.948 \pm 0.012	0.308 \pm 0.026	-1.104 \pm 0.030	-1.128 \pm 0.030	-0.878 \pm 0.028
-174	+140	269.3	4	...	1.48 \pm 0.12	0.866 \pm 0.013	0.001 \pm 0.026	-0.998 \pm 0.031	-1.112 \pm 0.030	-0.788 \pm 0.028
-262	+011	270.2	1	...	1.34 \pm 0.17	0.869 \pm 0.020	-0.253 \pm 0.035	-0.986 \pm 0.054	-1.166 \pm 0.053	-0.853 \pm 0.040
-272	+016	279.2	1	...	1.35 \pm 0.12	0.840 \pm 0.017	-0.297 \pm 0.029	-0.957 \pm 0.036	-1.163 \pm 0.036	-0.748 \pm 0.032
-274	+010	283.1	2	...	1.40 \pm 0.11	0.881 \pm 0.012	0.012 \pm 0.025	-0.949 \pm 0.028	-1.070 \pm 0.028	-0.695 \pm 0.027
-285	+023	291.1	1	...	1.43 \pm 0.12	0.837 \pm 0.016	-0.343 \pm 0.027	-0.968 \pm 0.033	-1.186 \pm 0.032	-0.873 \pm 0.029
-159	+162	294.3	4	...	1.58 \pm 0.16	0.799 \pm 0.021	-0.570 \pm 0.033	-0.854 \pm 0.040	-1.063 \pm 0.039	-0.639 \pm 0.035
-308	+035	313.2	1	...	1.40 \pm 0.11	0.812 \pm 0.017	-0.522 \pm 0.026	-0.812 \pm 0.030	-0.997 \pm 0.029	-0.687 \pm 0.028
-149	+177	314.0	4	...	1.51 \pm 0.12	0.764 \pm 0.015	-0.323 \pm 0.026	-0.947 \pm 0.030	-1.086 \pm 0.030	-0.809 \pm 0.028
-022	+227	396.8	8	257 \pm 94	1.48 \pm 0.13	0.886 \pm 0.012	0.442 \pm 0.026	-1.276 \pm 0.033	-1.140 \pm 0.032	-0.898 \pm 0.029
NGC 1068										
+111	-088	159.5	1	...	1.21 \pm 0.13	0.344 \pm 0.024	-0.397 \pm 0.045	-0.297 \pm 0.038	-0.038 \pm 0.038	-0.346 \pm 0.038
NGC 1232										
+062	+004	62.2	4	...	1.52 \pm 0.12	0.223 \pm 0.019	-0.857 \pm 0.033	-0.394 \pm 0.029	-0.097 \pm 0.028	-0.326 \pm 0.028
+075	-001	75.0	5	...	1.55 \pm 0.16	0.484 \pm 0.024	-0.957 \pm 0.052	-0.337 \pm 0.035	-0.319 \pm 0.034	-0.521 \pm 0.034

TABLE 4. (continued)

Offsets		r_0	Slit	[OIII]	[SII]	Log	Log	Log	Log	Log
E-W	N-S	[arcsec]	No.	ratio	ratio	([OII]+[OIII])	([OIII]/[OII])	([NII]/H α)	([NII]/[OII])	([SII]/[OII])
+075	-012	76.2	5	...	1.31 \pm 0.11	0.521 \pm 0.021	-0.848 \pm 0.034	-0.301 \pm 0.031	-0.307 \pm 0.030	-0.530 \pm 0.030
+059	+058	88.9	4	...	1.38 \pm 0.10	0.253 \pm 0.018	-0.696 \pm 0.025	-0.329 \pm 0.028	-0.043 \pm 0.027	-0.352 \pm 0.027
-103	-021	105.8	1	...	1.47 \pm 0.11	0.466 \pm 0.017	-0.543 \pm 0.025	-0.386 \pm 0.028	-0.290 \pm 0.028	-0.497 \pm 0.027
-103	+022	106.0	1	...	1.50 \pm 0.13	0.622 \pm 0.017	-0.466 \pm 0.027	-0.429 \pm 0.030	-0.466 \pm 0.030	-0.664 \pm 0.029
+021	+091	106.5	3	...	1.34 \pm 0.10	0.589 \pm 0.015	-0.274 \pm 0.025	-0.449 \pm 0.028	-0.396 \pm 0.027	-0.640 \pm 0.026
+004	-101	115.9	2	...	1.35 \pm 0.10	0.619 \pm 0.016	-0.512 \pm 0.025	-0.379 \pm 0.028	-0.422 \pm 0.027	-0.640 \pm 0.026
+057	+098	126.0	4	...	1.40 \pm 0.11	0.756 \pm 0.017	-0.413 \pm 0.027	-0.455 \pm 0.030	-0.602 \pm 0.029	-0.603 \pm 0.029
+056	+106	133.9	4	...	1.58 \pm 0.25	0.720 \pm 0.023	-0.216 \pm 0.041	-0.600 \pm 0.049	-0.678 \pm 0.048	-0.677 \pm 0.047
+147	-030	151.0	8	...	1.45 \pm 0.11	0.605 \pm 0.016	-0.417 \pm 0.026	-0.415 \pm 0.029	-0.434 \pm 0.028	-0.585 \pm 0.028
+117	+084	151.6	7	...	1.50 \pm 0.12	0.692 \pm 0.014	-0.134 \pm 0.025	-0.644 \pm 0.029	-0.639 \pm 0.028	-0.671 \pm 0.028
+099	-101	152.4	6	...	1.43 \pm 0.11	0.731 \pm 0.015	-0.273 \pm 0.026	-0.542 \pm 0.030	-0.631 \pm 0.029	-0.830 \pm 0.028
+093	-110	156.7	6	...	1.51 \pm 0.12	0.781 \pm 0.015	-0.269 \pm 0.026	-0.542 \pm 0.030	-0.679 \pm 0.029	-0.729 \pm 0.029
+147	-065	164.8	8	...	1.68 \pm 0.16	0.702 \pm 0.018	-0.317 \pm 0.030	-0.592 \pm 0.034	-0.664 \pm 0.033	-0.676 \pm 0.033
+135	+114	187.9	7	169 \pm 27	1.40 \pm 0.11	0.853 \pm 0.011	0.444 \pm 0.025	-0.946 \pm 0.029	-0.779 \pm 0.028	-0.878 \pm 0.028
NGC 1637										
-001	-000	1.2	3	...	1.01 \pm 0.08	0.094 \pm 0.019	-0.611 \pm 0.034	-0.093 \pm 0.029	0.374 \pm 0.028	-0.058 \pm 0.028
+016	-001	19.5	4	...	1.22 \pm 0.25	0.488 \pm 0.059	-1.162 \pm 0.250	-0.239 \pm 0.074	-0.242 \pm 0.076	-0.548 \pm 0.075
-019	-009	23.9	2	...	1.24 \pm 0.29	0.489 \pm 0.054	-0.400 \pm 0.103	-0.218 \pm 0.082	-0.105 \pm 0.086	-0.525 \pm 0.086
-020	-000	24.2	2	...	1.34 \pm 0.14	-0.317 \pm 0.049	-0.695 \pm 0.181	-0.360 \pm 0.036	0.493 \pm 0.053	0.154 \pm 0.052
-001	+026	26.6	3	...	1.43 \pm 0.12	0.215 \pm 0.018	-0.499 \pm 0.030	-0.309 \pm 0.030	0.052 \pm 0.030	-0.245 \pm 0.029
+009	-026	29.6	4	...	1.30 \pm 0.11	0.214 \pm 0.023	-0.863 \pm 0.056	-0.323 \pm 0.032	-0.024 \pm 0.032	-0.294 \pm 0.032
+022	+018	30.7	4	...	1.38 \pm 0.12	0.162 \pm 0.022	-1.108 \pm 0.074	-0.359 \pm 0.030	-0.032 \pm 0.030	-0.358 \pm 0.030
+026	+018	34.8	5	...	1.26 \pm 0.15	0.214 \pm 0.031	-0.840 \pm 0.100	-0.340 \pm 0.040	-0.039 \pm 0.041	-0.301 \pm 0.041
-017	-031	35.8	2	...	1.41 \pm 0.13	-0.110 \pm 0.030	-0.811 \pm 0.105	-0.371 \pm 0.033	0.257 \pm 0.037	-0.078 \pm 0.036
+051	+012	61.7	7	...	1.56 \pm 0.15	-0.168 \pm 0.032	-0.613 \pm 0.102	-0.317 \pm 0.034	0.379 \pm 0.038	0.126 \pm 0.038
+053	-007	65.2	7	...	1.25 \pm 0.13	-0.675 \pm 0.089	-0.445 \pm 0.265	-0.379 \pm 0.035	0.881 \pm 0.084	0.348 \pm 0.084
-055	-011	66.3	1	...	1.33 \pm 0.17	0.427 \pm 0.030	-0.634 \pm 0.065	-0.284 \pm 0.045	-0.164 \pm 0.045	-0.467 \pm 0.045
+047	-031	67.7	6	...	1.44 \pm 0.11	0.118 \pm 0.019	-0.933 \pm 0.030	-0.324 \pm 0.029	0.046 \pm 0.028	-0.342 \pm 0.027
+047	+046	69.9	7	...	1.46 \pm 0.13	0.210 \pm 0.025	-1.011 \pm 0.077	-0.263 \pm 0.033	0.024 \pm 0.034	-0.372 \pm 0.033
-055	-032	71.0	1	...	1.77 \pm 0.23	0.279 \pm 0.031	-0.523 \pm 0.068	-0.248 \pm 0.044	0.039 \pm 0.046	-0.206 \pm 0.046
+058	-054	93.3	8	...	1.51 \pm 0.12	0.672 \pm 0.018	-0.675 \pm 0.027	-0.418 \pm 0.029	-0.551 \pm 0.029	-0.692 \pm 0.028
NGC 2403										
+186	-177	262.4	4	...	1.45 \pm 0.10	0.913 \pm 0.010	0.118 \pm 0.021	-0.610 \pm 0.027	-0.703 \pm 0.025	-0.499 \pm 0.024
+178	-203	286.4	4	...	1.41 \pm 0.10	0.698 \pm 0.009	0.150 \pm 0.019	-0.940 \pm 0.024	-0.809 \pm 0.022	-0.924 \pm 0.023
+176	-211	295.2	4	...	1.33 \pm 0.12	0.683 \pm 0.021	-0.819 \pm 0.038	-0.684 \pm 0.034	-0.708 \pm 0.033	-0.567 \pm 0.031

TABLE 4. (continued)

Offsets		r_0	Slit	[OIII]	[SII]	Log	Log	Log	Log	Log
E-W	N-S	[arcsec]	No.	ratio	ratio	([OII]+[OIII])	([OIII]/[OII])	([NII]/H α)	([NII]/[OII])	([SII]/[OII])
+166	-229	315.9	4	...	1.47 \pm 0.11	0.779 \pm 0.013	-0.281 \pm 0.022	-0.748 \pm 0.028	-0.886 \pm 0.026	-0.697 \pm 0.024
+356	-195	414.2	5	...	1.44 \pm 0.10	0.899 \pm 0.010	0.020 \pm 0.020	-0.837 \pm 0.025	-0.968 \pm 0.023	-0.754 \pm 0.023
+360	-190	417.5	5	...	1.40 \pm 0.10	0.705 \pm 0.014	-0.474 \pm 0.021	-0.795 \pm 0.026	-0.919 \pm 0.024	-0.627 \pm 0.024
+377	-163	435.2	5	...	1.36 \pm 0.09	0.787 \pm 0.010	-0.047 \pm 0.020	-0.908 \pm 0.025	-0.984 \pm 0.023	-0.898 \pm 0.023
+376	-106	446.8	6	...	1.44 \pm 0.09	0.843 \pm 0.009	0.170 \pm 0.019	-1.094 \pm 0.024	-1.186 \pm 0.022	-1.135 \pm 0.022
-377	+104	448.9	2	...	1.46 \pm 0.10	0.753 \pm 0.011	-0.167 \pm 0.020	-0.881 \pm 0.025	-0.952 \pm 0.023	-0.911 \pm 0.022
-105	-218	452.0	3	...	1.38 \pm 0.17	0.581 \pm 0.016	-0.246 \pm 0.029	-1.001 \pm 0.039	-0.995 \pm 0.038	-0.930 \pm 0.035
-105	-224	461.5	3	...	1.56 \pm 0.13	0.652 \pm 0.015	-0.536 \pm 0.024	-0.889 \pm 0.029	-1.016 \pm 0.027	-0.923 \pm 0.027
-381	+082	464.5	2	...	1.38 \pm 0.11	0.815 \pm 0.012	-0.114 \pm 0.022	-0.915 \pm 0.028	-1.041 \pm 0.026	-0.938 \pm 0.025
+383	-056	482.7	6	...	1.61 \pm 0.13	0.809 \pm 0.011	-0.030 \pm 0.021	-1.015 \pm 0.027	-1.176 \pm 0.025	-1.182 \pm 0.025
-104	-256	511.2	3	...	1.35 \pm 0.11	0.744 \pm 0.014	-0.452 \pm 0.022	-0.992 \pm 0.029	-1.149 \pm 0.027	-1.069 \pm 0.026
-425	-002	585.8	1	...	1.47 \pm 0.11	0.773 \pm 0.012	-0.190 \pm 0.021	-0.999 \pm 0.028	-1.152 \pm 0.026	-0.925 \pm 0.024
-423	-010	590.3	1	...	1.47 \pm 0.11	0.757 \pm 0.011	-0.087 \pm 0.022	-1.068 \pm 0.030	-1.177 \pm 0.028	-1.004 \pm 0.025
-421	-017	594.1	1	...	1.59 \pm 0.12	0.694 \pm 0.016	-0.850 \pm 0.021	-0.924 \pm 0.028	-1.148 \pm 0.026	-0.990 \pm 0.024
NGC 2805										
-051	-009	60.8	2	...	1.38 \pm 0.10	0.578 \pm 0.013	-0.091 \pm 0.025	-0.668 \pm 0.028	-0.532 \pm 0.027	-0.598 \pm 0.027
+055	-026	61.5	6	...	1.45 \pm 0.12	0.787 \pm 0.015	-0.243 \pm 0.027	-0.654 \pm 0.030	-0.786 \pm 0.030	-0.788 \pm 0.029
+058	-022	63.4	6	...	1.40 \pm 0.11	0.713 \pm 0.016	-0.369 \pm 0.025	-0.596 \pm 0.029	-0.707 \pm 0.028	-0.684 \pm 0.027
-021	-045	65.3	3	...	1.55 \pm 0.13	0.651 \pm 0.016	-0.276 \pm 0.027	-0.582 \pm 0.031	-0.589 \pm 0.030	-0.708 \pm 0.029
+032	-056	68.8	6	...	1.48 \pm 0.13	0.794 \pm 0.017	-0.326 \pm 0.029	-0.655 \pm 0.032	-0.836 \pm 0.032	-0.792 \pm 0.031
-001	-079	97.2	4	...	1.40 \pm 0.11	0.737 \pm 0.012	0.015 \pm 0.025	-0.781 \pm 0.028	-0.759 \pm 0.028	-0.744 \pm 0.027
-005	-080	99.8	4	...	1.45 \pm 0.11	0.790 \pm 0.015	-0.270 \pm 0.025	-0.660 \pm 0.028	-0.813 \pm 0.028	-0.727 \pm 0.027
-041	-090	130.0	4	...	1.42 \pm 0.11	0.837 \pm 0.014	-0.239 \pm 0.025	-0.730 \pm 0.028	-0.910 \pm 0.027	-0.727 \pm 0.027
+037	-115	136.4	5	233 \pm 36	1.48 \pm 0.11	0.856 \pm 0.011	0.268 \pm 0.025	-1.018 \pm 0.028	-0.961 \pm 0.027	-0.735 \pm 0.027
+078	-107	137.6	5	...	1.48 \pm 0.13	0.840 \pm 0.013	0.106 \pm 0.028	-0.888 \pm 0.035	-0.909 \pm 0.034	-0.620 \pm 0.031
-068	-079	137.7	3	136 \pm 24	1.44 \pm 0.11	0.913 \pm 0.012	0.097 \pm 0.025	-0.906 \pm 0.028	-1.017 \pm 0.027	-0.840 \pm 0.027
+080	-110	141.3	6	...	1.40 \pm 0.12	0.930 \pm 0.015	-0.118 \pm 0.027	-0.815 \pm 0.032	-1.029 \pm 0.031	-0.750 \pm 0.030
+017	-119	142.3	5	...	1.42 \pm 0.12	0.809 \pm 0.012	0.148 \pm 0.027	-0.976 \pm 0.030	-0.931 \pm 0.030	-0.774 \pm 0.029
+089	-107	142.8	6	281 \pm 156	1.43 \pm 0.11	0.935 \pm 0.012	0.220 \pm 0.026	-1.107 \pm 0.030	-1.149 \pm 0.029	-0.917 \pm 0.028
+116	-098	152.3	6	156 \pm 11	1.38 \pm 0.10	0.892 \pm 0.012	0.177 \pm 0.025	-1.020 \pm 0.028	-1.062 \pm 0.028	-0.843 \pm 0.027
-145	+104	178.4	1	...	1.40 \pm 0.14	0.899 \pm 0.018	-0.309 \pm 0.030	-0.774 \pm 0.036	-1.054 \pm 0.035	-0.838 \pm 0.034
-151	+102	182.2	1	...	1.41 \pm 0.11	0.952 \pm 0.011	0.556 \pm 0.025	-1.202 \pm 0.030	-1.039 \pm 0.029	-0.895 \pm 0.028
IC 2458										
+002	-006	...	1	95 \pm 8	1.43 \pm 0.11	0.951 \pm 0.011	0.416 \pm 0.025	-1.226 \pm 0.029	-1.173 \pm 0.028	-0.921 \pm 0.027
-028	-007	...	1	...	1.32 \pm 0.18	0.757 \pm 0.019	0.190 \pm 0.040	-1.510 \pm 0.080	-1.396 \pm 0.080	-0.740 \pm 0.046

TABLE 4. (continued)

Offsets		r_0	Slit	[OIII]	[SII]	Log	Log	Log	Log	Log
E-W	N-S	[arcsec]	No.	ratio	ratio	([OII]+[OIII])	([OIII]/[OII])	([NII]/H α)	([NII]/[OII])	([SII]/[OII])
-033	-007	...	1	93 \pm 17	1.29 \pm 0.12	0.879 \pm 0.013	0.712 \pm 0.029	-1.554 \pm 0.033	-1.209 \pm 0.034	-0.873 \pm 0.033
NGC 2820										
+001	+001	...	1	...	1.38 \pm 0.25	0.812 \pm 0.043	-0.660 \pm 0.074	-0.413 \pm 0.068	-0.683 \pm 0.066	-0.694 \pm 0.064
+021	+011	...	1	...	1.31 \pm 0.13	0.604 \pm 0.018	-0.003 \pm 0.035	-0.622 \pm 0.037	-0.472 \pm 0.038	-0.510 \pm 0.037
-018	-009	...	1	...	1.53 \pm 0.30	0.764 \pm 0.036	-0.125 \pm 0.069	-0.573 \pm 0.074	-0.638 \pm 0.075	-0.580 \pm 0.072
-025	-013	...	1	...	1.52 \pm 0.21	0.852 \pm 0.023	-0.021 \pm 0.045	-0.680 \pm 0.052	-0.775 \pm 0.051	-0.668 \pm 0.049
NGC 2903										
-062	-085	123.2	1	...	1.71 \pm 0.21	0.678 \pm 0.023	-0.304 \pm 0.041	-0.322 \pm 0.044	-0.369 \pm 0.043	-0.526 \pm 0.043
-065	-073	123.7	1	...	1.63 \pm 0.28	0.603 \pm 0.044	-1.416 \pm 0.253	-0.346 \pm 0.048	-0.476 \pm 0.060	-0.560 \pm 0.058
-067	-061	124.9	1	...	1.79 \pm 0.18	0.620 \pm 0.020	-0.619 \pm 0.033	-0.371 \pm 0.051	-0.441 \pm 0.032	-0.607 \pm 0.031
-060	-100	127.8	1	...	1.48 \pm 0.13	0.615 \pm 0.022	-1.064 \pm 0.052	-0.339 \pm 0.033	-0.461 \pm 0.031	-0.566 \pm 0.030
+171	+196	326.6	2	...	1.48 \pm 0.10	0.732 \pm 0.012	-0.269 \pm 0.020	-0.556 \pm 0.025	-0.654 \pm 0.023	-0.834 \pm 0.023
+171	+226	336.3	2	...	1.64 \pm 0.13	0.697 \pm 0.012	-0.147 \pm 0.023	-0.604 \pm 0.029	-0.610 \pm 0.027	-0.783 \pm 0.026
+171	+232	338.7	2	...	1.50 \pm 0.16	0.692 \pm 0.023	-0.793 \pm 0.039	-0.493 \pm 0.038	-0.664 \pm 0.036	-0.681 \pm 0.035
+171	+236	340.3	2	...	1.26 \pm 0.13	0.648 \pm 0.020	-0.795 \pm 0.031	-0.477 \pm 0.034	-0.604 \pm 0.033	-0.675 \pm 0.032
+171	+243	343.3	2	...	1.48 \pm 0.15	0.618 \pm 0.018	-0.736 \pm 0.029	-0.506 \pm 0.032	-0.595 \pm 0.030	-0.742 \pm 0.030
NGC 3184										
-058	-007	60.9	2	...	1.46 \pm 0.11	-0.300 \pm 0.024	-0.566 \pm 0.068	-0.463 \pm 0.028	0.398 \pm 0.031	0.093 \pm 0.030
-064	-006	66.9	2	...	1.55 \pm 0.14	-0.087 \pm 0.031	-0.516 \pm 0.076	-0.319 \pm 0.033	0.340 \pm 0.040	-0.018 \pm 0.040
-080	-005	83.3	2	...	1.59 \pm 0.12	-0.039 \pm 0.016	-0.489 \pm 0.032	-0.384 \pm 0.027	0.232 \pm 0.026	-0.119 \pm 0.025
+085	-004	87.8	4	...	1.46 \pm 0.13	0.081 \pm 0.025	-0.648 \pm 0.066	-0.320 \pm 0.032	0.143 \pm 0.034	-0.172 \pm 0.034
+079	+035	91.5	4	...	1.54 \pm 0.12	-0.060 \pm 0.019	-0.759 \pm 0.048	-0.403 \pm 0.027	0.184 \pm 0.027	-0.106 \pm 0.026
+059	-079	98.7	5	...	1.50 \pm 0.11	0.146 \pm 0.017	-0.801 \pm 0.039	-0.364 \pm 0.027	0.012 \pm 0.025	-0.249 \pm 0.025
+074	+064	104.5	4	...	1.46 \pm 0.13	0.173 \pm 0.022	-0.450 \pm 0.047	-0.374 \pm 0.032	0.042 \pm 0.033	-0.140 \pm 0.033
+092	-093	130.8	5	...	1.50 \pm 0.10	0.256 \pm 0.016	-0.914 \pm 0.030	-0.350 \pm 0.026	-0.100 \pm 0.024	-0.285 \pm 0.023
+005	+135	140.1	3	...	1.38 \pm 0.10	0.565 \pm 0.013	-0.395 \pm 0.020	-0.394 \pm 0.026	-0.355 \pm 0.024	-0.564 \pm 0.023
-002	+136	140.6	3	...	1.56 \pm 0.19	0.255 \pm 0.030	-0.976 \pm 0.125	-0.422 \pm 0.040	-0.176 \pm 0.040	-0.360 \pm 0.040
-017	+137	141.7	3	...	1.40 \pm 0.10	0.311 \pm 0.016	-0.682 \pm 0.025	-0.370 \pm 0.027	-0.142 \pm 0.026	-0.428 \pm 0.025
+111	-102	150.8	5	...	1.88 \pm 0.38	0.701 \pm 0.043	-0.558 \pm 0.077	-0.354 \pm 0.073	-0.492 \pm 0.071	-0.648 \pm 0.069
-119	-121	181.3	1	...	1.44 \pm 0.14	0.416 \pm 0.021	-0.879 \pm 0.050	-0.381 \pm 0.032	-0.286 \pm 0.031	-0.491 \pm 0.031
-113	-127	181.5	1	...	1.18 \pm 0.10	0.747 \pm 0.010	0.308 \pm 0.024	-0.639 \pm 0.029	-0.460 \pm 0.028	-0.831 \pm 0.029
-101	-137	181.5	1	...	1.34 \pm 0.14	0.551 \pm 0.017	-0.291 \pm 0.030	-0.459 \pm 0.033	-0.375 \pm 0.032	-0.770 \pm 0.033
-110	-130	181.8	1	...	1.44 \pm 0.14	0.554 \pm 0.019	-0.481 \pm 0.031	-0.424 \pm 0.033	-0.404 \pm 0.032	-0.730 \pm 0.032
-095	-142	182.0	1	...	1.51 \pm 0.12	0.661 \pm 0.012	-0.065 \pm 0.023	-0.550 \pm 0.028	-0.494 \pm 0.027	-0.514 \pm 0.026
NGC 4395										

TABLE 4. (continued)

Offsets		r_0	Slit	[OIII]	[SII]	Log	Log	Log	Log	Log
E-W	N-S	[arcsec]	No.	ratio	ratio	([OII]+[OIII])	([OIII]/[OII])	([NII]/H α)	([NII]/[OII])	([SII]/[OII])
-003	-003	4.4	6	44 \pm 2	0.87 \pm 0.07	0.993 \pm 0.011	0.584 \pm 0.024	-0.621 \pm 0.032	-0.497 \pm 0.031	-0.435 \pm 0.027
+061	-029	68.5	8	...	1.45 \pm 0.11	0.749 \pm 0.015	-0.426 \pm 0.024	-0.853 \pm 0.023	-1.030 \pm 0.021	-0.807 \pm 0.026
+099	-029	105.3	8	...	1.58 \pm 0.85	0.862 \pm 0.022	0.105 \pm 0.046	-0.794 \pm 0.216	-0.842 \pm 0.214	-0.555 \pm 0.118
+002	-127	128.8	7	...	1.39 \pm 0.10	0.825 \pm 0.011	0.120 \pm 0.023	-1.046 \pm 0.027	-1.073 \pm 0.026	-0.995 \pm 0.026
-075	-117	144.7	4	...	1.46 \pm 0.11	0.835 \pm 0.014	-0.273 \pm 0.024	-0.978 \pm 0.029	-1.177 \pm 0.028	-0.818 \pm 0.027
+088	-119	148.0	9	313 \pm 241	1.38 \pm 0.11	0.825 \pm 0.011	0.195 \pm 0.024	-1.071 \pm 0.030	-1.040 \pm 0.029	-0.708 \pm 0.027
-167	-093	200.5	3	...	1.39 \pm 0.11	0.949 \pm 0.011	0.153 \pm 0.024	-1.068 \pm 0.030	-1.199 \pm 0.029	-0.772 \pm 0.027
+118	+206	246.7	10	...	1.49 \pm 0.11	0.750 \pm 0.012	-0.081 \pm 0.023	-0.952 \pm 0.029	-0.998 \pm 0.027	-0.918 \pm 0.026
+195	-159	252.8	11	...	1.46 \pm 0.12	0.878 \pm 0.013	-0.130 \pm 0.024	-1.046 \pm 0.030	-1.313 \pm 0.029	-1.056 \pm 0.028
+200	+141	256.7	12	...	1.44 \pm 0.11	0.843 \pm 0.013	-0.112 \pm 0.024	-0.941 \pm 0.029	-1.082 \pm 0.028	-0.872 \pm 0.027
-226	+237	328.0	2	...	1.46 \pm 0.12	0.860 \pm 0.011	0.220 \pm 0.024	-1.139 \pm 0.032	-1.145 \pm 0.030	-0.980 \pm 0.028
-272	+186	332.0	1	207 \pm 44	1.48 \pm 0.11	0.905 \pm 0.011	0.210 \pm 0.024	-1.144 \pm 0.028	-1.194 \pm 0.027	-0.910 \pm 0.026
NGC 5457										
-075	+028	84.7	7	...	1.30 \pm 0.11	-0.223 \pm 0.024	-0.408 \pm 0.052	-0.387 \pm 0.030	0.436 \pm 0.034	0.118 \pm 0.034
-106	+028	114.3	7	...	1.19 \pm 0.15	0.146 \pm 0.032	-0.309 \pm 0.065	-0.401 \pm 0.043	0.077 \pm 0.048	-0.212 \pm 0.048
-347	+276	465.2	4	220 \pm 14	1.41 \pm 0.10	0.949 \pm 0.011	0.906 \pm 0.023	-1.279 \pm 0.028	-0.818 \pm 0.026	-0.746 \pm 0.025
-459	-053	474.1	2	182 \pm 25	1.43 \pm 0.11	0.845 \pm 0.011	0.126 \pm 0.023	-1.013 \pm 0.027	-1.047 \pm 0.026	-0.937 \pm 0.027
+271	-393	498.6	11	...	1.43 \pm 0.12	0.730 \pm 0.015	-0.414 \pm 0.024	-0.856 \pm 0.030	-1.001 \pm 0.028	-1.001 \pm 0.027
-276	-417	500.2	6	...	1.34 \pm 0.11	0.719 \pm 0.016	-0.482 \pm 0.025	-1.042 \pm 0.036	-1.192 \pm 0.035	-0.868 \pm 0.027
-037	-532	541.2	8	...	1.42 \pm 0.16	0.813 \pm 0.017	-0.206 \pm 0.030	-0.938 \pm 0.039	-1.097 \pm 0.037	-1.012 \pm 0.034
-250	+484	566.6	5	...	1.80 \pm 0.15	0.743 \pm 0.013	-0.070 \pm 0.025	-1.045 \pm 0.030	-1.093 \pm 0.029	-0.831 \pm 0.028
-398	-436	590.6	3	102 \pm 7	1.40 \pm 0.11	0.867 \pm 0.010	0.414 \pm 0.023	-1.309 \pm 0.027	-1.178 \pm 0.026	-0.998 \pm 0.026
-291	+489	593.1	5	...	1.47 \pm 0.11	0.793 \pm 0.014	-0.334 \pm 0.024	-0.909 \pm 0.029	-1.106 \pm 0.027	-0.880 \pm 0.026
-499	+300	610.6	1	...	1.44 \pm 0.12	0.834 \pm 0.013	-0.042 \pm 0.042	-0.934 \pm 0.033	-1.056 \pm 0.032	-0.927 \pm 0.030
+010	+885	900.6	10	86 \pm 7	1.47 \pm 0.11	0.843 \pm 0.010	0.357 \pm 0.024	-1.297 \pm 0.027	-1.197 \pm 0.026	-0.935 \pm 0.026
+005	+887	902.8	10	...	1.53 \pm 0.12	0.738 \pm 0.013	-0.115 \pm 0.024	-1.182 \pm 0.030	-1.238 \pm 0.028	-0.991 \pm 0.028

Table 5. HII Region Abundances

Offsets		r ₀	Slit	T(O ⁺⁺)	12+Log(O/H)	Log(N/O)	Log(Ne/O)	Log(S/O)	Log(Ar/O)	(O/H)	(O/H)
E-W	N-S	[arcsec]	No.							ZKH	EP84
NGC 0628											
+081	-140	172.6	3	5700 ± 500	8.88±0.12	-1.15±0.17	-0.68±0.34	-1.83±0.26	-2.16±0.21	8.94	8.80
+062	-158	178.8	3	4800 ± 500	8.95±0.19	-1.14±0.24	...	-1.52±0.30	...	9.06	9.01
+047	-172	185.9	3	5500 ± 500	8.90±0.12	-1.17±0.18	...	-1.65±0.26	-2.22±0.22	8.95	8.81
+044	-175	187.7	3	6200 ± 500	8.82±0.10	-1.12±0.15	...	-1.81±0.25	-2.11±0.18	8.84	8.66
+180	-008	195.5	4	5100 ± 500	8.94±0.14	-1.15±0.21	...	-1.61±0.27	-2.13±0.25	9.02	8.94
+178	-052	203.3	4	5300 ± 500	8.95±0.14	-1.14±0.20	-0.60±0.40	-1.80±0.27	-2.16±0.24	9.02	8.93
-086	+186	216.9	2	6400 ± 500	8.79±0.10	-1.19±0.14	-0.81±0.26	-1.26±0.25	-2.20±0.17	8.78	8.60
-075	+200	224.6	2	6700 ± 500	8.69±0.10	-1.23±0.13	...	-1.63±0.24	-2.18±0.16	8.72	8.54
+203	-041	226.4	5	6000 ± 500	8.85±0.11	-0.97±0.16	...	-1.61±0.25	-2.03±0.19	8.87	8.70
-073	+203	226.5	2	6200 ± 500	8.80±0.10	-1.18±0.15	...	-1.67±0.24	-2.20±0.17	8.82	8.64
-069	+208	229.6	2	6900 ± 500	8.73±0.10	-1.15±0.12	-0.73±0.23	-1.51±0.21	-2.20±0.15	8.71	8.53
+254	-043	281.3	6	7000 ± 700	8.69±0.11	-1.16±0.16	...	-1.50±0.25	-2.31±0.20	8.67	8.49
+256	-041	283.0	5	8500 ± 800	8.48±0.10	-1.20±0.13	...	-1.38±0.24	-2.20±0.16	8.52	8.36
-232	+112	283.0	1	6400 ± 500	8.70±0.10	-1.47±0.14	...	-1.56±0.25	...	8.77	8.59
+262	-041	289.4	5	7500 ± 500	8.60±0.10	-1.18±0.11	...	-1.43±0.23	-2.14±0.14	8.62	8.44
+264	-037	290.7	6	7400 ± 500	8.65±0.10	-1.26±0.11	...	-1.55±0.24	-2.24±0.14	8.62	8.44
+265	-041	292.6	5	8300 ± 500	8.55±0.10	-1.22±0.14	...	-1.62±0.24	-2.28±0.18	8.50	8.35
-227	+148	297.2	1	7400 ± 500	8.64±0.10	-1.39±0.11	...	-1.80±0.24	-2.37±0.14	8.63	8.45
+292	-020	318.0	6	12000 ± 1500	8.10±0.10	-1.39±0.13	-0.70±0.25	-1.87±0.24	-2.29±0.16	8.45	7.81
NGC 0925											
+002	-002	3.6	10	5100 ± 500	8.98±0.15	-1.09±0.21	...	-1.63±0.28	-2.09±0.26	9.05	9.00
-005	+000	5.2	10	5100 ± 500	8.94±0.14	-1.14±0.21	...	-1.45±0.27	-2.25±0.25	9.01	8.92
-008	+000	8.4	10	5500 ± 500	8.89±0.12	-1.18±0.18	...	-1.49±0.26	-2.23±0.22	8.93	8.78
+010	-004	11.1	10	5500 ± 500	8.87±0.12	-1.16±0.18	...	-1.44±0.26	-2.24±0.22	8.93	8.79
+015	-005	16.0	10	5100 ± 500	8.96±0.15	-1.03±0.21	...	-1.52±0.28	-2.09±0.26	9.07	9.03
+030	-008	31.1	10	5400 ± 500	8.86±0.13	-1.19±0.19	...	-1.45±0.26	-2.14±0.23	8.94	8.79
+036	-010	37.5	10	5800 ± 500	8.82±0.11	-1.23±0.17	...	-1.49±0.25	-2.13±0.20	8.87	8.70
+042	-011	43.5	10	5800 ± 500	8.84±0.11	-1.18±0.17	...	-1.56±0.25	-2.23±0.20	8.89	8.73
+087	-031	94.1	12	6900 ± 500	8.71±0.10	-1.30±0.13	-0.28±0.23	-1.61±0.24	-2.18±0.15	8.70	8.51
-012	-066	120.5	9	8890 ± 520	8.48±0.05	-1.34±0.08	-0.61±0.13	-1.62±0.12	-2.11±0.10	8.47	8.32
-047	-058	124.2	9	7400 ± 500	8.60±0.10	-1.37±0.11	-0.25±0.20	-1.42±0.24	-2.27±0.13	8.65	8.47
+135	-016	137.2	12	7900 ± 500	8.58±0.10	-1.42±0.13	-0.25±0.25	-1.56±0.24	-2.30±0.16	8.57	8.40
-109	+062	137.6	6	7900 ± 1500	8.48±0.23	-1.25±0.30	-0.50±0.69	-1.72±0.34	-2.14±0.37	8.74	8.56
+137	+011	149.4	13	8900 ± 2000	8.38±0.25	-1.37±0.33	...	-1.43±0.35	-2.41±0.43	8.60	8.43
-137	+056	153.1	6	7000 ± 500	8.68±0.10	-1.35±0.12	...	-1.79±0.24	-2.27±0.15	8.68	8.50
-145	-006	154.8	5	10300 ± 2000	8.23±0.17	-1.28±0.23	-0.70±0.52	-1.60±0.43	-2.17±0.29	8.57	7.70
-080	+087	156.3	7	8300 ± 800	8.48±0.10	-1.42±0.14	-0.43±0.26	-1.53±0.22	-2.26±0.17	8.57	8.40
-114	+087	170.2	7	8500 ± 800	8.51±0.10	-1.45±0.13	...	-1.44±0.24	-2.35±0.16	8.49	8.34
+161	+015	177.0	13	8700 ± 2000	8.38±0.24	-1.46±0.35	...	-1.55±0.36	-2.36±0.43	8.67	8.48
+174	+018	192.5	13	8900 ± 1000	8.28±0.11	-1.64±0.16	...	-1.39±0.25	...	8.70	8.51
+182	+019	201.5	13	12500 ± 1500	8.01±0.10	-1.43±0.12	-0.89±0.23	-1.74±0.19	-2.22±0.16	8.54	7.72
-187	-017	205.3	5	7800 ± 500	8.61±0.10	-1.41±0.10	-0.67±0.18	-1.66±0.23	-2.34±0.12	8.58	8.41
-192	-018	211.1	3	8300 ± 800	8.56±0.10	-1.49±0.14	-0.68±0.26	-1.72±0.24	-2.36±0.17	8.50	8.34
-192	-018	211.1	5	8500 ± 800	8.53±0.10	-1.44±0.13	-0.68±0.25	-1.51±0.21	-2.37±0.16	8.51	8.35
-198	-013	214.1	3	10000 ± 2000	8.35±0.18	-1.40±0.25	-0.72±0.56	-1.67±0.42	-2.32±0.31	8.44	7.81
+209	-006	216.5	15	8600 ± 1600	8.39±0.19	-1.52±0.26	...	-1.55±0.30	-2.18±0.33	8.63	8.45
-200	-020	220.8	5	7500 ± 500	8.65±0.10	-1.34±0.11	-0.49±0.19	-1.68±0.23	-2.28±0.13	8.60	8.42
+217	-006	224.9	15	11200 ± 1500	8.19±0.10	-1.48±0.15	-0.48±0.29	-1.52±0.25	-2.45±0.19	8.43	7.82
+156	-114	226.4	14	7700 ± 600	8.59±0.10	-1.46±0.12	...	-1.38±0.20	-2.33±0.14	8.60	8.42

Table 5—Continued

Offsets		r_0	Slit							(O/H)	(O/H)
E-W	N-S	[arcsec]	No.	T(O ⁺⁺)	12+Log(O/H)	Log(N/O)	Log(Ne/O)	Log(S/O)	Log(Ar/O)	ZKH	EP84
-220	+004	228.7	3	7100 ± 500	8.67±0.10	-1.50±0.12	-0.71±0.22	-1.41±0.20	-2.33±0.14	8.67	8.49
+221	-006	229.0	15	11200 ± 1500	8.27±0.11	-1.27±0.15	...	-1.58±0.25	-2.35±0.19	8.31	7.91
+052	+130	249.1	11	11000 ± 1500	8.20±0.10	-1.57±0.15	-0.68±0.30	-1.68±0.25	-2.21±0.19	8.44	7.81
-250	+019	255.6	2	9300 ± 2000	8.31±0.23	-1.27±0.29	-0.77±0.70	-1.31±0.62	-2.15±0.38	8.66	8.48
+206	-114	256.8	14	7400 ± 500	8.65±0.10	-1.45±0.11	...	-1.62±0.24	-2.29±0.14	8.62	8.45
+019	+143	258.7	11	10000 ± 1000	8.39±0.10	-1.47±0.12	-0.52±0.23	-1.71±0.21	-2.32±0.15	8.32	7.90
-174	+140	269.3	4	11000 ± 1500	8.19±0.10	-1.43±0.15	-0.65±0.30	-1.62±0.24	-2.31±0.19	8.51	7.76
-262	+011	270.2	1	9800 ± 1000	8.30±0.10	-1.52±0.14	...	-1.45±0.24	...	8.50	7.76
-272	+016	279.2	1	9700 ± 1000	8.29±0.10	-1.55±0.15	...	-1.34±0.24	-2.44±0.18	8.56	7.71
-274	+010	283.1	2	10300 ± 2000	8.29±0.16	-1.41±0.23	-0.36±0.51	-1.50±0.40	-2.40±0.29	8.48	7.78
-285	+023	291.1	1	9700 ± 1000	8.30±0.10	-1.58±0.15	-0.51±0.25	-1.25±0.23	-2.39±0.17	8.56	7.70
-159	+162	294.3	4	7800 ± 700	8.49±0.10	-1.51±0.14	...	-1.28±0.24	...	8.63	8.45
-308	+035	313.2	1	8100 ± 800	8.50±0.10	-1.43±0.14	...	-1.34±0.24	-2.10±0.17	8.61	8.43
-149	+177	314.0	4	8600 ± 1600	8.38±0.18	-1.51±0.26	-0.63±0.40	-1.60±0.47	-2.40±0.32	8.69	8.50
-022	+227	396.8	8	9440 ± 1380	8.39±0.09	-1.53±0.13	-0.87±0.24	-1.93±0.24	-2.23±0.16	8.46	7.79
NGC 1068											
+111	-088	159.5	1	4700 ± 300	9.04±0.13	-0.82±0.15	...	-1.56±0.26	...	9.11	9.13
NGC 1232											
+062	+004	62.2	4	4200 ± 200	9.07±0.10	-0.95±0.13	...	-1.49±0.24	...	9.18	9.25
+075	-001	75.0	5	4900 ± 300	8.94±0.11	-1.07±0.14	...	-1.45±0.25	...	9.02	8.92
+075	-012	76.2	5	5200 ± 300	8.87±0.10	-1.00±0.13	...	-1.42±0.24	...	8.98	8.87
+059	+058	88.9	4	4300 ± 200	9.08±0.10	-0.88±0.12	...	-0.93±0.30	-2.38±0.14	9.16	9.23
-103	-021	105.8	1	5100 ± 400	8.94±0.14	-1.00±0.26	...	-1.55±0.27	-2.34±0.22	9.03	8.95
-103	+022	106.0	1	5900 ± 400	8.83±0.10	-1.07±0.13	...	-1.61±0.24	-2.45±0.18	8.88	8.72
+021	+091	106.5	3	5800 ± 400	8.85±0.10	-1.02±0.14	...	-1.19±0.24	-2.24±0.16	8.91	8.77
+004	-101	115.9	2	5900 ± 400	8.80±0.10	-1.03±0.13	...	-1.20±0.23	-2.27±0.16	8.88	8.72
+057	+098	126.0	4	7000 ± 700	8.67±0.10	-1.12±0.16	...	-1.13±0.31	-2.30±0.20	8.70	8.52
+056	+106	133.9	4	6600 ± 500	8.74±0.10	-1.21±0.14	...	-1.61±0.24	...	8.76	8.57
+147	-030	151.0	8	5800 ± 500	8.85±0.10	-1.05±0.17	...	-1.56±0.25	-2.40±0.19	8.90	8.74
+117	-084	151.6	7	6500 ± 500	8.77±0.10	-1.18±0.14	...	-1.68±0.24	-2.44±0.16	8.80	8.61
+099	-101	152.4	6	6700 ± 500	8.71±0.10	-1.16±0.13	...	-1.71±0.24	-2.30±0.16	8.74	8.55
+093	-110	156.7	6	7300 ± 800	8.64±0.11	-1.16±0.17	...	-1.56±0.25	-2.39±0.21	8.66	8.48
+147	-065	164.8	8	6400 ± 500	8.75±0.10	-1.22±0.14	...	-1.58±0.24	-2.43±0.19	8.78	8.60
+135	+114	187.9	7	10670 ± 650	8.20±0.05	-1.09±0.08	-0.96±0.11	-1.74±0.11	-2.23±0.10	8.53	7.73
NGC 1637											
-001	-000	1.2	3	4000 ± 200	9.18±0.11	-0.55±0.14	...	-1.40±0.25	...	9.23	9.34
+016	-001	19.5	4	4900 ± 300	8.91±0.13	-0.97±0.16	...	-1.42±0.26	...	9.01	8.92
-019	-009	23.9	2	5200 ± 300	8.94±0.11	-0.82±0.15	...	-1.61±0.26	...	9.01	8.92
-020	-000	24.2	2	3300 ± 200	9.30±0.21	-0.61±0.20	...	-1.46±0.31	...	9.35	9.52
-001	+026	26.6	3	4300 ± 200	9.10±0.10	-0.79±0.12	...	-1.53±0.24	...	9.18	9.25
+009	-026	29.6	4	4100 ± 200	9.10±0.10	-0.90±0.13	...	-1.46±0.25	...	9.18	9.25
+022	+018	30.7	4	3900 ± 200	9.12±0.11	-0.96±0.14	...	-1.50±0.25	...	9.20	9.29
+026	+018	34.8	5	4100 ± 200	9.11±0.11	-0.92±0.13	...	-1.48±0.25	...	9.18	9.25
-017	-031	35.8	2	3500 ± 200	9.26±0.16	-0.79±0.17	...	-1.52±0.28	...	9.30	9.44
+051	+012	61.7	7	3550 ± 200	9.24±0.17	-0.63±0.17	...	-1.42±0.28	...	9.31	9.46
-055	-011	66.3	1	4900 ± 300	8.95±0.11	-0.89±0.14	...	-1.51±0.25	...	9.06	9.01
+047	-031	67.7	6	3900 ± 200	9.12±0.10	-0.88±0.14	...	-1.56±0.24	-2.16±0.17	9.22	9.32
+047	+046	69.9	7	4000 ± 200	9.12±0.10	-0.88±0.14	...	-1.52±0.25	...	9.18	9.26
-055	-032	71.0	1	4500 ± 200	9.04±0.10	-0.78±0.12	...	-1.44±0.24	...	9.15	9.21
+058	-054	93.3	8	6200 ± 400	8.74±0.10	-1.14±0.12	...	-1.50±0.24	-2.06±0.15	8.82	8.64

Table 5—Continued

Offsets		r_0	Slit							(O/H)	(O/H)
E-W	N-S	[arcsec]	No.	T(O ⁺⁺)	12+Log(O/H)	Log(N/O)	Log(Ne/O)	Log(S/O)	Log(Ar/O)	ZKH	EP84
NGC 2403											
+186	-177	262.4	4	7600 ± 1400	8.74±0.24	-1.16±0.30	-0.50±0.69	-1.50±0.34	-2.26±0.38	8.41	8.28
+178	-203	286.4	4	8200 ± 1500	8.40±0.21	-1.23±0.27	-0.81±0.62	-1.87±0.32	-2.12±0.35	8.79	8.60
+176	-211	295.2	4	6200 ± 500	8.72±0.11	-1.28±0.15	...	-1.31±0.25	-2.27±0.22	8.81	8.63
+166	-229	315.9	4	7100 ± 500	8.66±0.10	-1.38±0.12	...	-1.52±0.24	-2.40±0.14	8.66	8.48
+356	-195	414.2	5	9100 ± 1000	8.44±0.10	-1.35±0.14	-0.80±0.28	-1.54±0.25	-2.27±0.17	8.44	8.30
+360	-190	417.5	5	8000 ± 1500	8.44±0.18	-1.36±0.28	-0.20±0.67	-1.32±0.30	-2.39±0.34	8.78	8.59
+377	-163	435.2	5	8500 ± 1500	8.42±0.18	-1.39±0.25	-1.04±0.56	-1.69±0.30	-2.22±0.31	8.65	8.47
+376	-106	446.8	6	10300 ± 2000	8.23±0.17	-1.53±0.23	-0.72±0.52	-1.70±0.46	-2.31±0.29	8.55	8.39
-377	+104	448.9	2	8000 ± 1500	8.46±0.20	-1.40±0.28	-0.63±0.67	-1.69±0.32	-2.22±0.35	8.71	8.52
-105	-218	452.0	3	7800 ± 1500	8.33±0.22	-1.48±0.31	...	-1.70±0.33	...	8.93	8.78
-105	-224	461.5	3	7400 ± 1400	8.44±0.23	-1.48±0.32	...	-1.62±0.33	...	8.85	8.67
-381	+082	464.5	2	8600 ± 1600	8.43±0.19	-1.47±0.26	...	-1.69±0.30	-2.24±0.33	8.60	8.43
+383	-056	482.7	6	9100 ± 2000	8.35±0.23	-1.56±0.31	...	-1.94±0.34	-2.37±0.39	8.61	8.44
-104	-256	511.2	3	8500 ± 1500	8.34±0.18	-1.58±0.25	...	-1.68±0.30	-2.36±0.31	8.72	8.53
-425	-002	585.8	1	8900 ± 2000	8.33±0.24	-1.58±0.32	...	-1.61±0.34	-2.35±0.41	8.68	8.49
-423	-010	590.3	1	9300 ± 2000	8.26±0.21	-1.56±0.29	...	-1.71±0.32	-2.45±0.37	8.70	8.52
-421	-017	594.1	1	9000 ± 1000	8.21±0.11	-1.55±0.15	...	-1.49±0.25	-2.12±0.19	8.79	8.61
NGC 2805											
-051	-009	60.8	2	5900 ± 400	8.84±0.10	-1.14±0.13	-0.62±0.25	-1.21±0.24	-2.33±0.16	8.93	8.78
+055	-026	61.5	6	7300 ± 800	8.64±0.11	-1.27±0.17	-0.50±0.35	-1.62±0.25	-2.36±0.21	8.65	8.47
+058	-022	63.4	6	6500 ± 500	8.75±0.10	-1.25±0.14	-0.47±0.26	-1.56±0.24	-2.31±0.16	8.77	8.58
-021	-045	65.3	3	6200 ± 500	8.79±0.10	-1.18±0.15	...	-1.69±0.24	-2.23±0.18	8.85	8.67
+032	-056	68.8	6	7300 ± 800	8.62±0.11	-1.32±0.17	...	-1.57±0.26	-2.51±0.22	8.64	8.46
-001	-079	97.2	4	6800 ± 500	8.75±0.10	-1.28±0.13	-0.65±0.24	-1.31±0.22	-2.28±0.15	8.73	8.54
-005	-080	99.8	4	7300 ± 800	8.65±0.11	-1.29±0.17	...	-1.47±0.29	-2.43±0.20	8.65	8.46
-041	-090	130.0	4	8000 ± 800	8.56±0.10	-1.35±0.15	-0.43±0.28	-1.49±0.24	-2.43±0.17	8.56	8.40
+037	-115	136.4	5	9710 ± 490	8.33±0.04	-1.34±0.08	-0.70±0.11	-1.57±0.10	-2.32±0.09	8.53	8.37
+078	-107	137.6	5	7900 ± 500	8.61±0.10	-1.37±0.13	-0.76±0.25	-1.61±0.25	-2.37±0.17	8.56	8.39
-068	-079	137.7	3	11480 ± 840	8.19±0.05	-1.31±0.08	-0.62±0.13	-1.67±0.11	-2.35±0.10	8.41	7.84
+080	-110	141.3	6	10000 ± 1000	8.38±0.10	-1.38±0.13	...	-1.42±0.24	-2.48±0.16	8.37	8.26
+017	-119	142.3	5	9700 ± 2000	8.28±0.20	-1.30±0.27	-0.96±0.62	-1.60±0.31	-2.24±0.34	8.61	8.44
+089	-107	142.8	6	9180 ± 2670	8.49±0.13	-1.53±0.19	...	-1.64±0.30	-2.42±0.22	8.36	8.25
+116	-098	152.3	6	10970 ± 270	8.22±0.03	-1.37±0.06	-0.62±0.07	-1.64±0.07	-2.35±0.08	8.45	7.80
-145	+104	178.4	1	9300 ± 1000	8.40±0.10	-1.42±0.14	...	-1.45±0.24	...	8.44	8.30
-151	+102	182.2	1	12000 ± 1500	8.16±0.10	-1.32±0.13	-0.75±0.25	-1.72±0.22	-2.32±0.17	8.32	7.91
IC 2458											
+002	-006	...	1	13120 ± 460	8.06±0.03	-1.43±0.07	-0.68±0.08	-1.68±0.08	-2.28±0.08	8.32	7.90
-028	-007	...	1	13100 ± 1500	7.87±0.10	-1.68±0.14	...	-1.37±0.24	...	8.70	7.56
-033	-007	...	1	13210 ± 1110	7.98±0.05	-1.48±0.09	-0.95±0.13	-1.63±0.13	-2.39±0.11	8.48	7.78
NGC 2820											
+001	+001	...	1	6000 ± 1000	8.95±0.25	-1.30±0.34	...	-1.54±0.36	...	8.61	8.43
-018	-009	...	1	6900 ± 500	8.69±0.10	-1.22±0.14	...	-1.49±0.24	...	8.90	8.74
+021	+011	...	1	6000 ± 400	8.83±0.10	-1.08±0.13	...	-1.66±0.24	-2.31±0.16	8.69	8.50
-025	-013	...	1	8000 ± 800	8.60±0.10	-1.25±0.15	...	-1.56±0.25	...	8.53	8.37
NGC 2903											
-062	-085	123.2	1	6200 ± 500	8.78±0.10	-0.96±0.15	...	-1.47±0.25	...	8.81	8.63
-065	-073	123.7	1	5500 ± 500	8.79±0.16	-1.16±0.19	...	-1.31±0.28	...	8.90	8.75
-067	-061	124.9	1	5800 ± 500	8.81±0.11	-1.09±0.17	...	-1.50±0.25	-2.40±0.24	8.88	8.72
-060	-100	127.8	1	5600 ± 500	8.79±0.14	-1.12±0.18	...	-1.34±0.27	...	8.89	8.73

Table 5—Continued

Offsets		r_0 [arcsec]	Slit No.	T(O ⁺⁺)	12+Log(O/H)	Log(N/O)	Log(Ne/O)	Log(S/O)	Log(Ar/O)	(O/H)	(O/H)
E-W	N-S									ZKH	EP84
+171	+196	326.6	2	6700 ± 500	8.71±0.10	-1.19±0.13	...	-1.72±0.24	-2.17±0.16	8.74	8.55
+171	+226	336.3	2	6400 ± 500	8.78±0.10	-1.19±0.14	...	-1.79±0.24	-2.17±0.17	8.79	8.60
+171	+232	338.7	2	6400 ± 500	8.70±0.11	-1.26±0.14	...	-1.42±0.25	-2.02±0.20	8.80	8.61
+171	+236	340.3	2	6000 ± 500	8.74±0.12	-1.25±0.16	...	-1.45±0.26	...	8.85	8.68
+171	+243	343.3	2	5700 ± 500	8.79±0.12	-1.24±0.17	...	-1.57±0.26	-2.02±0.22	8.89	8.72
NGC 3184											
-058	-007	60.9	2	3400 ± 200	9.27±0.15	-0.70±0.18	...	-1.55±0.27	...	9.35	9.51
-064	-006	66.9	2	3700 ± 200	9.23±0.15	-0.67±0.16	...	-1.55±0.27	-2.16±0.23	9.29	9.43
-080	-005	83.3	2	3800 ± 200	9.19±0.11	-0.74±0.15	...	-1.61±0.25	...	9.28	9.41
+085	-004	87.8	4	3900 ± 200	9.18±0.10	-0.78±0.14	...	-1.52±0.25	...	9.24	9.34
+079	+035	91.5	4	3600 ± 200	9.24±0.14	-0.81±0.16	...	-1.52±0.25	...	9.28	9.42
+059	-079	98.7	5	4000 ± 200	9.12±0.10	-0.89±0.14	...	-1.48±0.24	-2.25±0.19	9.21	9.30
+074	+064	104.5	4	4300 ± 200	9.11±0.11	-0.79±0.12	...	-1.46±0.25	...	9.20	9.28
+092	-093	130.8	5	4100 ± 200	9.09±0.10	-0.99±0.13	...	-1.40±0.24	-2.18±0.16	9.16	9.22
+005	+135	140.1	3	5000 ± 600	9.10±0.19	-1.08±0.28	...	-1.70±0.31	-2.26±0.33	8.94	8.80
-002	+136	140.6	3	4200 ± 200	9.05±0.10	-1.06±0.13	...	-1.46±0.25	...	9.16	9.22
-017	+137	141.7	3	4400 ± 200	9.05±0.10	-0.97±0.12	...	-1.56±0.24	...	9.13	9.18
+111	-102	150.8	5	5400 ± 300	9.01±0.22	-1.21±0.28	...	-1.62±0.33	...	8.78	8.60
-119	-121	181.3	1	4700 ± 300	8.97±0.11	-1.07±0.15	...	-1.49±0.25	-2.24±0.25	9.07	9.03
-113	-127	181.5	1	6000 ± 500	8.71±0.10	-1.02±0.16	...	-1.62±0.25	-2.19±0.20	8.72	8.53
-101	-137	181.5	1	5500 ± 500	8.90±0.13	-1.05±0.18	...	-1.84±0.26	-2.12±0.22	8.96	8.82
-110	-130	181.8	1	5500 ± 500	8.87±0.12	-1.06±0.18	...	-1.71±0.26	-2.23±0.23	8.95	8.82
-095	-142	182.0	1	6200 ± 500	8.82±0.10	-1.09±0.15	...	-1.60±0.25	-2.27±0.18	8.84	8.66
NGC 4395											
+061	-029	68.5	8	7800 ± 500	8.48±0.21	-1.50±0.31	...	-1.51±0.32	-2.28±0.37	8.71	8.53
+099	-029	105.3	8	8100 ± 800	8.57±0.10	-1.29±0.25	...	-1.48±0.35	...	8.51	8.36
+002	-127	128.8	7	9700 ± 2000	8.29±0.20	-1.44±0.27	-0.84±0.62	-1.46±0.56	-2.16±0.34	8.58	8.41
-075	-117	144.7	4	8900 ± 2000	8.39±0.23	-1.60±0.32	-0.69±0.80	-1.47±0.34	-2.40±0.41	8.57	8.40
+088	-119	148.0	9	8930 ± ⁵⁷⁹⁰ ₁₂₀₀	8.41±0.17	-1.44±0.27	-0.57±0.47	-1.61±0.30	-2.25±0.31	8.58	8.41
-167	-093	200.5	3	10300 ± 2000	8.33±0.17	-1.59±0.23	-0.58±0.52	-1.54±0.29	-2.26±0.30	8.32	7.90
+118	+206	246.7	10	8500 ± 1500	8.39±0.17	-1.41±0.25	-0.91±0.56	-1.22±0.52	-2.19±0.31	8.71	8.52
+195	-159	252.8	11	10000 ± 2000	8.31±0.17	-1.66±0.25	...	-1.82±0.44	-2.32±0.31	8.48	8.33
+200	+141	256.7	12	9100 ± 2000	8.38±0.22	-1.48±0.31	-0.71±0.74	-1.59±0.33	-2.21±0.39	8.55	8.39
-226	+237	328.0	2	12000 ± 1500	8.06±0.10	-1.46±0.13	-0.83±0.25	-1.69±0.24	-2.17±0.16	8.52	7.74
-272	+186	332.0	1	10050 ± 770	8.33±0.05	-1.55±0.09	-0.75±0.14	-1.65±0.14	-2.28±0.11	8.42	8.29
NGC 5457											
-075	+028	84.7	7	3600 ± 200	9.23±0.17	-0.57±0.17	...	-1.53±0.28	...	9.33	9.48
-106	+028	114.3	7	4250 ± 250	9.13±0.12	-0.80±0.15	...	-1.63±0.25	...	9.21	9.30
-347	+276	465.2	4	9880 ± 170	8.41±0.03	-1.17±0.06	-0.69±0.07	-1.38±0.20	-2.03±0.07	8.32	8.23
-459	-053	474.1	2	10450 ± 480	8.22±0.04	-1.39±0.07	-0.68±0.10	-1.65±0.21	-2.32±0.09	8.55	8.38
+271	-393	498.6	11	7600 ± 1400	8.49±0.21	-1.49±0.30	...	-1.43±0.63	-2.28±0.36	8.74	8.56
-276	-417	500.2	6	8600 ± 1600	8.30±0.19	-1.47±0.26	-0.60±0.40	-1.46±0.30	-2.36±0.33	8.76	8.57
-037	-532	541.2	8	8900 ± 2000	8.38±0.24	-1.54±0.33	...	-1.70±0.34	-2.54±0.42	8.61	8.43
-250	+484	566.6	5	9100 ± 2000	8.28±0.23	-1.48±0.31	-0.74±0.74	-1.58±0.33	-2.42±0.39	8.72	8.54
-398	-436	590.6	3	12750 ± 320	8.01±0.03	-1.44±0.06	-0.77±0.07	-1.66±0.07	-2.30±0.07	8.50	7.76
-291	+489	593.1	5	8300 ± 1500	8.44±0.19	-1.55±0.27	-0.67±0.60	-1.56±0.30	-2.44±0.33	8.64	8.46
-499	+300	610.6	1	10300 ± 1200	8.09±0.10	-1.43±0.14	-0.23±0.27	-1.47±0.24	-2.24±0.17	8.56	7.70
+010	+885	900.6	10	13630 ± 440	7.92±0.03	-1.45±0.06	-0.75±0.07	-1.69±0.39	-2.46±0.08	8.55	7.72
+005	+887	902.8	10	12200 ± 1500	7.95±0.10	-1.51±0.13	-0.51±0.24	-1.53±0.24	-2.44±0.16	8.73	7.53

Table 6. Radial Oxygen Abundance Gradients

Galaxy	No. of HII Regions	Central 12+log(O/H)	Gradients		
			[dex/ r_{25}]	[dex/ r_d]	[dex/kpc]
NGC 0628	26	9.46 ± 0.11	-0.99 ± 0.14	-0.23 ± 0.03	-0.067 ± 0.009
NGC 0925	53	8.79 ± 0.06	-0.45 ± 0.08	-0.12 ± 0.02	-0.032 ± 0.006
NGC 1068	13	9.26 ± 0.02	-0.30 ± 0.07	-0.16 ± 0.04	-0.020 ± 0.004
NGC 1232	16	9.49 ± 0.12	-1.31 ± 0.20	-0.36 ± 0.05	-0.056 ± 0.009
NGC 1637	15	9.18 ± 0.07	-0.34 ± 0.15	-0.06 ± 0.02	-0.068 ± 0.028
NGC 2403	40	8.70 ± 0.07	-0.77 ± 0.14	-0.14 ± 0.02	-0.074 ± 0.013
NGC 2805	17	9.11 ± 0.12	-1.05 ± 0.17	-0.42 ± 0.07	-0.049 ± 0.008
NGC 2903	36	9.22 ± 0.06	-0.56 ± 0.09	-0.13 ± 0.02	-0.048 ± 0.008
NGC 3184	32	9.50 ± 0.04	-0.78 ± 0.07	-0.20 ± 0.02	-0.083 ± 0.007
NGC 4395	14	8.48 ± 0.13	-0.32 ± 0.19	-0.13 ± 0.07	-0.037 ± 0.022
NGC 5457	53	9.29 ± 0.05	-1.52 ± 0.09	-0.27 ± 0.02	-0.049 ± 0.003

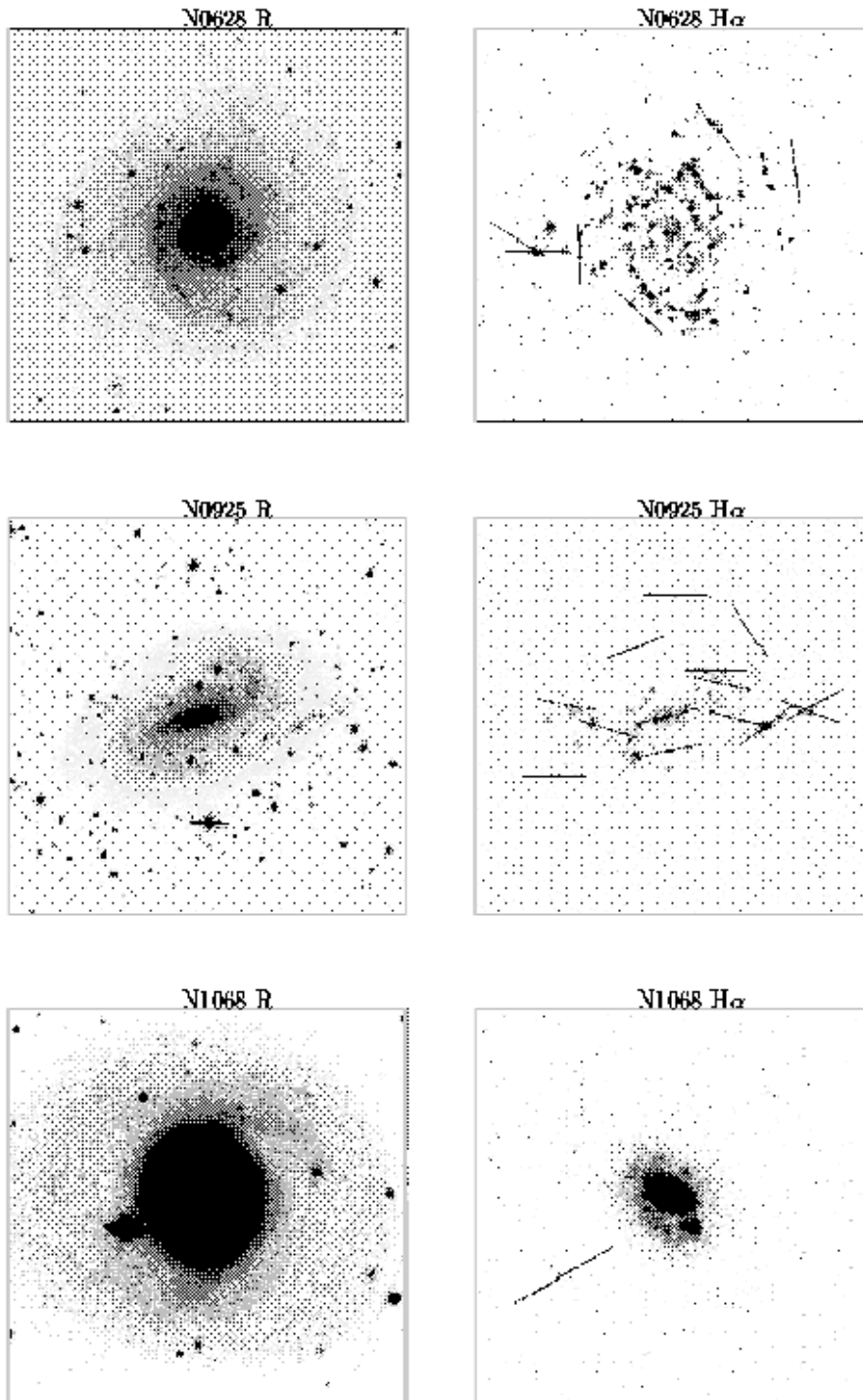


Fig. 1.— R-band and continuum subtracted $H\alpha$ images of the galaxies in the sample. The positions of the 2' slits are illustrated on the $H\alpha$ images. The images are oriented with north to the top and east to the left.

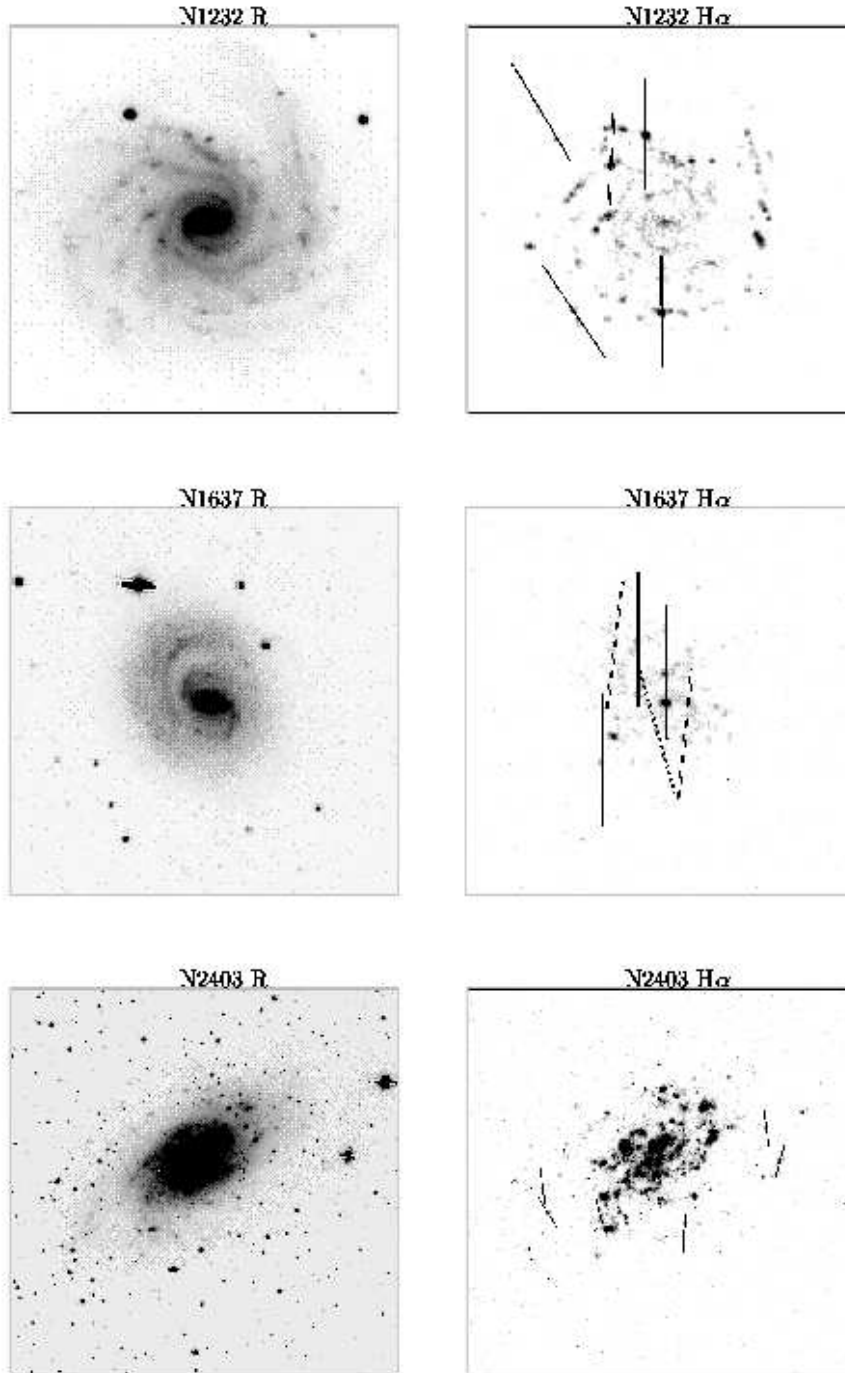


Fig. 1 continued

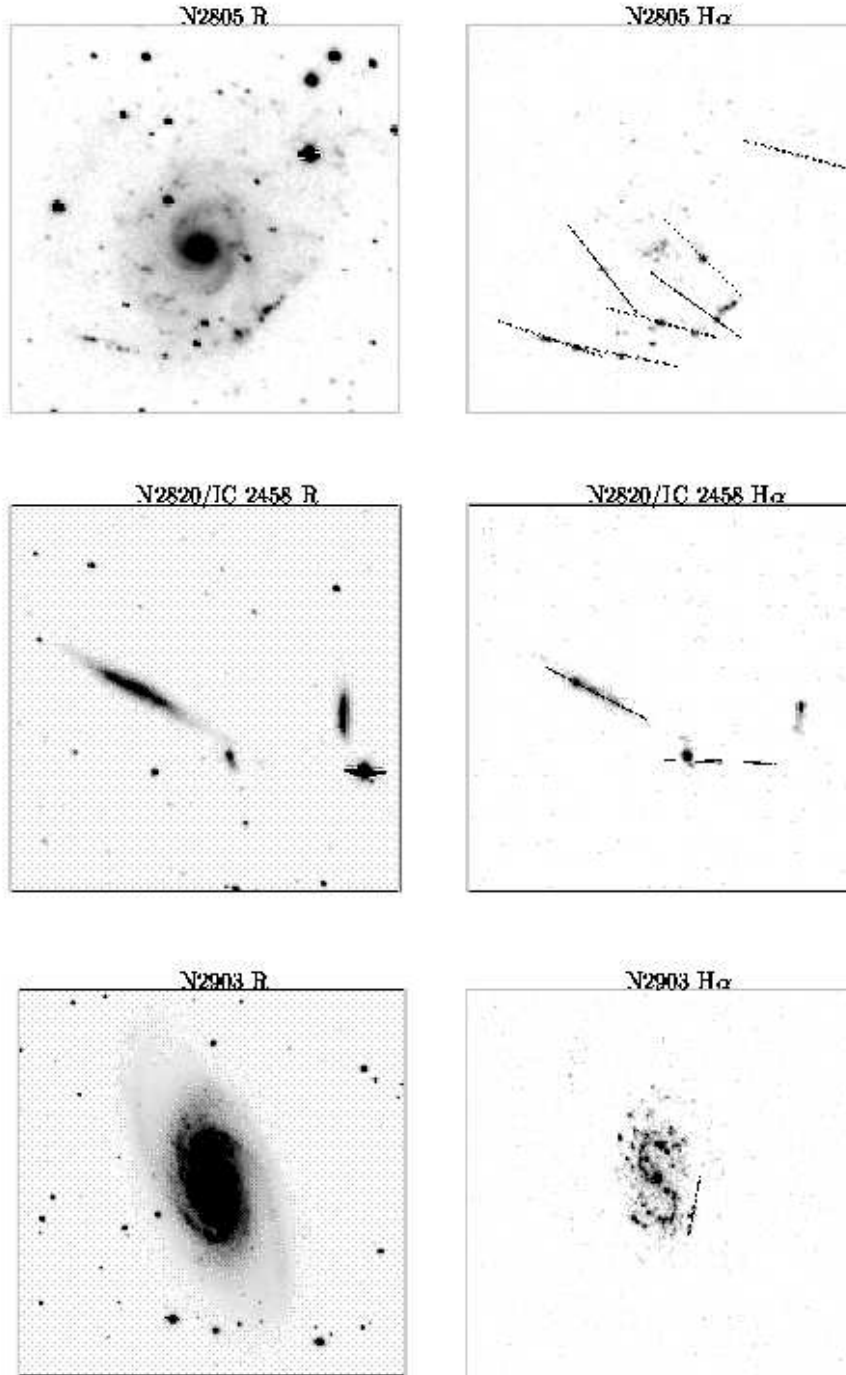


Fig. 1 continued

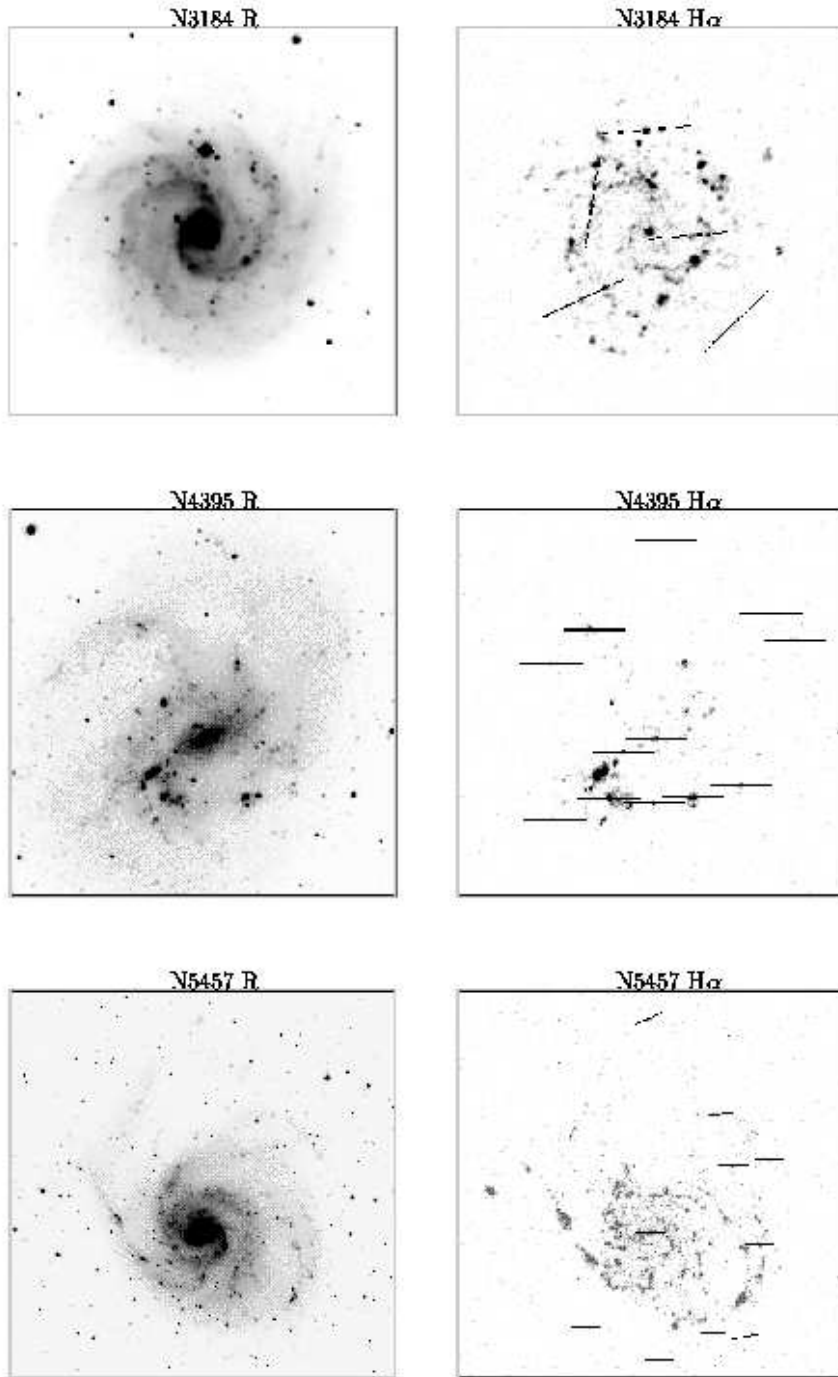


Fig. 1 continued

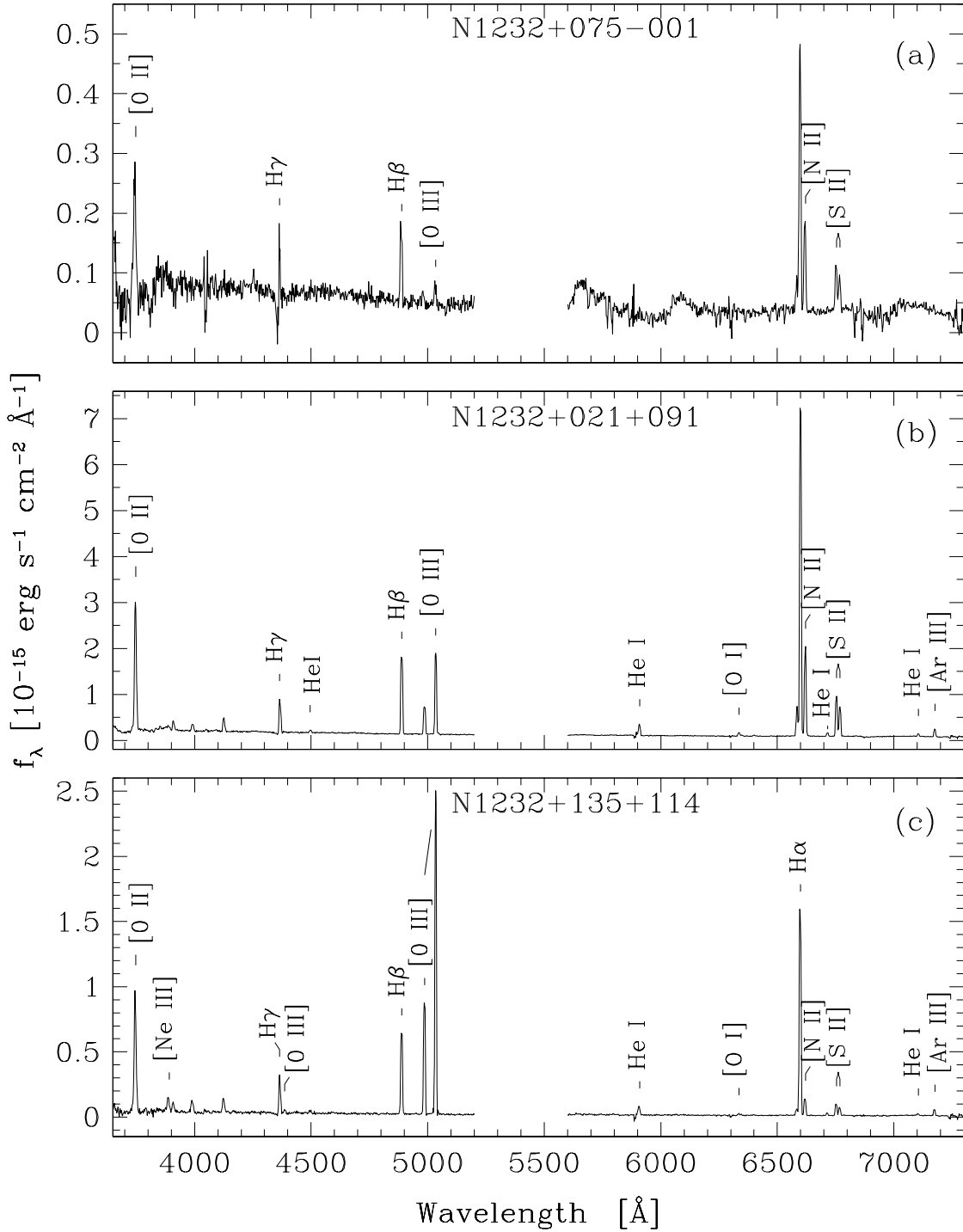


Fig. 2.— Representative spectra of H II regions in NGC 1232. The inner H II regions (a) and (b) are clearly high abundance, with strong [N II] and [S II] and weak [O III] lines. The outermost H II region (c) is low abundance, with weak [N II] and strong [O III] lines.

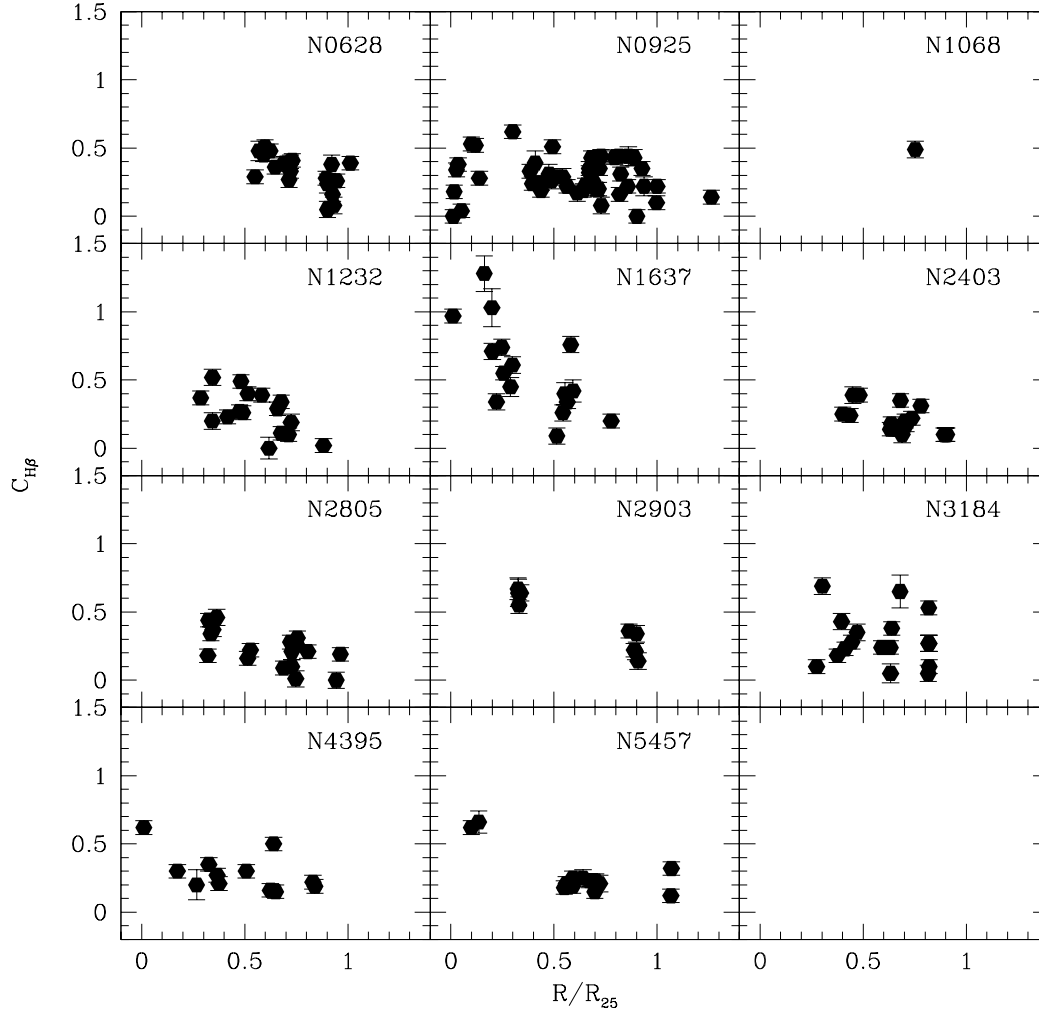


Fig. 3.— Reddening as a function of radius for each galaxy. In each panel the radius has been normalized by the isophotal radius of that galaxy.

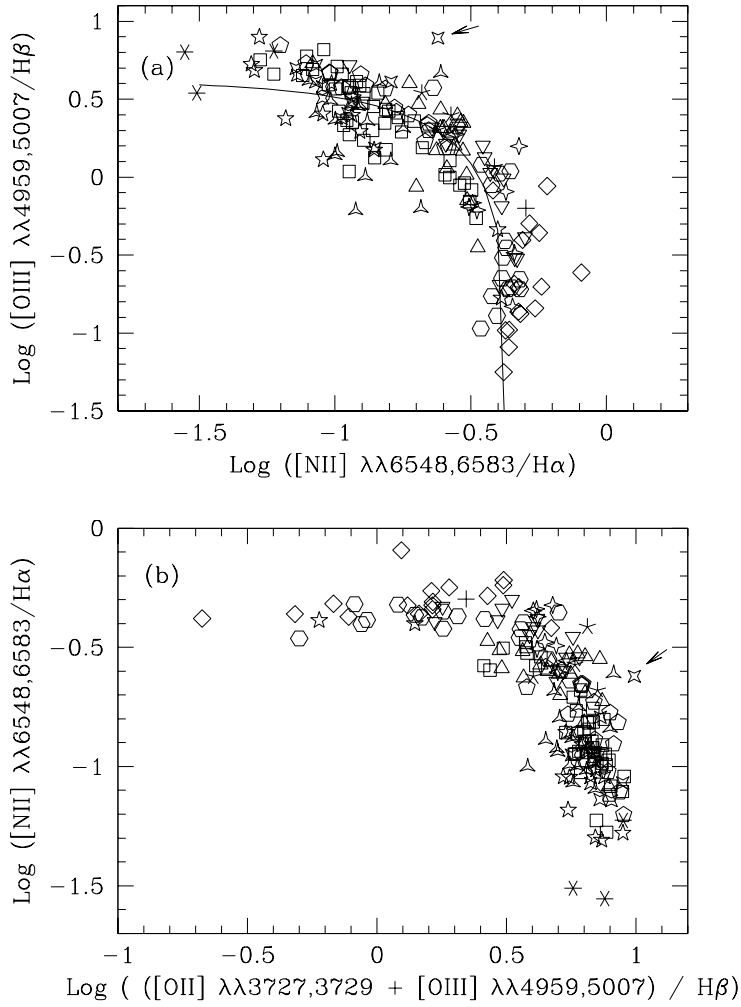


Fig. 4.— Emission–line diagnostic diagram for [N II]. In this and subsequent figures, H II regions from NGC 628 are denoted by upright triangles, NGC 925 by squares, NGC 1068 by crosses, NGC 1232 by downward triangles, NGC 1637 by diamonds, NGC 2403 by upward indented triangles, NGC 2805 by pentagons, IC 2458 by six pointed stars, NGC 2820 by five pointed stars, NGC 2903 by indented crosses, NGC 3184 by hexagons, NGC 4395 by four pointed open stars, and NGC 5457 by five pointed open stars. (a) The H II region sequence formed by [N II] and [O III] normalized by Balmer lines. A theoretical curve from Baldwin *et al.* (1981) is superposed. (b) The H II region sequence formed by R_{23} vs. [N II]/H α . In both panels, NGC 4395–003–003 is marked by an arrow.

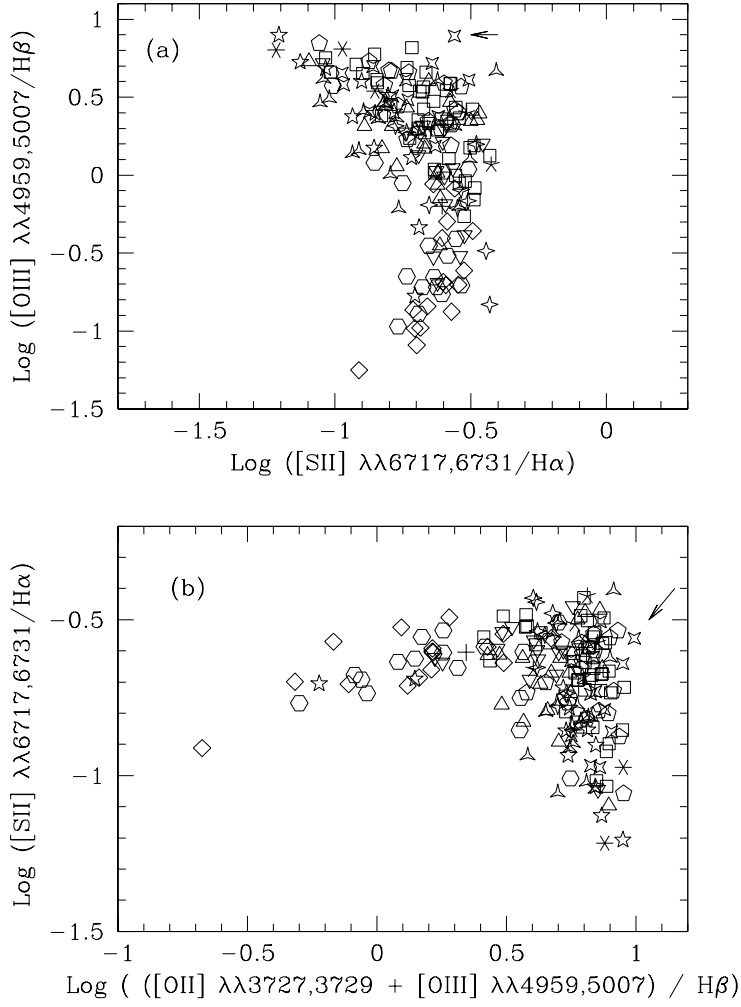


Fig. 5.— Emission–line diagnostic diagrams for [S II]. The symbols are the same as in Figure 4. (a) The H II region sequence formed by [S II] and [O III] normalized by the Balmer lines. (b) The H II region sequence formed by R_{23} vs. [S II]/H α . In both panels, NGC 4395–003–003 is marked by an arrow.

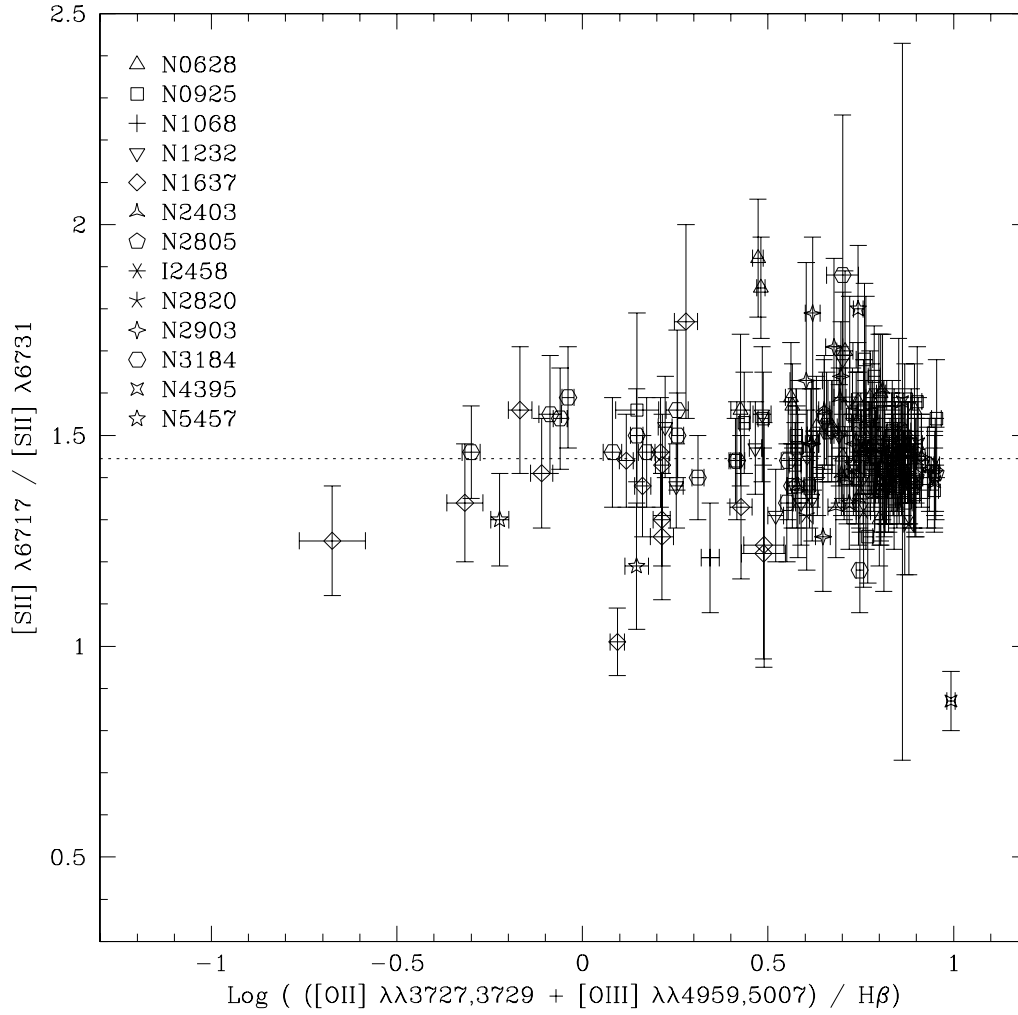


Fig. 6.— The density sensitive line ratio [S II] $\lambda 6717/6731$ as a function of R_{23} . The symbols are the same as in Figure 4. The dashed line indicates the maximum value of the [S II] ratio in the low density limit. The majority of the H II regions fall within the low density limit.

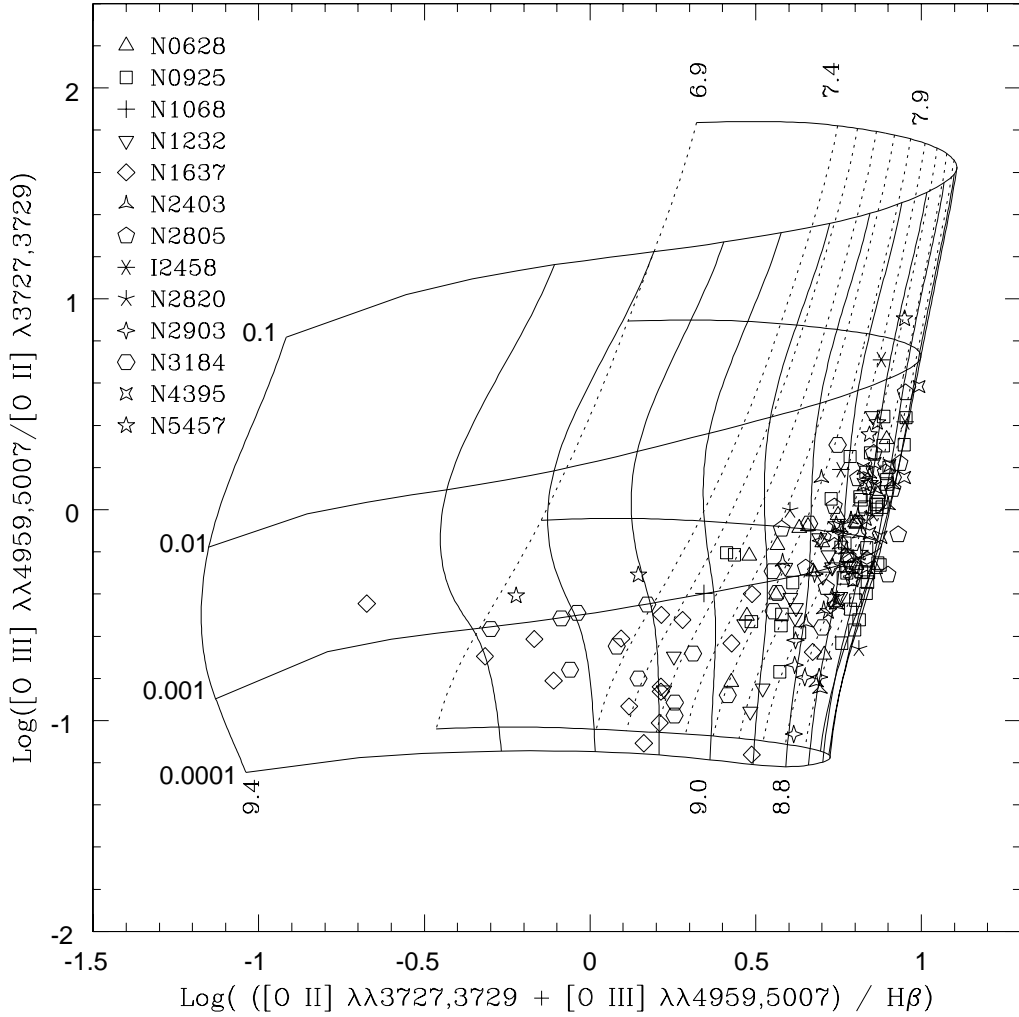


Fig. 7.— The model grid of the R_{23} relation from McGaugh (1991). The locations of the H II regions are marked; the symbols are the same as in Figure 4. The ambiguity between the high and low abundance sides of the surface can be resolved based on the strength of the $[\text{N II}]$ lines.

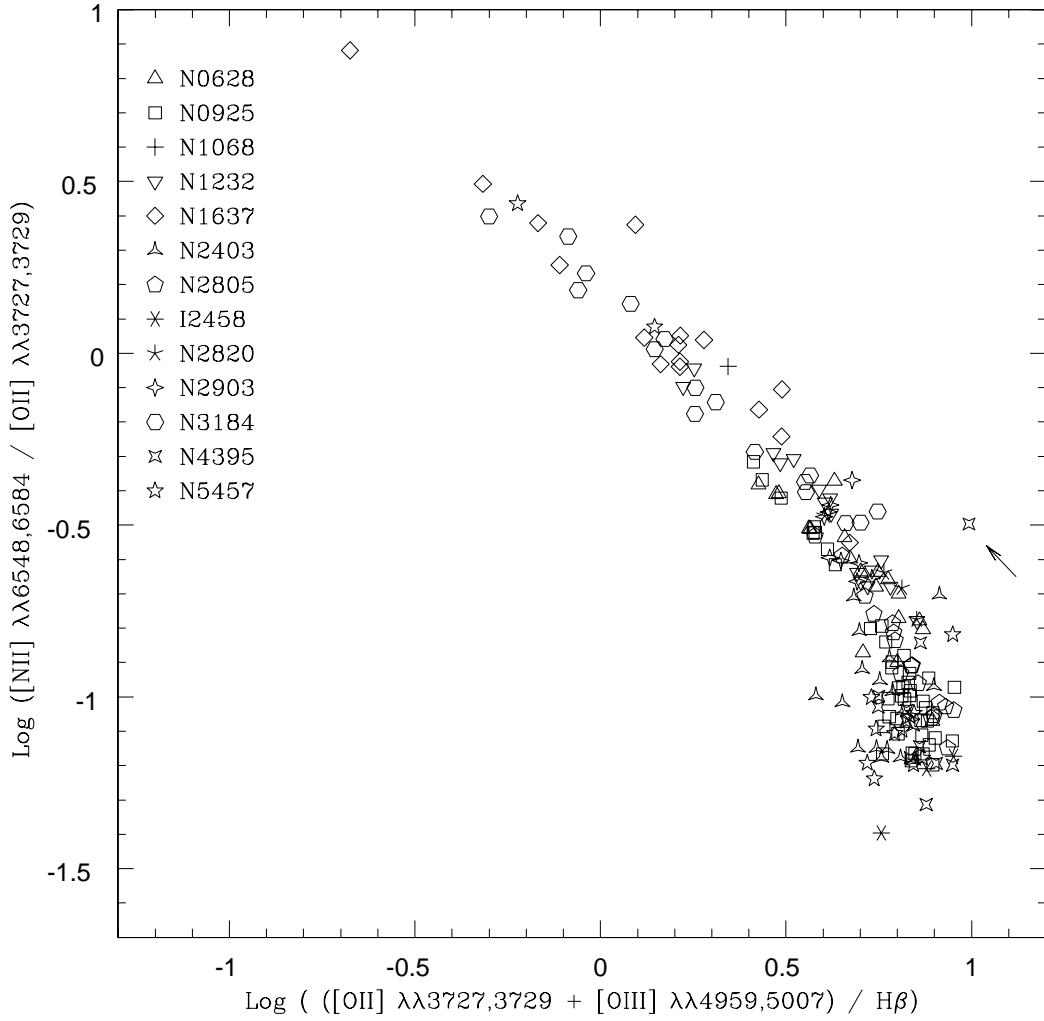


Fig. 8.— The [N II]/[O II] diagnostic diagram. The symbols are the same as in Figure 4. The one outlying point is NGC 4395–003–003. Low values of [N II]/[O II] and high values of [O II]+[O III]/H β are found for the outermost H II regions in NGC 925, NGC 2403, NGC 2805, NGC 4395, and NGC 5457, indicating that these are low abundance H II regions.

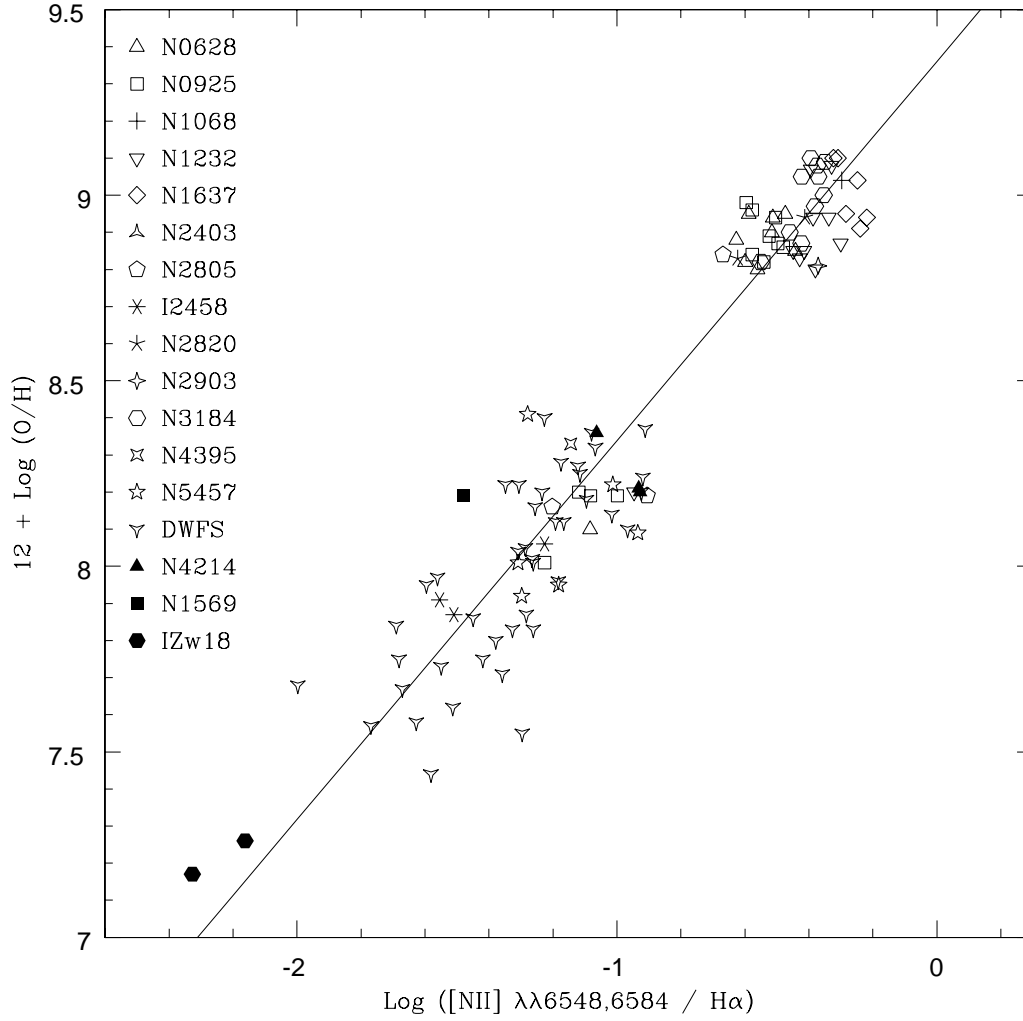


Fig. 9.— A semi-empirical technique for determining oxygen abundances. The line shows the least squares fit to the low ($12 + \log(\text{O}/\text{H}) < 8.2$) and high ($8.8 < 12 + \log(\text{O}/\text{H}) < 9.1$) abundance H II regions and H III regions from a dwarf galaxy sample (van Zee *et al.* 1997). Also plotted are data points for H II regions in NGC 4214 (Kobulnicky & Skillman 1996), NGC 1569 (Kobulnicky & Skillman 1997), and I Zw 18 (Skillman & Kennicutt 1993).

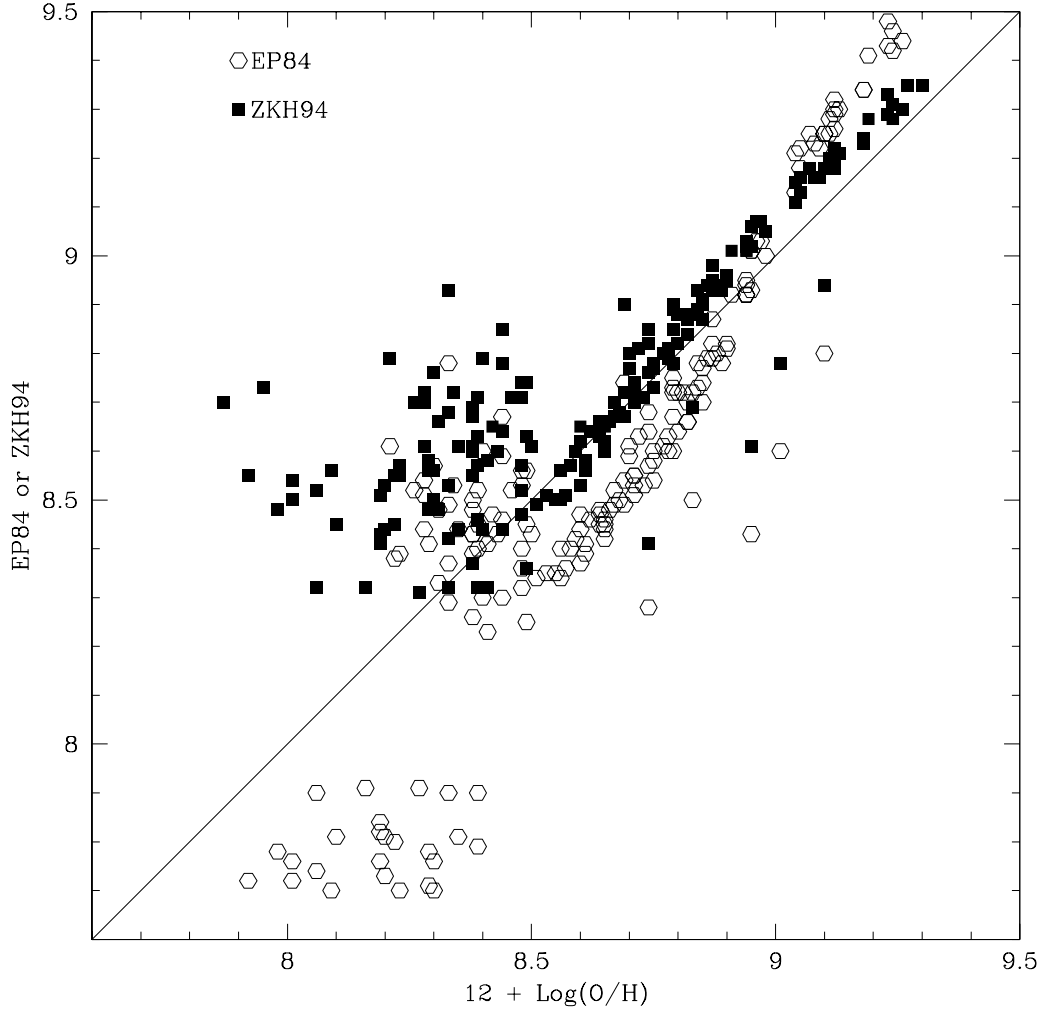


Fig. 10.— Comparison between R_{23} calibrations. The large scatter for $12 + \log(O/H) < 8.5$ is due to the turnover in the R_{23} relation which has not been accounted for in the ZKH (Zaritsky *et al.* 1994) calibration. The six high abundance points which are offset from both the EP84 (Edmunds & Pagel 1984) and ZKH calibrations are from H II regions where the $[N II]/H\alpha$ calibration was used instead of the pure R_{23} relation. Two of these points are from the edge-on spiral NGC 2820, where the combination of uncertain extinction corrections and the superpositions of multiple H II regions make the empirical calibration highly uncertain. While there are systematic differences between the calibrations, at high abundances the ZKH calibration is very similar to the calibration used here. In contrast, the calibration of EP84 would result in much steeper abundance gradients.

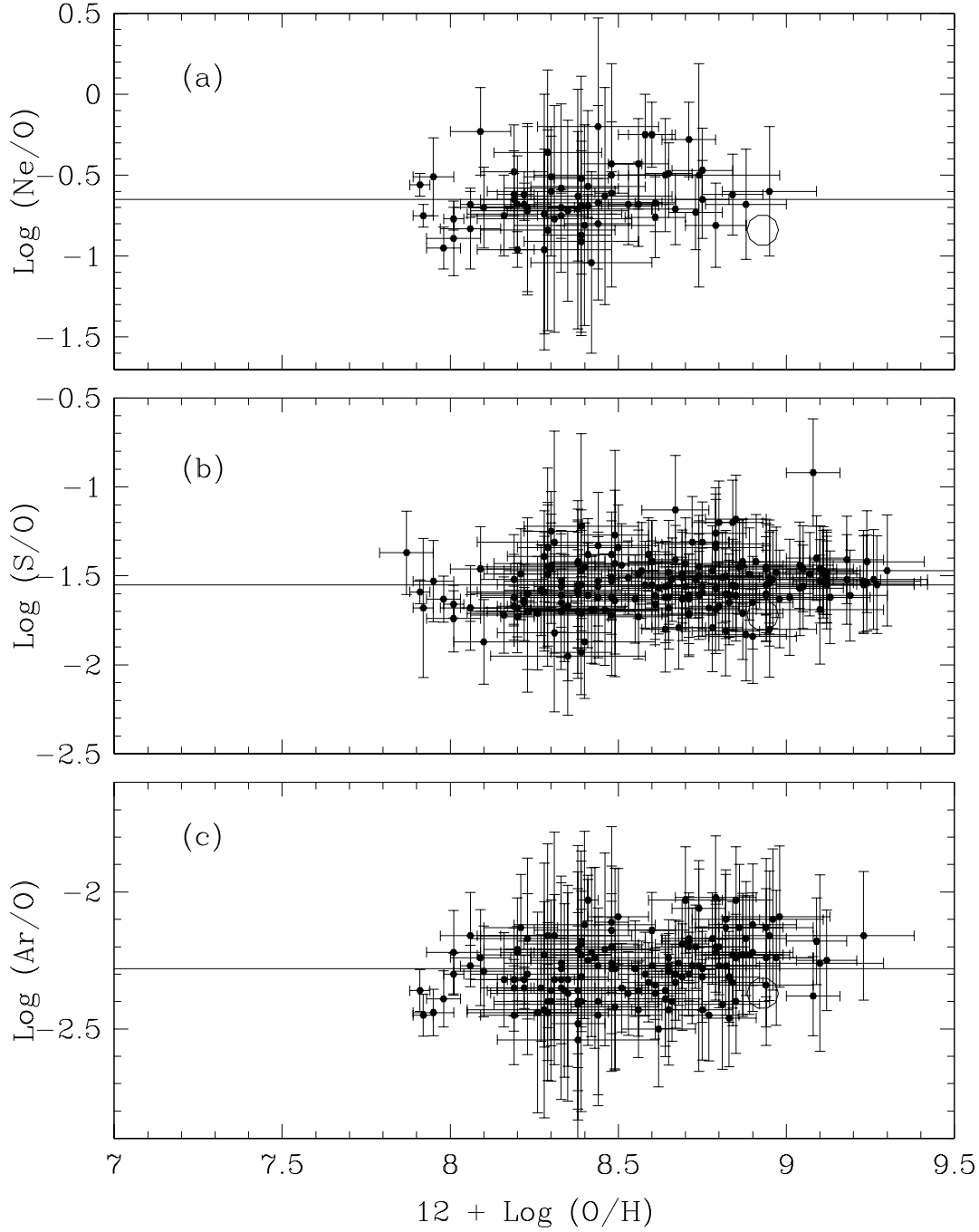


Fig. 11.— The relative enrichment of the α elements. In all three panels, the mean value is denoted by a solid line. The solar value (Anders & Grevesse 1989) is represented by an open circle, where the symbol size is indicative of the errors. (a) $\text{Log}(\text{Ne}/\text{O})$ as a function of oxygen abundance. (b) $\text{Log}(\text{S}/\text{O})$ as a function of oxygen abundance. (c) $\text{Log}(\text{Ar}/\text{O})$ as a function of oxygen abundance.

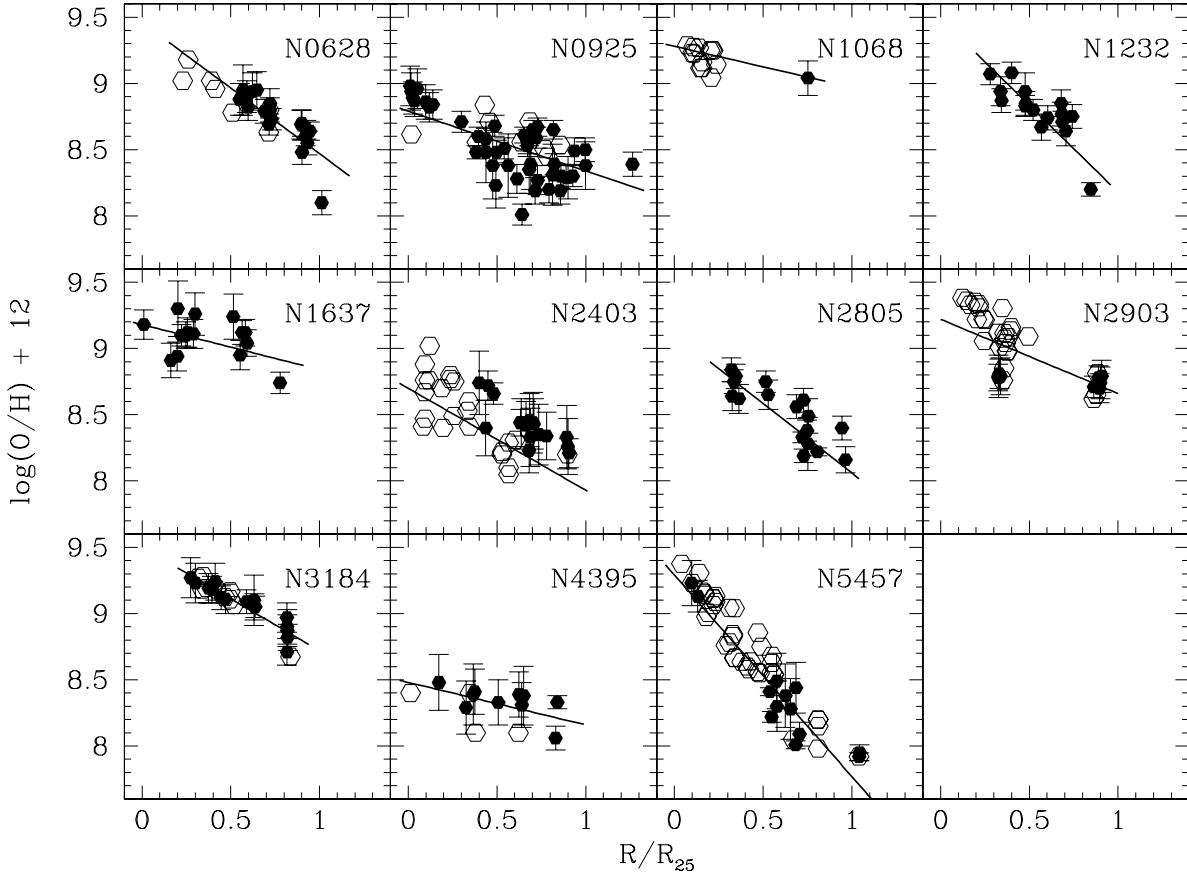


Fig. 12.— The observed oxygen abundance gradients in all 11 spiral galaxies. The filled symbols represent H II regions from the present study. The open circles represent data from the literature: NGC 628– McCall *et al.* (1985); NGC 925– Zaritsky *et al.* (1994); NGC 1068– Evans & Dopita (1987), Oey & Kennicutt (1993); NGC 2403– McCall *et al.* (1985), Fierro *et al.* (1986), Garnett *et al.* (1997); NGC 2903– McCall *et al.* (1985), Zaritsky *et al.* (1994); NGC 3184– Zaritsky *et al.* (1994); NGC 4395– McCall *et al.* (1985); NGC 5457– Kennicutt & Garnett (1996). The solid lines illustrate the derived oxygen abundance gradients.